UNIVERSITY OF CALIFORNIA SAN DIEGO

Point-of-Care and High-Density Array Electrochemical Biosensors

A dissertation submitted in partial satisfaction of the
requirements for the degree Doctor of Philosophy

in

Electrical Engineering (Electronic Circuits and Systems)

by

Alexander Chuan Sun

Committee in charge:

Professor Drew A. Hall, Chair
Professor Gert Cauwenberghs
Professor Yeshaiahu Fainman
Professor Yu-Hwa Lo
Professor Patrick Mercier

2018

The Dissertation of Alexander Chuan Sun is approved, and it is acceptable in quality and form for publication on microfilm and electronically:

_____

_____

_____

_____

_____

Chair

University of California San Diego

2018

DEDICATION

To Annette Shaw and Yik-Ching Sun, my parents, for their immeasurable love and support.

To Christine Sun, my sister, role model, and mentor.

TABLE OF CONTENTS

LIST OF FIGURES

LIST OF TABLES

ACKNOWLEDGEMENTS

Over this past six years I have received support and encouragement from a great number of individuals. I would first like to acknowledge my advisor, Professor Drew Hall, for his invaluable mentorship and guidance as well as his extreme patience during my journey through graduate school. It is with his unwavering confidence in me that I was able to accomplish this body of work. I would also like to thank my other mentors and members of my committee, Professor Gert Cauwenbergs, Professor Yeshaiahu Fainman, Professor Patrick Mercier, Professor Vikash Gilja, Dr. Eliah Aronoff-Spencer, and Professor Yu Hwa Lo, for their input and feedback.

I also owe many thanks to my fellow colleagues for their help, advice, and friendship. I would like to thank Chung-Lun Edwin Hsu for being a great friend and source of knowledge ever since the beginning when we were the only two students in a windowless blue room. I would also like to acknowledge Venkatesh Alagarswamy, Chih-Cheng Huang, Brandon Hong, and Rajesh Seenivasan for their immense assistance and expertise. I would also like to express my gratitude to Enrique Alvarez-Fontecilla, Somok Mondal, Haowei Jiang, Tom Phelps, Travis Wambach, Chengyang Yao, Cooper Levy, Voravit Vorapipat, Xiahan Zhou, Da Ying, and Corentin Pochet for their help and support.

Last, but definitely not least, I would like to thank my family and friends for their never-ending support, encouragement, and understanding as well as for keeping me sane and laughing during the most stressful times.

Since portions of this dissertation have been published in various journals as a result of several collaborations, I must again acknowledge each of the authors for their tremendous contributions.

Chapter 3, in full, is a reprint of the material as it appears in IEEE Transactions on Biomedical Circuits and Systems 2016. Alexander C. Sun, A. G. Venkatesh, and Drew A. Hall, "*A Multi-Technique Reconfigurable Electrochemical Biosensor: Enabling Personal Health Monitoring in Mobile Devices*," IEEE Transactions on Biomedical Circuits and Systems, vol. 10, no. 5, pp. 945–954, 2016. The dissertation author was the first author of this paper.

Chapter 4, in full, is a reprint of the material as it appears in IEEE Biomedical Circuits and Systems Conference 2015. Alexander C Sun, Anthony Au, A. G. Venkatesh, Vikash Gilja, and Drew A. Hall, "*A scalable high-density electrochemical biosensor array for parallelized point-of-care diagnostics*," in 2015 IEEE Biomedical Circuits and Systems Conference (BioCAS), 2015, pp. 1–4. The dissertation author was the first author of this paper.

Chapter 5, in full, is a reprint of the material as it appears in IEEE Journal of Solid-State Circuits 2018. Alexander C. Sun, Enrique Alvarez-Fontecilla, A. G. Venkatesh, Eliah Aronoff-Spencer, and Drew A. Hall, "*High-Density Redox Amplified Coulostatic Discharge-Based Biosensor Array*," IEEE Journal of Solid-State Circuits, pp. 1–11, 2018. The dissertation author was the first author of this paper.

Alexander Chuan Sun

La Jolla, CA

May 2018

VITA

EDUCATION

2012	Bachelor of Science in Electrical Engineering and Computer Science, University of California Berkeley
2014	Master of Science in Electrical and Computer Engineering, University of California San Diego
2018	Doctor of Philosophy in Electrical Engineering (Electronic Circuits and Systems), University of California San Diego

PUBLICATIONS

A. C. Sun, E. Alvarez-Fontecilla, A. G. Venkatesh, E. Aronoff-Spencer, and D. A. Hall, "High-Density Redox Amplified Coulostatic Discharge-Based Biosensor Array," *Journal of Solid-State Circuits (JSSC)*, In Press.

C. L. Hsu, **A. C. Sun**, Y. Zhao, E. Aronoff-Spencer, and D. A. Hall, "A 16×20 Electrochemical CMOS Biosensor Array with In-Pixel Averaging Using Polar Modulation," *Custom Integrated Circuits Conference (CICC)*, San Diego, CA, Apr. 9-11, 2018.

A. C. Sun, E. Alvarez-Fontecilla, A. G. Venkatesh, E. Aronoff-Spencer, and D. A. Hall, "A 64×64 High-Density Redox Amplified Coulostatic Discharge-Based Biosensor Array in 180nm CMOS," presented at the *ESSCIRC 2017*, Leuven, Belgium, 2017.

A. C. Sun, T. Phelps, C. Yao, A. G. Venkatesh, D. Conrad, and D. A. Hall, "Smartphone-Based pH Sensor for Home Monitoring of Pulmonary Exacerbations in Cystic Fibrosis," *Sensors*, vol. 17, no. 6, p. 1245, May 2017.

H. Jiang, **A. C. Sun**, A. G. Venkatesh, and D. A. Hall, "An Audio Jack-Based Electrochemical Impedance Spectroscopy Sensor for Point-of-Care Diagnostics," *IEEE Sensors Journal*, vol. 17, no. 3, pp. 589–597, Feb. 2017.

E. Aronoff-Spencer, A. G. Venkatesh, **A. C. Sun**, H. Brickner, D. Looney, and D. A. Hall, "Detection of Hepatitis C core antibody by dual-affinity yeast chimera and smartphone-based electrochemical sensing," *Biosensors and Bioelectronics*, vol. 86, pp. 690–696, Dec. 2016.

A. C. Sun, C. Yao, V. A.G., and D. A. Hall, "An efficient power harvesting mobile phone-based electrochemical biosensor for point-of-care health monitoring," *Sensors and Actuators B: Chemical*, vol. 235, pp. 126–135, Nov. 2016.

A. C. Sun, A. G. Venkatesh, and D. A. Hall, "A Multi-Technique Reconfigurable Electrochemical Biosensor: Enabling Personal Health Monitoring in Mobile Devices," *IEEE Transactions on Biomedical Circuits and Systems*, vol. PP, no. 99, pp. 1–10, 2016.

B. Hong, **A. C. Sun**, L. Pang, A. G. Venkatesh, D. Hall, and Y. Fainman, "Integration of Faradaic electrochemical impedance spectroscopy into a scalable surface plasmon biosensor for in tandem detection," *Opt Express*, vol. 23, no. 23, pp. 30237–30249, Nov. 2015.

B. Hong, **A. C. Sun**, L. Pang, A. G. Venkatesh, D. Hall, and Y. FAINMAN, "Integrated biosensor for simultaneous detection by surface plasmon resonance and Faradaic electrochemical impedance spectroscopy," in *Conference on Lasers and Electro-Optics, OSA Technical Digest (2016) (Optical Society of America*, 2016), paper JW2A.113.

A. C. Sun, T. Wambach, A. G. Venkatesh, and D. A. Hall, "A multitechnique reconfigurable electrochemical biosensor for integration into mobile technologies," in *2015 IEEE Biomedical Circuits and Systems Conference (BioCAS)*, 2015, pp. 1–4.

A. C. Sun, A. Au, A. G. Venkatesh, V. Gilja, and D. A. Hall, "A scalable high-density electrochemical biosensor array for parallelized point-of-care diagnostics," in 2015 *IEEE Biomedical Circuits and Systems Conference (BioCAS)*, 2015, pp. 1–4.

C. Yao, **A. C. Sun**, and D. A. Hall, "Efficient power harvesting from the mobile phone audio jack for mHealth peripherals," in 2015 *IEEE Global Humanitarian Technology Conference (GHTC)*, 2015, pp. 219–225.

A. G. Venkatesh, **A. C. Sun**, H. Brickner, D. Looney, D. A. Hall, and E. Aronoff-Spencer, "Yeast dual-affinity biobricks: Progress towards renewable whole-cell biosensors," *Biosensors and Bioelectronics*, vol. 70, pp. 462–468, Aug. 2015.

A. C. Sun, T. Wambach, A. G. Venkatesh, and D. A. Hall, "A low-cost smartphone-based electrochemical biosensor for point-of-care diagnostics," in 2014 *IEEE Biomedical Circuits and Systems Conference (BioCAS)*, 2014, pp. 312–315.

PATENTS

Alexander C. Sun, Drew A. Hall. A reconfigurable, multitechnique electrochemical portable biosensor. US and Foreign Provisional Patent

Chung-Lun Hsu, **Alexander C. Sun**, Yunting Zhao, Eliah Aranoff-Spencer, Drew A. Hall. Electrochemical Biosensor Array Devices, Systems, and Methods for Point-of-Care Detection. US and Foreign Provisional Patent

ABSTRACT OF THE DISSERTATION

Point-of-Care and High-Density Array Electrochemical Biosensors

by

Alexander Chuan Sun

Doctor of Philosophy in Electrical Engineering (Electronic Circuits and Systems)

University of California San Diego, 2018

Professor Drew A. Hall, Chair

As a result of numerous advances towards miniaturization in several diverse fields including chemistry, nanofabrication, microfluidics, and electronics, point-of-care (PoC) biosensors have become a promising tool to combat the most life-threatening and expensive health issues affecting the world today. PoC technology helps solve these problems by allowing for diagnostic tools typically restricted to centralized facilities to be brought closer to the point of diagnosis for faster and more frequent testing in both clinical and remote settings. While many biosensor types exist, electrochemical-based detection has the advantage that it is inherently

compatible with circuits, requiring only electrodes for transduction, allowing it fully to benefit from both Moore's Law scaling and the well-established semiconductor manufacturing industry to produce miniaturized, cost-effective, and portable devices. However, there has been a lack of successful PoC electrochemical platforms capable of running multiple diagnostic tests or multi-analyte assays due to the difficultly of balancing power and area constraints of the circuitry with maintaining the required sensitivity.

Therefore, in this dissertation, the circuit and system design of two electrochemical biosensor platforms are presented that explore the challenges of implementing both multi-technique and multi-analyte biosensors at the PoC. The first is a reconfigurable, multi-technique electrochemical biosensor designed for direct integration into smartphone technologies to enable personal health monitoring. By repurposing components from one mode to the next, the biosensor is able to efficiently reconfigure itself into three different measurement modes allowing it to run a variety of assays. Each distinct mode is able to match the performance of state-of-the-art single technique biosensors, while all being integrated onto a single device at a fraction of the size. The 3.9×1.65 cm^2 module was used with a modular smartphone for a variety of real-world point-of-care applications.

Scaling the sensors further for high-density multi-analyte testing, a 4,096-pixel electrochemical biosensor array in 180 nm CMOS is presented. It uses a coulostatic discharge sensing technique and interdigitated electrode (IDE) geometry design to reduce the size of the readout circuitry. Each biopixel contains an IDE with a 13 aA low-leakage readout circuit directly underneath. Compared to standard electrodes, the implemented IDEs along with their inherent 3-D trenches achieve an amplification factor of 10.5× from redox cycling. The array's sensor density is comparable to state-of-the-art arrays, all without augmenting the sensors with complex post-

processing. The simultaneous detection of anti-Rubella and anti-Mumps antibodies in human serum is demonstrated.

Chapter 1

Introduction

1.1 Motivation for Point-of-Care Biosensors

Currently, chronic diseases, such as heart disease, stroke, and diabetes, are the leading cause of death and disability in the United States, with over 50% of the population having at least one chronic illness [1,2]. Furthermore, 87% of the total annual healthcare expenditures ($2.7 trillion in total) are for chronic diseases with 35% of this spending being only for 8.7% of the population [3]. This high death rate and financial cost exists even though in many cases these diseases are preventable or easily manageable. On the other hand, in developing countries, communicable disease, such as respiratory infections, HIV, and TB are the top causes of death [4]. Outbreaks of acute infectious disease are also a major concern as they not only can create a large death toll, but also spread to other parts of the world if unchecked, such as the Ebola outbreak in 2014 that infected individuals in 10 different countries, caused 11,310 verified deaths, and cost $3.6 billion dollars to control [5]. Much like the issues in developed countries, these diseases are

often also preventable or treatable, but, in this case, a lack of adequate healthcare infrastructure makes such solutions infeasible.

One of the main reasons why these problems exist and why the current system is unable to offer an efficient solution is that much of modern medicine is based on a reactive approach to healthcare, which relies on a cycle of doctor's visits and diagnostic tests performed at labs. While this approach works well with treating acute illnesses, it is often inefficient for a number of reasons. Firstly, this system depends on the patient to seek care after symptoms appear, which typically means that the illness has progressed to a somewhat severe state. Furthermore, there is a reliance on access to a centralized facility with trained personnel and expensive test equipment that can take a significant amount of time to return results delaying appropriate treatment. Finally, the patient is typically only a passive recipient of treatment, rather than an active participant in managing his or her own health.

Point-of-care (PoC) biosensors, as shown in Figure 1.1, allow for diagnostic tools to be brought closer to the patient thereby augmenting the current healthcare system by providing more rapid and frequent feedback loops. With PoC devices located near a patient such as at-home diagnostics or wearables, the patient can begin to be more involved in their own health to prevent series issues and manage chronic conditions. More comprehensive testing equipment can also be carried by the physician or in the doctor's office for faster results leading to early treatment and better patient outcome. Finally, the same technology can also be used for rapid and accurate ad hoc testing in remote settings. Hence, moving diagnostic devices closer to the PoC greatly improves the quality of healthcare both in the developing develop parts of the world. However, to make these improvements to the system possible sensitive, low-power, and small-form factor PoC platforms need to be designed.

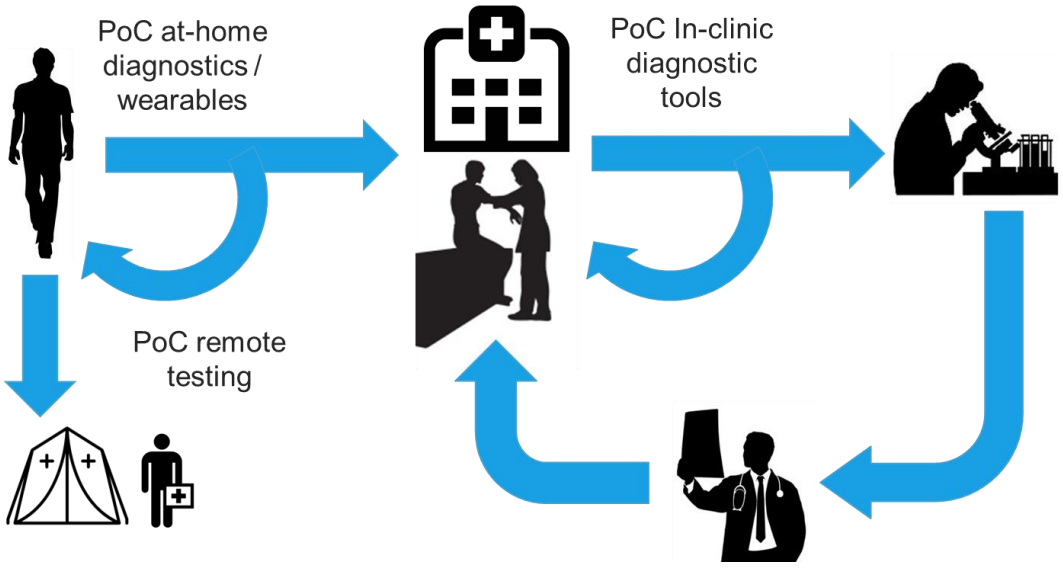

Figure 1.1. Modern healthcare system augmented with PoC biosensors.

1.2 Electrochemical Biosensing

Electrochemical sensors consist of a two or more electrodes submerged in an electrolytic solution to form an electrochemical cell. The "bioelement" or recognition molecule (DNA, antibody, protein, peptide, etc.) is used to isolate the biomarker of interest from all other interferers converting biochemical detection directly into a change in the electrical characteristics of the electrochemical cell. This electrical variation is then transduced by an electrode, typically known as the working electrode (WE), which is made of gold, platinum, carbon, indium tin oxide, etc., to a current or voltage signal to be measured by an analog front-end known as either a potentiostat or galvanostat. The counter (CE) and reference (RE) electrodes are used together in feedback to complete the circuit with the working electrode and properly set a reference voltage in the electrochemical cell.

The electrochemical cell can be modelled in terms of passive electrical components that is known as Randles equivalent circuit. The model consists of a solution resistance (determined by a number of factors including strength of buffer), charge transfer resistance (efficiency of redox reactions), double layer capacitance (formation of ions around a biased WE), and Warburg impedance (diffusion of redox molecules) to model the various electrochemical phenomena that occur within the cell as shown in Figure 1.2. For biosensing, the "bioelement" affects a change in one of these elements either through charge displacement or accumulation, impeding or encouraging the rate of reduction/oxidation reactions, or shifting of the bulk ion concentration. All these occurrences can be sensed directly as an electrical current or voltage, often after applying a potential or current signal to the electrochemical cell. It is worth noting that the need for only a metal or carbon electrode in addition to the measurement circuitry makes electrochemical biosensors ideal for PoC applications because the sensors themselves are highly scalable and can be fully integrated together with circuitry onto the same chip.

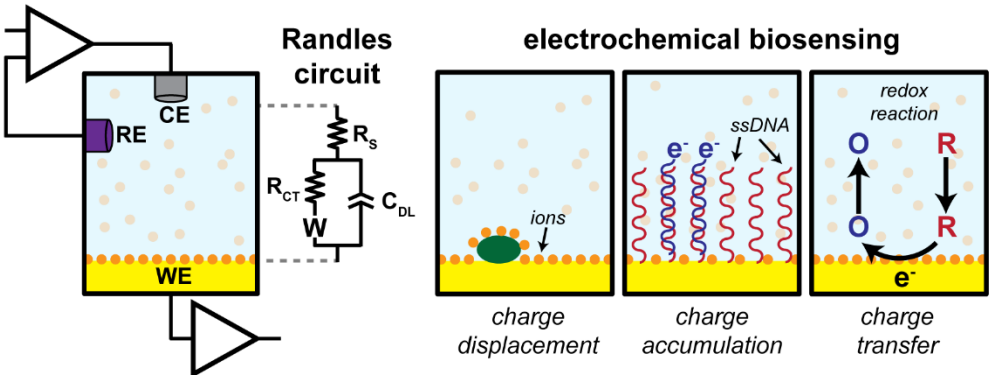

Figure 1.2. Diagram of circuit model and varying modes of electrochemical detection.

1.3 Potentiostat Circuitry

A potentiostat circuit, similar to the standard single channel resistive feedback transimpedance amplifier (R-TIA) or instrumentation amplifier (IA) based designs shown in

Figure 1.3, is used to run electrochemical techniques, which require potential control and current measurement such as cyclic voltammetry, chronoamperometry, and pulse voltammetry each with its own drawbacks and advantages. The technique chosen typically depends on the application as well as the type of assay, so it is crucial for PoC biosensors meant for general diagnostic testing to be able to perform as many techniques as possible. The measurement circuitry must be able to apply a stimulus potential signal between the WE and RE that can be any combination of triangle, square, step, pulse, or sinusoidal waveforms. The applied voltage range is traditionally limited to below 1 V with a resolution of at least 5 mV. The resulting generated current waveform is then measured, which corresponds to the amount of the biomarker detected by the sensor. The signal portion of the waveform is highly dependent on the assay, concentration range of the analyte, and size of the transducer. For the PoC screen-printed electrodes or microelectrodes such signal currents can range anywhere from femtoamperes to microamperes on top of background currents so high sensitivity and large dynamic range is often necessary. Furthermore, the bandwidth requirements typically range from sub-Hz levels to 100 KHz, so contending with $1/f$ noise for some techniques is crucial, while for others extending the bandwidth is necessary, thus integrating more noise. Hence, for enabling multi-techniques, the gain and bandwidth must be adjustable, the input leakage current needs to be a fraction of the expected minimum signal current, smaller if dealing with a high sensor impedance such as ion-selective electrode, and the appropriate noise of the analog front-end (AFE) needs to be filtered or reduced.

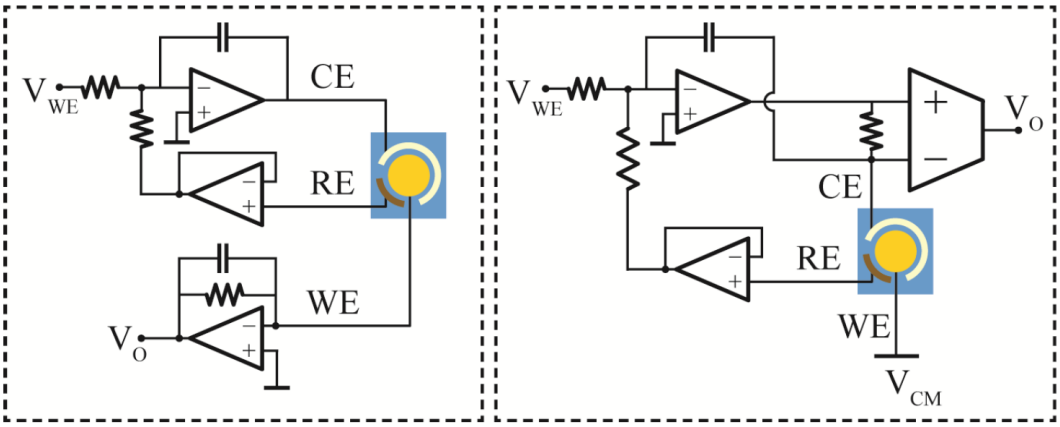

Figure 1.3. Simplified schematics of single channel potentiostat designs from [6].

1.4 Challenges

As discussed before, potentiostats designed for a variety of assays rather than a single application tend to be very sensitive and highly customizable meaning that they can be bulky and consume a lot of power. When moving to a PoC device, there are many challenges that must be overcome. For personal diagnostic devices or wearables, the area the circuitry consumes must be small enough to allow the device to be portable and easy to carry or integrate into a wearable device. More challenging is the limited power available, as the device must now run off of batteries either its own or from a nearby mobile device or harvest energy. When drawing power from a mobile device, it must consume negligible amounts since battery charge is already a precious commodity. These energy sources also mean lower voltage headroom typically regulated to 1.2-5 V reducing dynamic range and making it crucial that gain be programmable to prevent saturation. Furthermore, at this scale, the logic, microcontrollers, mixed signal, and communication circuits also begin consuming a more significant portion of the area and power, leaving only so much available for the AFE to trade for lower noise and leakage. When scaling down to micro-sized electrodes (< 0.01 mm^2) for high-density arrays integrated on chip, which can perform multi-

analyte detection, the area constraint for the in-pixel circuitry becomes an even greater challenge. To match the number of sensing areas used by standard optical based array scanners (< 100 μm spot size) without consuming too much expensive silicon area, sensor pixel sizes typically are less than 0.01 mm^2. This means that the in-pixel circuitry containing the AFE can become the limiting factor determining the density of the array. Furthermore, scaling the size of the electrodes more than 1,000× decreases the current signal generated proportionally, requiring both increased sensitivity and reduced size of the measurement circuitry.

1.5 Scope of Dissertation

This dissertation presents the development of the measurement circuitry for PoC and high-density array biosensors for multi-technique devices and multi-analyte sensing. In Chapter 2, the current ecosystem of PoC electrochemical biosensors for mobile health, or mHealth, applications is discussed. Chapter 3 introduces a single-analyte multi-technique reconfigurable electrochemical biosensor for integration directly into mobile devices or wearables. Advancing to multi-analyte sensing, Chapter 4 presents a highly scalable electrochemical biosensor scheme intended for high-density parallelized PoC diagnostics. Chapter 5 goes over the full-scale integrated version of this high-density coulostatic discharge-based array using redox cycling to amplify the minute signals. Finally, Chapter 6 presents concluding remarks and future research directions.

Chapter 2

mHealth-oriented Electrochemical Biosensors

2.1 Introduction to mHealth for PoC Diagnostics

As of 2017, 63% of the world's population use mobile phones, and 31% specifically have a smartphone [7]. In the United States, the number of adults with smartphones has already reached 77% with 12% being "smartphone only" users without a household phoneline or internet [8]. This growth can also be seen in other regions of the world such as Africa, Asia Pacific, and the Middle East that account for 80% of all new mobile phone subscriptions [7]. This overwhelming data clearly shows that mobile phones and, increasingly so, smartphones have become a ubiquitous part of everyday life around the world. Having what is essentially a very powerful network connected portable device attached to almost everyone, presents a tremendous opportunity to the leverage this technology to developed PoC biosensors that offer the user portable and convenient diagnostic testing. This trend that involves utilizing mobile phones to support medical and public health practice has been coined as mobile health or mHealth.

Due to the widespread availability of mobile phones, there have recently been a large influx of mHealth biosensing peripheral modules that attach to smartphones to take advantage of their computing power, network connectivity, battery, and camera in order to offload as much of the biosensor components as possible onto the phone itself. Therefore, much more streamlined devices can be produced that consume less power and area and are less expensive compared to equivalent stand-alone biosensors. It is worth noting here that while much of the smartphone-based biosensor ecosystem consists of optical based sensing that uses the camera to measure fluorescent or colorimetric assays [9–11], the following sections will only focus on electrochemical sensing. These optical techniques are typically limited by the resolution and focus of the smartphone camera as well as ambient lighting conditions [12]. On the other hand, electrochemical measurement has the advantage of being mostly independent of the smartphone's capabilities while still achieving a comparable or better formfactor than optical peripherals.

2.2 Integration with Smartphone and Mobile Devices

A number of different ways to integrate a peripheral module to a phone have been developed all with distinct trade-offs in terms of available power, data rate, and compatibility with different makes and models.

2.2.1 Proprietary Port

Proprietary ports such as USB-B or Apple's lightning port have been widely used as a method to both provide power to the peripheral and send bidirectional data [13–17]. Typically, no additional power source other than the phone is required in this case removing the hassle of charging or replacing an extra battery, which can lead to better patient adherence to frequent testing. The lack of a battery also can greatly reduce the bulk and size of the peripheral device.

The amount of available power from these interfaces is also very high with USB rated to provide a maximum of 2.5 W. This amount of power is more than enough when designing electrochemical measurement circuitry, which at most have been shown to consume 400 mW [17]. However, interfacing with these ports requires the addition of a USB interface chip (such as the CH372 or FT232R), which is essentially an additional microcontroller, that handles the lower layer USB protocol between the phone and onboard logic [14,17]. Furthermore, compatibility between smartphone devices is very limited when using only the proprietary interfaces. A device produced specifically for a certain smartphone type would need to be redesigned in order to be compatible with a different make or model. For example, a different interface would be required when switching between old and new models of the iPhone, from iPhones to Android phones, from USB-C to USB-B devices, and even between various feature phones.

2.2.2 Audio Headphone Port

The 3.5-mm audio port intended for connecting headphones can be used as an interface between a peripheral device and mobile phone. This port allows for both bidirectional data transfer via the microphone terminal and one of the output channels (left or right ear) and power transfer from the phone using the remaining output channel. When used as the interface for power and communication for a peripheral device, the headphone jack's main advantages are that it is both the only truly universal I/O port that exists on all smartphones along with feature phones and has remained entirely unchanged throughout many generations of smart devices (expect for the iPhone X, which requires an adapter). Hence, mHealth peripherals that use the headphone jack are essentially hardware compatible with all devices that have a three terminal audio port including laptops, tablets, mp3 players, and older mobile phones. Similar to devices that use the proprietary

ports, taking power from the audio jack means that no additional battery is required. However, since this port is AC coupled (bandpass from 20 Hz to 22 kHz) to prevent damaging headphones, no DC signals can pass through requiring both rectification of the audio output for power and modulation / demodulation of control and data signals.

2.2.2.1 Power Harvesting

As is demonstrated in prior art, an output sinusoid from the audio channel can be rectified with a MOSFET H-Bridge and Schottky diode for to obtain a 1.2 – 4 V that can be further regulated and filtered [6,18–20]. However, since various makes and models of smartphones use different audio drivers, the output characteristics of different headphone jacks can vary. Figure 2.1 shows the measured values of both the output resistance and available power for a wide variety of smartphones. The resistances and maximum power available range from 1-20 Ω and 3-80 mW, respectively. The variation in output resistances can negatively affect the matching between the phone and the power harvesting circuitry leading to further reduced power. To account for this, an automatically tunable matching network can be added to the peripheral device in order to change the input impedance of the harvester and improve overall power transfer efficiency. This technique has been demonstrated to improve efficiency from 52% up to 85.4% [20,21]. Even with this improvement, however, the power consumption of biosensors that use the audio port must still be low enough in order to remain compatible with most smartphones. As a result, all the peripherals in this space consume the least power (2.5-6.9 mW) when compared to other smartphone-based biosensors, aside from those that use NFC [6,19,21].

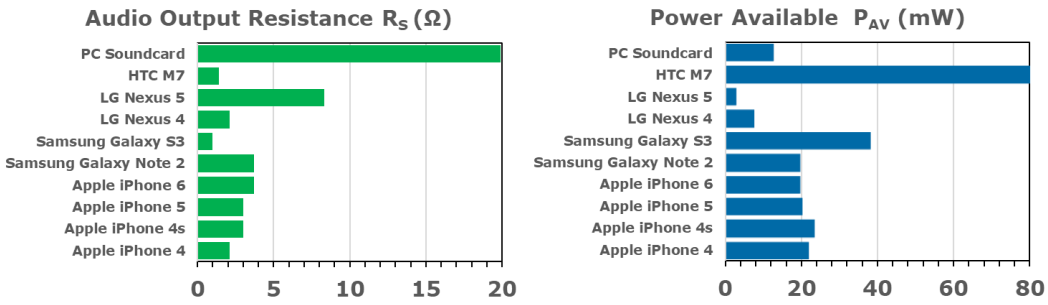

Figure 2.1. A survey of the output resistance and power available for a set of popular smartphones.

2.2.2.2 Data Transfer

Signal transmission via the audio port can be accomplished in a number of different ways. Frequency shift keying (FSK) at ~17 bps handled by an on-board microcontroller can facilitate digital transmission between the smartphone and peripheral device as is demonstrated in Nemiroski 2014 and Sun 2017 [18,22]. In Wang 2015 [23], a phase-locked loop (PLL) (TI CB4046B) with active filters is used to demodulate a frequency signal from the smartphone to a voltage ramp stimulus for the potentiostat to run cyclic voltammetry. Another PLL is used to modulate the output of the potentiostat back to a frequency signal to transmit it to the phone to be quantized. This design does not require an onboard digital-to-analog converter (DAC), analog-to-digital converter (ADC), or microcontroller, instead offloading most of this functionality to the smartphone. However, the ability to set the test parameters including scan rate and voltage range is limited because the absolute voltage and slope of the ramp are dependent on each other. In Sun 2016 [21], bidirectional data was instead handled by a low power microcontroller sending and receiving UART packets in order to set the test parameters for cyclic voltammetry. The ramp signal was then generated on-board using a PWM generator and integrator with feedback to a course ADC to insure accuracy. The output of the potentiostat was then converted into a frequency by a

555-timer-based voltage-controlled oscillator (VCO) modulated with marker tones to ensure that the measured data lines up with the stimulus voltage. This frequency signal is then sent to the phone to be quantized. This design is able to independently set the voltage range and scan rate, while still consuming low enough power to be powered off of the audio jack. Jiang 2017, similar to Wang 2015, completely does away with using a microprocessor, instead relying on frequency and voltage modulation of the audio output channel along with frequency and amplitude detection circuits to control the EIS biosensor [19]. This design allows the peripheral to achieve a low 2.5 mW maximum power consumption and power itself directly from the audio port.

2.2.3 Bluetooth

Recently more and more mHealth peripherals have begun using Bluetooth to wireless transmit data to and from the smartphone [24–35]. The obvious benefit is that these types of peripherals are compatible with all types of smartphones regardless of the make or model. Also, since some companies have been shifting towards replacing most wired interfaces with wireless ones, using Bluetooth connection appears to be more future proof than the headphone port. However, a wireless biosensor dongle requires an additional battery that must be either replaced or recharged in addition to the smartphone. In addition to an extra battery and Bluetooth radio module (such as HC-06, HM-10, TI CC2541, Bluegiga WT-12), these types of peripherals must also generate all the voltage stimulus signals as well as quantize the potentiostat output on-board.

2.3 PoC Implementations of E-chem Techniques

2.3.1 Amperometry

For potential controlled current measurement techniques such as chronoamperometry (step input), cyclic voltammetry (triangular waveform input), and pulse voltammetry (pulse train input), most mHealth devices either use a commercially available AFE i.e., TI LMP91000, or a custom potentiostat circuit. The advantage of LMP91000 is that the entire AFE is completely integrated into a single chip in a 4×4 mm^2 package that consumes ~40 µW. The detectable current range for this chip is 5-750 µA, which is acceptable for applications such as blood glucose measurement where concentration of the analyte is generally high [35], but not sensitive enough for many other assays. Instead, when power can be traded for lower noise and smaller input bias current, custom potentiostat circuits with resistive feedback transimpedance amplifiers (R-TIA) as in Figure 1.3 are designed to obtain a higher current resolution. The open source "CheapStat" potentiostat has a current resolution of 1 nA with tunable gain from 33-165 kΩ [26,36]. Fan 2017 demonstrates a custom Bluetooth potentiostat that also achieves a current resolution of 1 nA and limit-of-detection (LOD) for neuron-specific enolase of 22 pM using differential pulse voltammetry (DPV) [27]. Sun 2016 also obtains a ~300 pA current resolution with a LOD for secretory leukocyte protease inhibitor (SLPI) of 1.4 nM using CV in an audio-jack powered peripheral. Jung 2017 and Pechlivanidis 2017 also both report current resolutions for their Bluetooth based biosensors of 400 pA and 122 pA, respectively [17,29].

2.3.2 Potentiometric

Potentiometric measurement circuitry typically only requires an amplifier with a large input impedance to measure the voltage from an ion selective electrode known for its high resistance (10 MΩ – 1 GΩ). In Zhang 2015, a USB powered non-inverting amplifier with a input

bias current of ~20 nA is used and can achieve a LOD of α-amylase of 89 nM [14]. There also exists a commercial potentiometric measurement chip, i.e. LMP91200, which is essentially an ultra-low leakage buffer (600 fA), that has been used in audio-jack biosensors [18].

2.3.3 Electrochemical Impedance Spectroscopy

Electrochemical impedance spectroscopy (EIS) is typically measured by applying a small sinusoidal voltage stimulus between electrodes and measuring the magnitude and phase of the resulting current signal at multiple frequencies in order to calculate an impedance spectrum. Due to the typical frequency range 1-100 kHz and the low 5-mV peak amplitude of the stimulus signal, EIS tends to be the most power consumptive measurement technique since it needs to accurately measure both magnitude and phase accurately from a small current signal at all frequencies within the spectrum. Hence, most of the mHealth oriented EIS sensors require power sources such as a 9 V lithium ion battery. As with the other two measurement modes, there exists a popular commercial IC solution, AD5933, which is able to fit a complete digital signal generator (DDS) core, DAC, ADC, and discrete Fourier transform (DFT) hardware into a single small chip [24,25,30]. However, the main issues with this IC are that the smallest potential stimulus it can apply is ~200 mV peak-to-peak and the bias point cannot be set independently of the amplitude. In most cases, EIS measurements need to be fitted to a linear impedance model. With a high stimulus amplitude, it can no longer be assumed that the data matches this linear model. Furthermore, in assays where there are redox reactions, setting the bias point accurately is crucial to the measurement. Custom EIS circuits have been created to obtain more accurate results that use on-board ADCs, DACs, and microcontrollers relying on separate batteries to provide enough power [31,33]. However, Jiang 2017 shifts the generation of the stimulus signal and quantization

to the smartphone through the headphone jack, negating the need for a microcontroller and mixed-signal circuits allowing for a very low power (2.5 mW) EIS peripheral, which is mostly analog [19].

2.4 Summary

The current ecosystem of mHealth PoC electrochemical biosensors was explored and the different types of interfaces were compared to demonstrate the trade-offs of each. Overall compatibility with smartphones, amount of available power, whether an external power source is required, and the sensitivity of the potentiostat circuitry was examined. While each type of peripheral biosensor has its own advantages and optimal use cases, carrying around multiple dongles for different PoC assays in unrealistic. Hence a device that combines all the techniques and benefits together into a single biosensing platform would greatly improve the practicality of mHealth PoC biosensors. Furthermore, all of the current mHealth biosensor devices are for single-analyte detection, and further improvements in the measurement circuitry are required to be able bring multi-analyte measurement into the mHealth space.

Chapter 3

A Multi-Technique Reconfigurable Electrochemical Biosensor: Enabling Personal Health Monitoring in Mobile Devices

3.1 Introduction

Chronic illnesses, such as heart disease, stroke, cancer, and diabetes, are not only the leading cause of death and disability in the US, but also the most commonly diagnosed and expensive health issues to treat [2]. One of the many reasons for this phenomenon is the heavy reliance on periodic hospital checkups as the sole mechanism to determine one's well-being. While remote and at-home testing is a promising solution to help alleviate this burden on the healthcare system and potentially improve one's health, most medical diagnostic equipment today is confined to centralized laboratories and hospitals. Furthermore, this equipment is too expensive and bulky for direct PoC use.

Fortunately, recent advances in portable electronics and sensor miniaturization have allowed for the development and proliferation of mHealth technologies that can continuously

monitor patients at the PoC, away from traditional hospital settings. Many mobile devices have fitness-oriented sensors built-in, such as accelerometers for tracking physical activity, electrocardiograms (ECG) to record the electrical signals of the heart, and photoplethsymogram (PPG) to determine heart rate as well as the blood oxygenation level. Unfortunately, these sensors offer limited medically actionable data, especially for those with chronic diseases. Biomolecular sensors, on the other hand, that measure the constituents of biological samples (e.g., blood, urine, saliva, etc.) provide a much more complete and medically relevant picture of the user's health. Such sensors could be used for at-home diagnosis of infection, monitoring of treatment progression [13,22,37], hydration and fatigue tracking during exercise [38], and testing food and water safety [22,23,39–41].

While several add-on biosensing modules for mobile phones have been developed that leverage intrinsic hardware such as the camera, Bluetooth, USB, and audio port [6,13,22,23,37–48], these devices are still external to the phone making them more burdensome to manage and transport than a fully integrated solution, dissuading frequent use. By integrating biosensors directly into a smartphone or smartwatch and leveraging the scalability, cost-effectiveness, and accuracy of electrochemical biosensing, which led to the success of glucose meter, one can develop much more accessible and seamless mHealth applications that promote adherence to frequent or continuous testing. Furthermore, in addition to being a boon for those who live with chronic illnesses, biosensors integrated into everyday items also enable other individuals who are either at risk for disease, trying to improve health and fitness, or curious about their well-being to routinely monitor themselves.

To this end, we describe the design of an electrochemical biosensor module for direct integration into a smartphone or wearable through the use of a reconfigurable bipotentiostat

capable of both supporting an extended range of techniques and, at the same time, conforming to the challenging size and power consumption constraints set by continually shrinking portable devices. While enabling a wide variety of tests would typically consume additional area and power, this design alleviates the problem by repurposing the same components in different measurement modes, ultimately reducing the redundancy. The entire platform (Figure 3.1) consists of the sensing module that houses the reconfigurable potentiostat that is meant to be built into a mobile device, an external sensor (disposable test strips, screen-printed electrodes, ion selective electrodes, etc.), and the mobile device itself. Since the external sensor component is in contact with the biological sample and is meant to be disposable, it is not permanently integrated into the smartphone like the rest of the module. However, when compared to non-integrated biosensors, which have this same external sensor constraint, smartphone integration ultimately eliminates having to carry around an extra hardware component thereby increasing accessibility. The mobile platform used in this work is Google's Project Ara modular smartphone, which allows the user to swap out different components and customize the phone’s hardware. This platform is ideal for biosensor integration because of its open and high-speed interface as well as its modularity that enables the smartphone to have biosensing, amongst many other, capabilities.

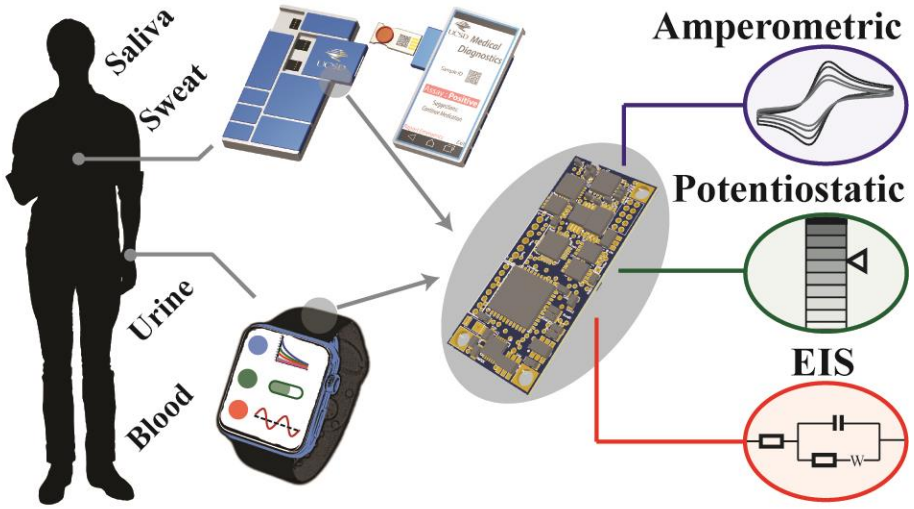

Figure 3.1. Illustration showing potential uses for the multi-technique biosensor platform integrated into smartphones and wearable devices.

3.2 Electrochemical Sensing Background

As with other state-of-the-art PoC electrochemical biosensors, the most crucial component is the potentiostat, or the analog front-end, that interfaces with and controls the electrodes in contact with the sample. A typical electrochemical cell consists of a working electrode (WE), where the biochemical reaction occurs, and a reference electrode (RE), usually working in tandem with a counter electrode (CE) to set the potential of the cell. While there are numerous types of techniques which the potentiostat can conduct, each with varying sets of parameters, requirements, and advantages, all these methods essentially measure different aspects of the same phenomenon: the movement and displacement of charge at the interface between an electrode and an electrolytic solution, also known as an electrochemical cell. Equivalent circuit models of this electrochemical cell can be used to better understand the sensing mechanisms of various electrochemical techniques, thereby guiding the design and implementation as well as setting the requirements of the circuits tailored for each distinct test type.

Randles equivalent circuit [49], shown in Figure 3.2 for a three electrode system, is the most widely used electrical model for characterizing the electrode-solution interface, and contains four main components: double-layer capacitance (C_{dl}), charge transfer resistance (R_{ct}), Warburg impedance (Z_{Warg}), and solution resistance (R_s). C_{dl} is a combination of the capacitance of the electrode itself and the capacitance generated by layers of ions and charged molecules forming at the surface of the electrode due to electrostatic forces. C_{dl} is not a strict capacitance, and is typically modelled as a constant phase element with an impedance of $Z_{dl} = \frac{1}{(j\omega)^m C_{dl}}$, where m is the phase parameter. Typically, C_{dl} ranges from 0.1-1 μF/mm^2 and is highly dependent on the salt concentration in solution as well as the voltage of the electrode [49,50]. R_{ct} captures the transfer of electrons between the solution and electrode from reduction and oxidation reactions of molecules close to the surface. This resistance is typically ~10-100 kΩ or approximately infinite in cases without the presence of redox molecules (non-faradic measurements) and varies with the concentration and type of molecule as well as the materials and voltage bias of the electrode. Z_{Warg} models the diffusion of redox molecules to and from the surface. Similar to C_{dl}, it also is a constant phase element component, but always with a 45° phase shift. Finally, R_s models the ions drifting in bulk solution and is set by the solution conductivity and applied voltage. Depending on the measurement technique, different components of this model become important to the design of the potentiostat.

Amperometry is the standard method to perform most sensitive labelled assays, which use enzymatic tags that transduce and amplify a detection event into a measurable electrochemical signal. The circuitry for amperometric techniques [51–53] applies a voltage waveform between the WE and RE using the CE to reduce voltage error while measuring the corresponding generated current signal at the WE, which is proportional to the concentration of the biomarker. For example,

cyclic voltammetry (CV) and linear sweep voltammetry (LSV) both use slow (10-100 mV/s) ramps (< 1 V sweep range) to stimulate the electrochemical cell, while step-techniques such as chronoamperometry (CA) and square wave voltammetry (SWV) instead use pulsed voltages (a single step for CA and 10-100 Hz for SWV). In the majority of amperometry, the objective is to measure the current due to a particular redox reaction rather than from the faster charging and discharging of C_{dl}, referred to as background current. Even in pulsed techniques, the sections of the current measurement that contains the signal occur after the output has settled. Hence, amperometry necessitates precise voltage control and high measurement sensitivity for slow large signal currents.

While ions cannot be easily measured with traditional labelled assays or DC current measurements, their inherent charge and size allows them to be detected via potentiometric tests. Ion-selective electrodes (ISEs) separate specific ions with a semi-permeable membrane between two electrodes, thereby creating a potential difference (~0.1-100 mV) proportional to the amount of that ion concentration in the solution. However, due to the nature of these sensors, their impedance is very high, roughly on the order of 100 MΩ, necessitating high resolution sampling of the electrode voltage with a high input impedance.

For label-free electrochemical assays, electrochemical impedance spectroscopy (EIS) is most often used since it measures changes in impedance on the surface of an electrode due to displacement of charge (ΔC_{dl}) or impeding of redox reactions (ΔR_{ct}). Although there are many different circuit topologies that can implement EIS [54–56], generally they all apply small amplitude (<10 mV) voltage sinusoids of varying frequencies (0.1 Hz – 100 kHz) between a two electrode cell and record the resulting current. For each frequency, the magnitude and phase change is calculated and used to find the complex impedance ultimately forming an impedance spectrum

that can be fitted to the Randles circuit. Unlike in traditional amperometry where aligning the timing of the input and output waveforms is often not necessary, EIS circuitry must not only have high enough bandwidth to measure these small signal AC currents but also have the ability to accurately track phase change between the applied voltage and measured current. Furthermore, any frequency dependent phase shift introduced by the measurement circuitry must be calibrated out.

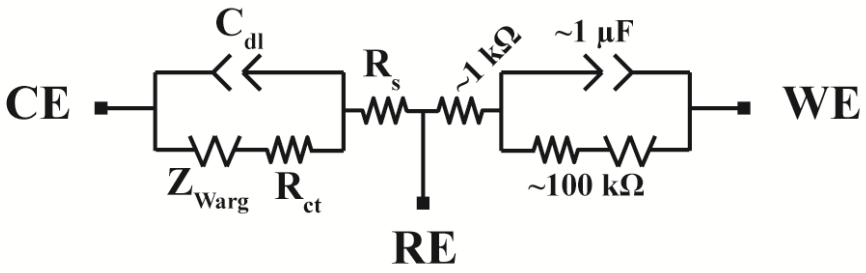

Figure 3.2. Randles equivalent circuit model for a three-electrode system.

3.3 Design of Reconfigurable Module

In this work, the potentiostat discussed is based on a well-studied and commonly used topology in electrochemistry [57,58], and is an expanded and improved version of our previous work [59]. However, to enable a large set of possible mHealth applications, the potentiostat must be able to run multiple types of techniques discussed above, which require different sensing modes and additional circuitry. Each of these various types of tests would typically require a different and separate set of circuitry. However, space and power are highly constrained resources on a mobile device and commodities must be shared with the device's other components. Therefore, in order to reduce the area and, more importantly when moving to an integrated circuit implementation, the power, a single reconfigurable design (Figure 3.3), rather than three different sets of potentiostat circuits, is used that repurposes components from one mode to the next while maintaining

performance across different techniques. Hence, the potentiostat is designed to support three distinct techniques: 1) amperometric, 2) potentiometric, and 3) impedance spectroscopy.

To further increase the flexibility and compatibility of the platform with PoC type of tests, the potentiostat includes dual WEs each with its own resistive feedback transimpedance amplifier (TIA), which is based on circuit topology commonly used in potentiostats [36,60,61]. Using networks of switches that can switch between a range of different resistors and capacitors, each TIA has independently adjustable gain (10 kΩ, 100 kΩ, and 1 MΩ) and bandwidth (1 Hz – 100 kHz), expanding its dynamic range and allowing it to measure different types of biomarkers that have varying sensitivity requirements. This dual WE functionality also enables two tests of the same technique to be run simultaneously on the same sample, allowing one to either be a control to compensate for factors such as temperature variation or background signals, or an additional sensor for another biomarker. In order to take advantage of this parallel testing, an assay must either generate no free-roaming redox molecules that can diffuse between electrodes and cause interference (e.g. label-free assays) or use an electrode design that physically isolates or spreads out the sensing surfaces using wells or additional sample collection channels. Alternatively, the two electrodes can be used together for redox cycling with an interdigitated electrode in order to chemically amplify the signal for higher sensitivity, particularly when dealing with micro- and nano-scale sensors [62]. The common-mode voltage is adjustable to accommodate and optimize the various current and voltage ranges, which can be skewed either to the positive or negative side depending on the expected response. The different configurations and respective performance are discussed in the following sections.

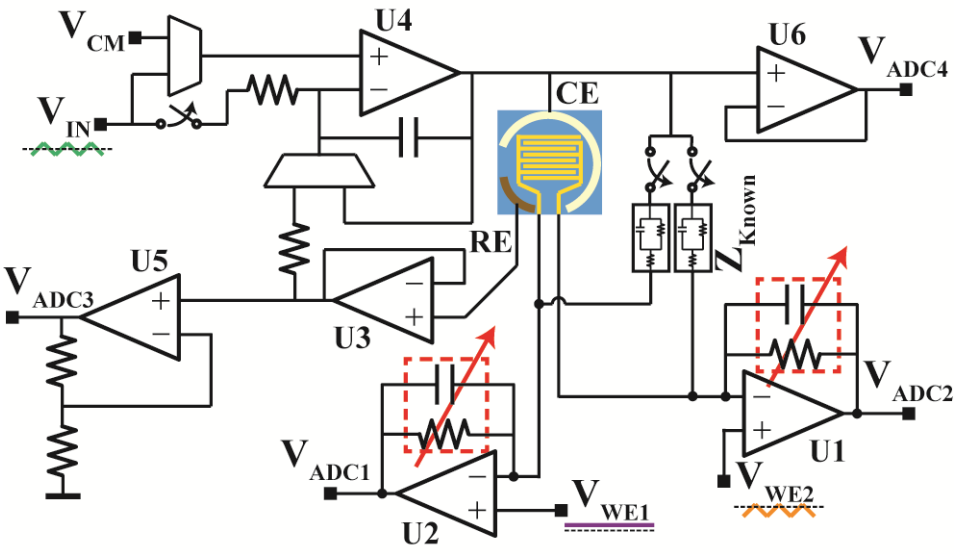

Figure 3.3. Schematic of reconfigurable potentiostat where V_{CM}, V_{IN}, V_{WE1}, and V_{WE2} are DAC outputs and V_{ADC1-4} are ADC inputs.

3.3.1 Amperometric

The potentiostat configuration for this mode is shown in Figure 3.4. A voltage signal is applied to the three-electrode sensor between the RE and the WE, with the CE supplying the current to set the solution potential. This voltage waveform, which varies depending on the technique chosen, generates a current signal in the solution that is measured at the WE, in this case, with a resistive feedback TIA. To expand the possible applications of the device, this potentiostat version has two working electrodes with each channel having TIAs with independently configurable gain and bandwidth (adding either 1, 10, and 100 nF capacitor in parallel with the feedback resistance). The variable gain allows the device to adjust for the different baseline currents and varying physiological concentration ranges of different biomarkers, assays, and sensor areas. Also, since different amperometric techniques excite the electrochemical cell with different input voltage waveforms, the bandwidth of the generated current signal can vary.

Since the sensitivity of these measurements depends on how accurately current can be measured, the most important design considerations for this mode are the input-referred noise of the TIA and the current leakage at the WE node. Hence, all the switches where chosen to have low leakage (<20 pA) and the opamps (U1 and U2, Analog Devices AD8552) were selected to balance the power, input bias current (160 pA), and noise. The requirements at the other electrodes are less constrained. The input bias current of the RE circuitry must be minimized in order to reduce the IR error of the applied voltage. By using a very low input bias opamp (U3, Analog Devices AD8691) chosen specifically for the potentiometric mode (described later), this design achieves an RE leakage of 200 fA, which, with a typical solution resistance of 100 Ω, contributes a negligible 100 nV error. Furthermore, since the CE, which is controlled by U4 (Texas Instruments OPA2333), only needs to be able to supply the necessary current to the cell for this mode, the parameters for the control circuitry are set by the EIS mode.

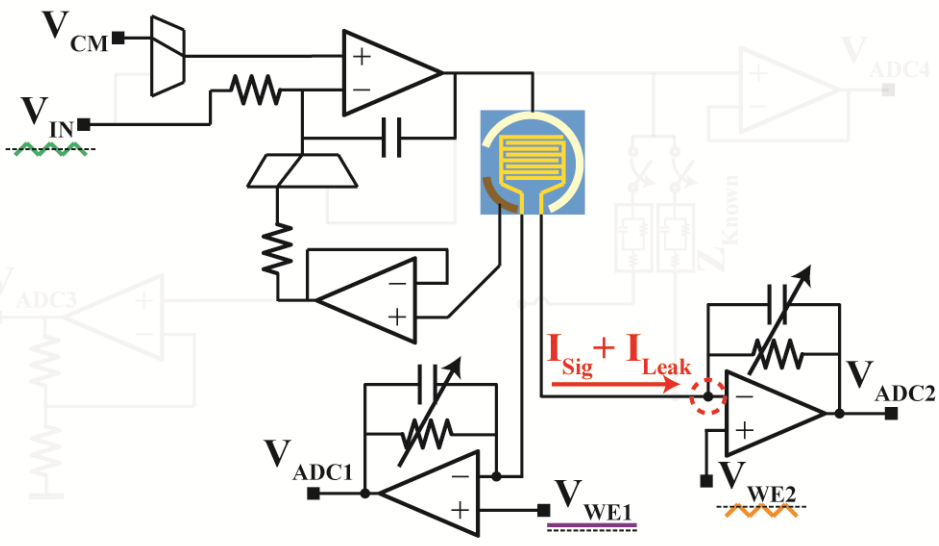

Figure 3.4. Simplified schematic of the potentiostat in amperometric mode.

3.3.2 Potentiometric

In the potentiometric mode (Figure 3.5), the voltage generated between two electrodes in a solution is measured. Typically, an ISE requires measurement circuitry with an input bias current of less than 1 pA to ensure that measurement error is less than 1%. Without adding a new set of components, the input buffer used for RE in the amperometric mode is switched into the signal path for use as a high impedance input with a working electrode operating as the other terminal. By adjusting the bandwidth switches to provide a short, the WE circuitry in this case operates as a buffer and allows the voltage from sensor to either be sampled single-ended or pseudo-differentially to reject common-mode signals.

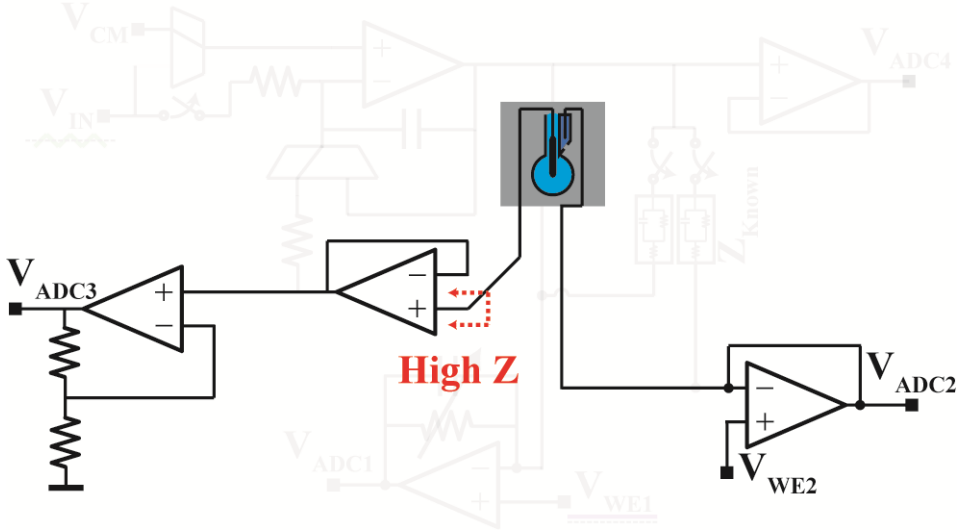

Figure 3.5. Simplified schematic of the potentiostat in potentiometric mode.

3.3.3 Impedance Spectroscopy

In the EIS mode (Figure 3.6), a two-electrode sensor is attached between the CE and a single WE, with the option of attaching an additional sensor on the other WE. Small signal (20 mV) voltage sinusoids, with varying frequency from 1 Hz – 10 kHz, are applied between the two

terminals and the WE measure the resulting current. The gain and bandwidth of the WE TIA is adjusted depending on the impedance and frequency being measured, changing if the signal is too small or if the channel becomes saturated. In the two other modes, the open switches and unused electrodes are always low impedance nodes set to known voltages in order to avoid instability and interference. However, in the EIS mode, the RE input is left floating in the circuitry in order to avoid the leakage current from adding a switch at this node, which is crucial for accurate amperometric and potentiometric measurements. However, the RE can be tied directly to the CE through a short on the electrode without affecting the impedance measurements as it can be incorporated into the calibration.

Making the approximation that the system is linear, due to the stimulus being small, the complex impedance Z_{Cell} is computed as:

$$Z_{Cell}(j\omega) = H(j\omega)\frac{V_{IN}(j\omega)}{V_{OUT}(j\omega)} \tag{3.1}$$

where $H(j\omega)$ is the transfer function that converts the current to voltage, V_{IN} is the voltage sinusoid applied to the Z_{Cell}, and V_{OUT} is the voltage read by the ADC. $H(j\omega)$ in not only dependent on the feedback network of the TIA, which changes depending on the cell impedance, but also other factors such as parasitics in the switching networks and phase shift in the signal path. Hence, to account for varying $H(j\omega)$ and compensate the channel accordingly, known test impedances (Z_{Known}) measured prior to use, one for each WE, are switched in between the two electrodes, given the same stimulus, and measured at each frequency before the actual sensor is tested.

$$\begin{aligned} H(j\omega) &= Z_{Known}(j\omega)\frac{V_{IN}(j\omega)}{V_{Measured}(j\omega)}, \\ Z_{Known}(j\omega) &= R_s + \frac{1}{j\omega C} \| R_{ct} \end{aligned} \tag{3.2}$$

Using known impedance measurements, the transfer function of the channel can be determined for each frequency (Eq. 2) and used to calibrate the impedance measurements in software on the host device [63]. Furthermore, to ensure that the input signal is correctly aligned with the output, the ADC simultaneously measures the CE voltage, thereby reducing phase error introduced by the control circuitry.

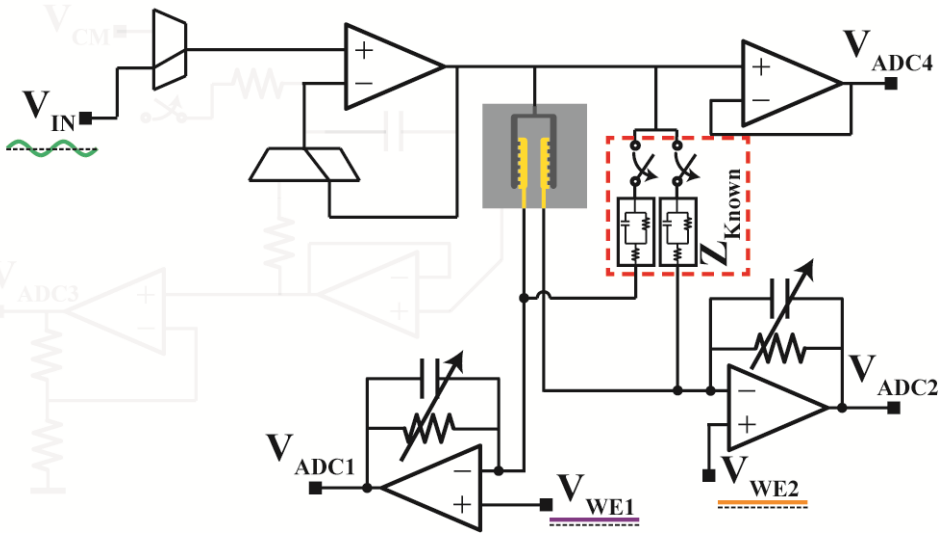

Figure 3.6. Simplified schematic of the potentiostat in EIS mode.

3.4 Integration with Mobile Technology

Shown in Figure 3.7a, aside from the potentiostat, the module also contains a power regulation network, a DAC (Analog Devices AD5685R), an ADC (Analog Devices AD7682), and a microcontroller (Microchip dsPIC33EP256MC204). This periphery circuitry can be easily tailored to the specifications of the wearable or mobile device. The design takes its power from the host device with an input voltage anywhere from 2.5 to 5.5 V and with a light-load efficient buck-boost DC-DC converter (Texas Instruments LM366SD) in series with two LDOs (Texas Instruments TPS79101) regulates it to both a 4 V and a 3.3 V thereby isolating the analog and

digital supplies. The DAC (14-bits) and ADC (16-bits) both have 4 channels, and, via SPI, their maximum update and sample rates are ~200 kHz. The microcontroller controls the potentiostat during testing by updating and sampling from the proper DAC and ADC channels respectively. The microcontroller also communicates with the host device via serial communication (either SPI, I^2C, or RS-232 depending on the mobile device interface) and configures the potentiostat with the proper settings. In order to integrate this module into a mobile device that is not a modular smartphone, an internal I/O port needs to be accessible. While this communication between the module and processor would usually be through a proprietary communication protocol, it is reasonable to expect that for mobile devices that use different types of sensors (such as accelerometers and pulse oximeters) the translation hardware is already available that implements the required communication interface between sensors and the high-speed processor bus. Hence, adding this module would be as simple as integrating any other sensor.

A 3.9×1.65 cm^2 4-layer PCB (Figure 3.7b) with discrete ICs was fabricated to fit into the Google Project Ara smartphone as a 2×1 sized module and work with an Android application (Figure 3.7c). Furthermore, this current prototype is small enough to be considered compatible with wearable devices as well. The module communicates with the Spiral 1 Ara platform via the I^2C serial communication pins of the microcontroller. For testing purposes, we used several off-the-shelf sensors that each have varied connectors. Hence, an interposer board to accommodate all the electrodes was also constructed and attaches to the top or bottom of the module. Since the sensing areas are smaller than the module itself, actual developed and complete mobile devices can have the sensor or the sensor holder, in the case of disposable test strips, mounted directly into the shell of the device without altering the form factor.

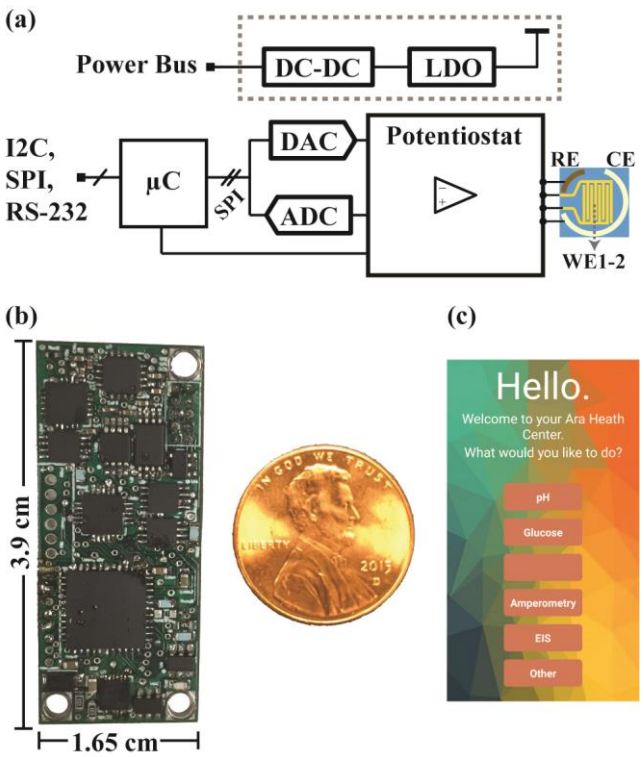

Figure 3.7. a) Block diagram of the entire module b) Photograph of PCB next to a US penny for scale c) Screenshot of smartphone application interface.

3.5 Electrical Measurement Data

Each of the three modes were characterized and tested to verify their functionality. For the amperometric mode, since the sensitivity of these measurements depends on how accurately current can be measured, the most important design considerations for this mode are the input-referred noise, which was measured with 100 kΩ gain and a 1 kHz bandwidth to be 216 pA_{RMS}, and the leakage current at the input of the TIAs or WE. Since low leakage switches for selecting the gain and bandwidth are used and the number of connections to the inverting node are minimized, the overall input leakage (~180 pA) is dominated by the input bias current of the opamp. Hence, we can measure bidirectional currents ranging from ~500 pA to 200 µA, which is ideal for most PoC applications. For the potentiometric mode, the input bias current of the

measurement circuitry is ~200 fA, setting the approximate input impedance at 5 TΩ. The input referred voltage noise is 1.060 μV_{RMS} (10 Hz bandwidth), and the voltage offset is ~400 μV. For EIS, when testing a known impedance of 100 kΩ in parallel with 1 μF from 1 Hz – 10 kHz, the module was measured to have a 5% magnitude and a 6° phase error as compared with a benchtop EIS tool. This configuration and calibration scheme described previously can measure an impedance range of 50 Ω - 10 MΩ.

To demonstrate the reproducibility and stability of all modes, a series of repeated measurements (N = 100) on known inputs was performed using both the smartphone integrated platform and a benchtop potentiostat (CH Instruments 750E) also referred to in this paper as CHI. For the amperometric mode, a signal current of 10 μA was generated by applying a voltage signal across a model of an electrochemical cell made from circuit components resembling a simplified version of Randles equivalent circuit model (R_{ct} = 200 kΩ, C_{dl} = 2 μF, and R_s = 1 kΩ). For the potentiometric mode, an input voltage of 0.5 V was applied directly from the sourcemeter across two electrodes. Finally, for EIS, the same circuit model was measured by both instruments to find the value of the charge transfer resistance. The results, shown in Figure 3.8, show the mean and standard deviation of the measurements normalized to the CHI data. While the variance in the data from the module is larger than that of the benchtop potentiostat (1.41 nA vs. 88.6 pA, 93.7 μV vs. 16.3 μV, and 0.630 Ω vs. 0.186 Ω), each is still within acceptable bounds for that particular technique and matches well with the CHI measurements.

These modes also consume varying amounts of power, due to the different ADC sampling and data transfer rates required by each mode. Also, since the module can disable the potentiostat, ADC, and DAC, as well as make the microcontroller sleep, essentially shutting itself off when not measuring (< 100 μW), the average runtimes of each technique also determine the overall energy

used by each mode. The entire potentiostat's peak power consumption including the switches and multiplexors is 9.6 mW. To conserve space, many of the parts used in the potentiostat contain more than one device in a single package making it difficult to power gate individual unused components, so the power consumption of the potentiostat remains approximately constant across different modes. The digital and mixed signal circuitry including the microcontroller, ADC, and DAC consume a maximum of 49.5 mW in amperometric mode with a runtime of 10 – 200 s and 46.2 mW in potentiometric mode for tests that last approximately 10 s. In EIS mode, this power consumption is 111 mW for an average of 130 s. To put these numbers into context, the lithium ion battery found in most of today's smartphones has a capacity of approximately 1500 mAh. Average idle time is ~50 hours (@ 108 mW), while talk time is ~10 hours (@ 540 mW). Hence, at the very worst, this module would about match the power consumption of the phone while idling and consume 80% less than a phone call. Therefore, making a couple of several minute-long measurements per day should not add noticeably to battery drain of the mobile device.

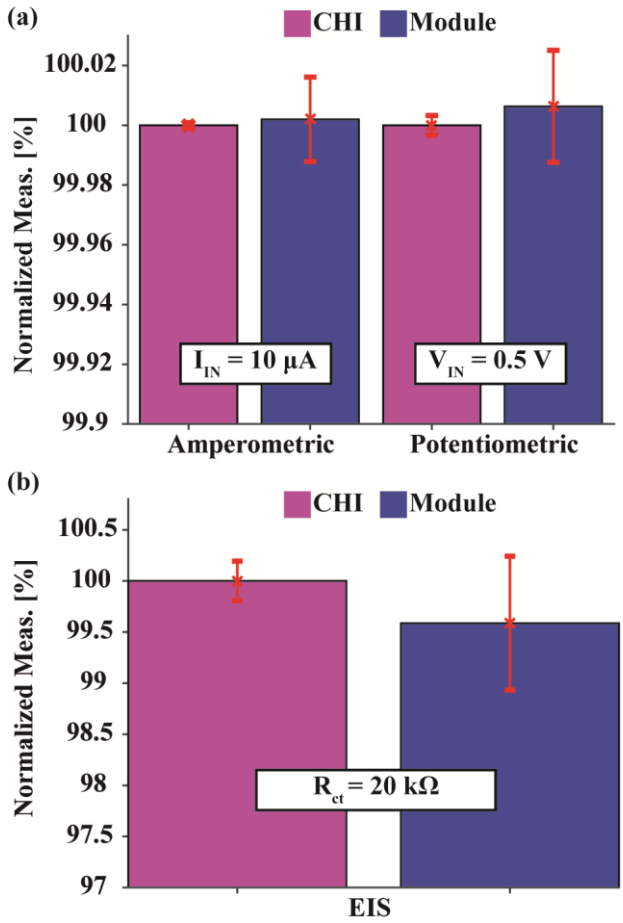

Figure 3.8. a) Plots of the amperometric, potentiometric and b) EIS mode repeated measurements for both the CHI and module potentiostat for N = 100 normalized to the CHI average.

3.6 Testing PoC Applications

While the device itself can perform many types of electrochemical tests, the biomarkers detected in the following assays were chosen due to their PoC applications. All these experiments, while some taking more effort and materials than others, do not require lab equipment to pre-process the samples and have been shown to be possible to measure at the PoC.

3.6.1 Amperometric Testing

3.6.1.1 Glucose

For Glucose experiments, PBS was spiked with various concentrations of Dextrose from Marcon (4912-12) to create the test solutions. Commercial glucose test strips (True Test Blood Glucose Strips) based on Glucose dehydrogenase-PQQ (GDH) were applied with the various test solutions (27-450 mg/dL) and measured with chronoamperometry (0.5 V step for 10 seconds) with both a benchtop instrument (CHI 750E) and the biosensor module. Since commercial glucose strips are optimized for small droplets of blood (a few microliters), 1 μL of each of the test solutions were used in these measurements. The results (Figure 3.9) show that the measured currents (taken after 10 seconds) for each concentration measured by both instruments follow the same trend. The calibration curve demonstrates that the assay is in the correct region to be able to diagnose or monitor diabetes (positive >200 mg/dL according to the American Diabetes Association).

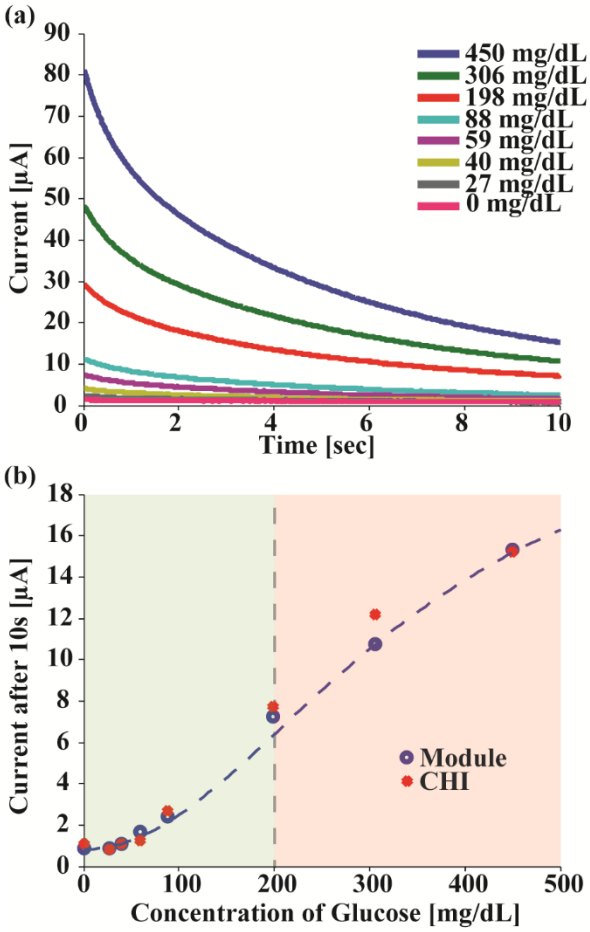

Figure 3.9. a) Chronoamperometry curves for glucose measured by the sensing module and b) calibration curves for both the biosensor and CHI with the positive and negative diagnosis ranges annotated.

3.6.1.2 Lactoferrin

Lactoferrin (LTF) is a common biomarker for infection found in various concentrations in bodily fluid such as sweat [64], saliva [65], urine [66], tears [67], and stool [68]. In this case, the detection of LTF in urine is used to diagnose urinary tract infection. Unlike the detection of glucose which is enzymatic, the detection method used here is a sandwich assay similar to ELISA.

Gold DropSens electrodes were functionalized for detection of LTF. Anti-human LTF (Abcam #ab10110) was mixed with Traut's reagent (Pierce 26101), dropped on the gold working

electrodes, and incubated overnight at -4°C. 2% BSA (Thermo Scientific 37525) was applied for 1 hour at room temperature to block the surface. Afterwards, various concentrations of LTF (Abcam #a78526) in 20 μL droplets were added to each electrode before adding the secondary antibody (Abcam #ab25811) and then the NeutrAvidin conjugated alkaline phosphatase (Thermo Scientific #31002). Each binding step lasted an hour and included washing in between. Finally, before running cyclic voltammetry on each electrode, the substrate, p-AminoPhenyl Phosphate (Santa Cruz Biotechnology sc-281392) was added and allowed to react for 10 minutes. The sweep range and scan rate were -0.2 V to 0.3 V and 25 mV/s, respectively.

The concentration of LTF in the urine of a patient with and without an UTI is 3,300 ± 646.3 ng/mL and 60.3 ± 14.9 ng/mL, respectively [66]. As shown in Figure 3.10, the limit of detection of this assay is approximately ~1 ng/mL. Hence, LTF can be detected by this device in the diagnostically relevant range. Furthermore, the average LTF concentration in various bodily fluids in healthy patients is annotated on the same plot, demonstrating that this device could also be used to measure physiological LTF concentrations in these other fluids.

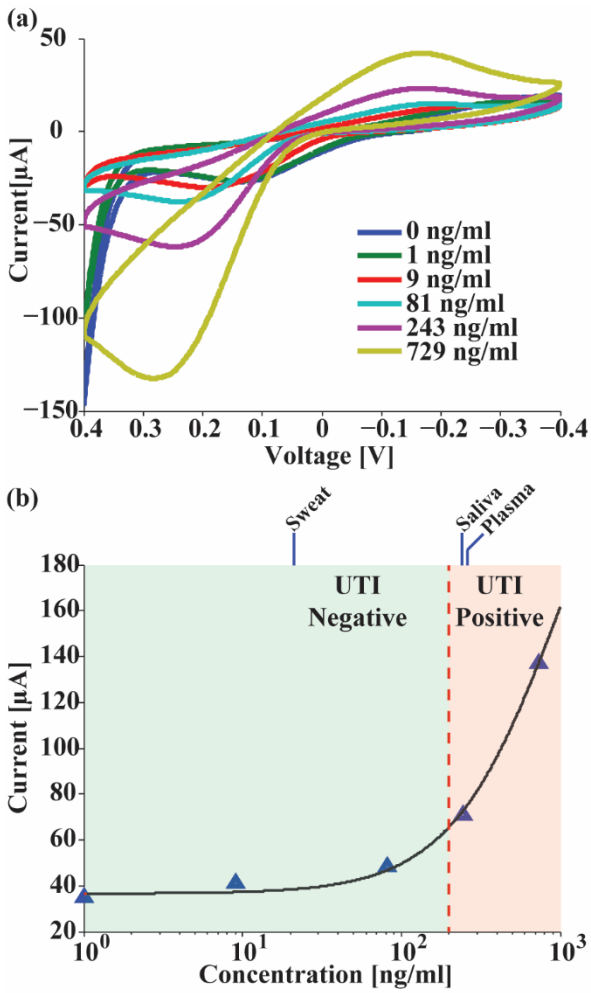

Figure 3.10. a) CV curves for LTF measured by the sensing module and b) calibration curves for the LTF assay with the positive and negative diagnosis ranges annotated.

3.6.2 pH measurements in Sweat

pH levels in sweat secreted from the skin have been shown to correlate with hydration levels in the body [38]. The higher the pH the more dehydrated someone is. Hence, by monitoring sweat during exercise, hydration can be tracked allowing the user to act accordingly to optimize his or her workout and avoid dangerous over exertion.

In order to first test the potentiostatic mode's accuracy when interfaced with a high impedance sensor, standard pH buffers from Thermo Scientific (910104, 910107, and 910110)

were used as well as separately prepared phosphate buffers adjusted to specific values ranging from pH 4-10. All measurements were taken with an Oakton pH Probe (EW-35811-74). These buffers were measured with the biosensor module in potentiometric mode and verified with a table top pH meter (Orion Star A211). The maximum deviation was found to be 1.2% or 0.08 pH between the two measurement methods.

Next, 75 µL of sweat was collected at 10-minute intervals from a volunteer running at a steady pace for an hour. Afterwards, the sweat was tested with the module using a small pH electrode (VersaFlex VNIS/LD). Each sample was also tested using standard pH test strips (pHydrion Vivid 67). As shown in Figure 3.11, the pH level increases steadily as more sweat is lost during the exercise as expected when compared to published data [38]. The test strips line up with the pH levels measured by the device and serve to confirm this trend as well.

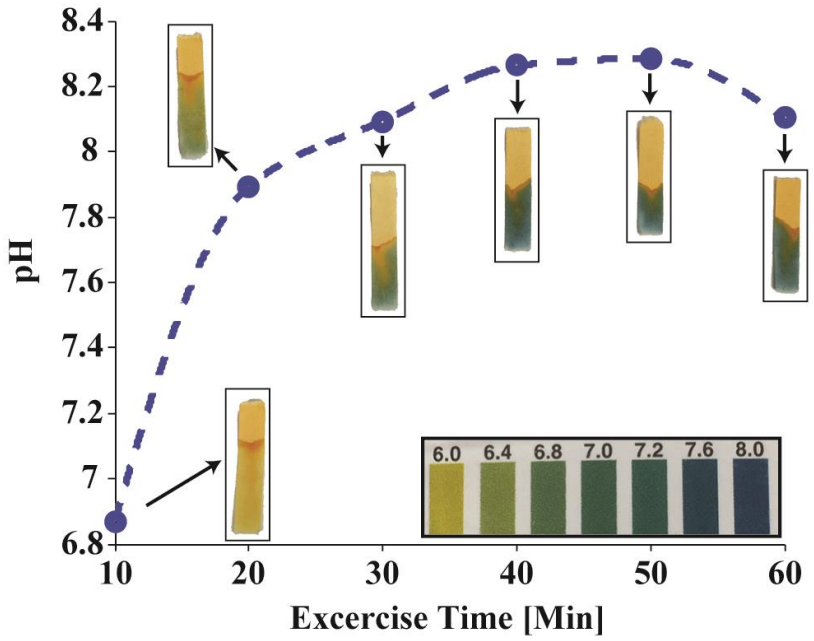

Figure 3.11. Plot of pH levels of sweat from subject during exercise and the pH test strip result for each sample.

3.6.3 Label-Free Assay

The sensing of certain biomarkers, such as ions (H+, Na+, etc.) and some metabolites (glucose, lactose, etc.) especially those with large physiological concentrations, can be easily designed for portable PoC use without an abundance of steps or reagents. However, assays for more complex molecules (peptides, proteins, DNA, etc.) that require much higher sensitivity to detect can be more cumbersome and time consuming for a user to conduct. For infrequent diagnostic tests, such as the labelled and highly sensitive UTI test discussed previously, the additional washing and reagent steps in the assay are manageable in the case of at-home testing. However, for more remote applications that require equally high sensitivity and increased portability, label-free techniques, such as EIS, are a promising solution as they do not use enzymatic labels to indirectly measure the biomarker, but rather physical and chemical changes, allowing for faster results with fewer assay steps [69,70]. To demonstrate our module's label-free capabilities, we conducted an assay for the detection of NeutrAvidin using biotin immobilized on the surface of a gold electrode. NeutrAvidin is version of avidin, a protein that forms a specific and high-affinity bond with biotin, a pair commonly used as a preliminary model for label-free detection assays.

Prior to the start of the assay, the electrode, 100 nm of gold sputtered onto a glass substrate, was cleaned with 1 mM KOH / H_2O_2 and functionalized with a 100 µM thiolated-biotin (Sigma-Aldrich #746622) reagent solution. After performing a washing and blocking, the electrode was ready for use. 20 µL droplets of different concentrations of NeutrAvidin (Thermo Scientific #31000) in a 1 mM ferro/ferri-cyanide ($K_4[Fe(CN)_6]$)/$K_3[Fe(CN)_6]$) PBS buffer were added to the electrode, allowed to bind for 10 minutes, and then measured using EIS (1 Hz – 10 kHz) with a Ag wire pseudo RE. These data were then fitted against the standard Randles circuit [49] to

determine the change in charge transfer resistance, relevant in faradaic impedance measurements. The Nyquist plot of the results as well as the concentration curve, shown in Figure 3.12, clearly demonstrate that this module can be used as a label-free biosensor. While NeutrAvidin itself is not a particularly useful biomarker, due to the mechanism of the biotin-avidin bonding, the results of this model assay demonstrate that this device can be generalized and used in most label-free affinity assays already developed [71–73].

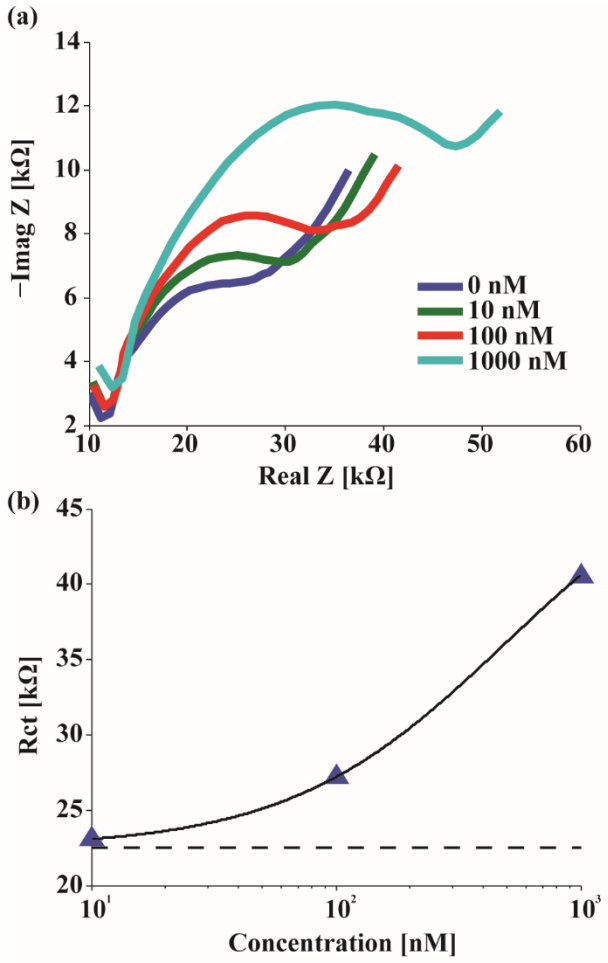

Figure 3.12. a) Nyquist plot of each serial dilution of NeutraAvidin b) Concentration curve after fitting data Randles circuit to find charge transfer resistance with baseline drawn below.

3.6.4 Comparison with Literature

These PoC applications experiments demonstrate both the performance and the extensive functionality of the reconfigurable module. To closely examine the performance, Table 3.1 shows a comparison with state of the art portable biosensors that have been previously published. For each mode, our module approximately matches the performance of other platforms in terms of dynamic range, sensitivity, and error, while at the same time being able to reconfigure itself into these three different sensing modes. Hence, whereas other devices only have one or two of these measurement capabilities, this device is able to package all these multiple techniques with approximately equivalent performance into a single small form factor module.

Table 3.1. Comparison with state-of-the-art for all electrochemical modes.

Ref.	**Amperometric**		**Potentiometric**		**EIS**		
	Dynamic Range	**Sensitivity [nA]**	**pH Resolution**	**Input [Ω]**	**Frequency [Hz]**	**Z Range [Ω]**	**Mag./Phase Error**
[36]	54 dB	100	-	-	-	-	-
[74]	43.5 dB	5000	-	-	-	-	-
[75]	51.1 dB	15	-	-	-	-	-
[22]	104 dB	0.5	8%	5 TΩ	-	-	-
[38]	-	-	0.2 pH	N/A	-	-	-
[76]	-	-	-	-	0.01 – 100k	1k-1T	5%, 3°
[77]	-	-	-	-	10 – 100k	N/A	12.3%, 12°
[47]	-	-	-	-	10 – 10k	1k – 10M	N/A, 0.8°
This Work	***106 dB***	***< 1 nA***	***1.2%, 0.08 pH***	***~5 TΩ***	***1 – 10k***	***50 – 10M***	***5%, 6°***

3.7 Conclusion

We have built and demonstrated a reconfigurable, multi-technique biosensor platform specially designed for integration directly into mobile devices for diagnosing and monitoring the health of a user at the PoC. By reusing components in different measurement modes, we can minimize the size and power of the design while at the same time keeping performance and expanding the functionality of the module for use in most PoC applications. By adding this dedicated hardware directly into every day carry electronics, we hope to promote the use of

specialized, portable, and practical medical devices well positioned to be the first line of defense in the future of healthcare.

Chapter 3, in full, is a reprint of the material as it appears in IEEE Transactions on Biomedical Circuits and Systems 2016. Alexander C. Sun, A. G. Venkatesh, and Drew A. Hall, "*A Multi-Technique Reconfigurable Electrochemical Biosensor: Enabling Personal Health Monitoring in Mobile Devices*," IEEE Transactions on Biomedical Circuits and Systems, vol. 10, no. 5, pp. 945–954, 2016. The dissertation author was the first author of this paper.

Chapter 4

A Scalable High-Density Electrochemical Biosensor Array for Parallelized Point-of-Care Diagnostics

4.1 Introduction

Currently, several biomedical sensing applications would benefit from high-density biosensor arrays (e.g., proteomics, genomics, and peptide arrays), which consist of tens of thousands of individually addressable miniature sensors packed tightly together on a single substrate. This high number of sensors offers a feasible method to conduct many assays simultaneously, while the dense packing of sensors greatly reduces the reagent cost and sample size requirement.

In proteomics, arrays are currently being used for drug discovery and biomarker selection, where a target analyte (protein or antigen) is applied to an array functionalized with thousands of different peptide variations in order to characterize the analyte through mapping its binding affinity to a wide range of peptides. High density arrays are suitable for this application due to the

enormous number peptides that can be used to map the analyte, since, unlike DNA which has 4-base pairs, peptides are created from a library of 20-amino acids. In neuroengineering, high density electrochemical arrays can be used to spatially map the release of neurotransmitters in the brain with high resolution, potentially down to individual neurons. Finally, immunosignaturing, a novel and promising diagnostic technique currently under development, uses high density arrays to map a patient's immune response profile (antibodies found in a blood sample) to detect disease, rather than directly detecting the antigen itself [78]. Unlike directed tests, this technique allows for early diagnosis and is disease agnostic since prior knowledge or hypothesis of what the disease could be is not needed.

Most of these applications, however, use optical detection methods with a fluorescent enzyme label. This transduction technique requires a high-resolution imager, which tends to be too bulky and impractical for point-of-care (PoC) devices meant to handle measurements in remote areas outside of centralized laboratories. To solve this problem, in this paper, we describe the design and validation of a portable and aggressively scalable high-density array biosensor (Figure 4.1) that uses electrochemical detection instead of optical, enabling powerful, yet cost-effective point-of-care diagnostic tools.

Electrochemical detection is often used in order to improve the size, cost, and scalability of PoC biosensors. As seen in the past decade, there have been many novel developments in miniaturization of electrochemical biosensors thereby allowing the sensing surface to be fabricated directly on top of the integrated readout circuitry [79–82]. However, these implementations require a full potentiostat with a very sensitive transimpedance amplifier (TIA) or current conveyor to measure the signal from the sensors.

The proposed design aims to significantly reduce the complexity and size of the circuitry by leveraging a little studied electrochemical detection method known as coulostatic discharge. The transduced signal from this technique is a transient voltage, instead of a current, thereby greatly decreasing the area and power consumption of the readout circuity for each sensor. Hence, this technique coupled with electrochemical amplification from interdigitated electrodes (IDEs) and efficient utilization of the inherent double layer capacitance allows one to pack all the sensors and circuitry densely enough for these high-density array applications.

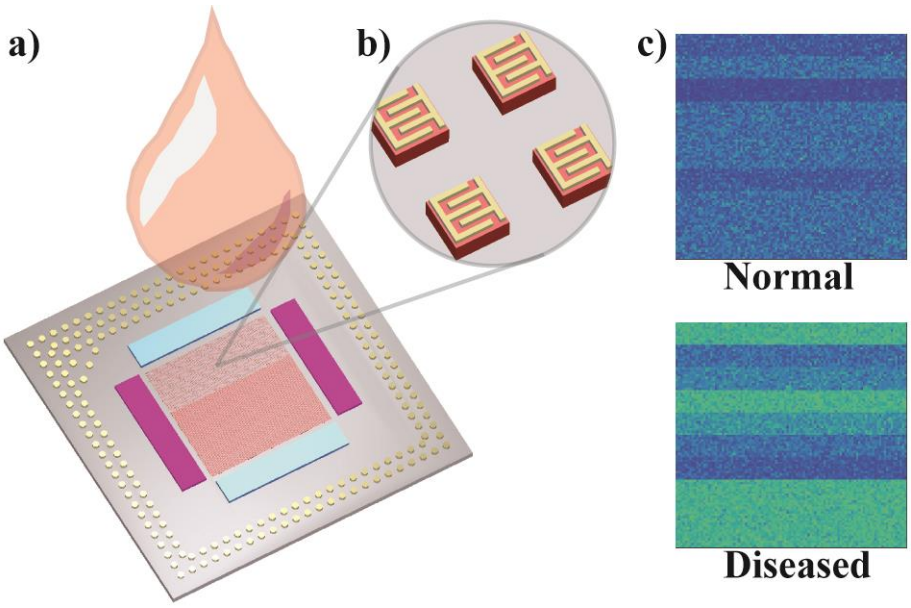

Figure 4.1. a) Drawing of the proposed high-density biosensor array chip, b) interdigitated electrodes with circuitry for c) tens of thousands of diagnostic tests on a single sample.

4.2 Electrochemical Detection Method

4.2.1 Mult-Biomarker Assay

While some applications do not require sensor functionalization, such as in neurotransmitter detection, many do operate as affinity assays by functionalizing the surface of the sensor with detection molecules that capture a target antigen. Typically the assay is conducted as

in Figure 4.2 where an enzymatic label is used that produces a redox active molecule when an antigen has been captured that is then transduced by the electrodes. Due to the goal of miniaturization and high number of sensors, both spotting and *in-situ* peptide printing are being explored as the current functionalization method, the latter having shown promise in previous optical peptide microarrays [78,83].

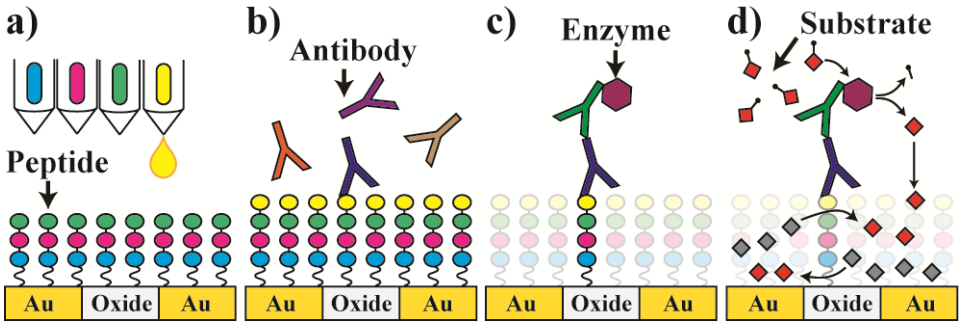

Figure 4.2. Steps for proposed sandwich assay: a) Detection peptides are printed on the surface, b) analyte solution is applied, c) the secondary antibody with the enzyme is introduced, d) and a substrate is added and reacts with the enzyme to produce a redox active pair of molecules generating an electrical signal.

4.2.2 Coulostatic Discharge Technique Theory

The coulostatic discharge technique was first described independently by Delahay and Reinmuth as an electrochemical method to study fast electrode processes, and, while not widely studied, has been verified as a highly sensitive biosensing technique [84–86]. As seen in Fig.3a, instead of applying a continuous potential signal to an electrochemical sensor and measuring the generated current response, as is the case with often used amperometric techniques, a potential is applied only briefly in the coulostatic discharge method, enough to allow a build-up of charge to form at the interface between the electrode and the ionic solution, often referred to as the double layer capacitance. The source supplying the potential to the electrode is then disconnected. The

discharging of the double layer capacitance, along with any other capacitance at this measurement node, decreases the voltage of the electrode at a rate that is related to the concentration and reactivity of the redox probe present. The simple fact that this method outputs a fairly large voltage signal (~hundreds of millivolts) over time rather than a small current signal that can fall to femtoampere levels typical of microelectrodes, makes the readout circuitry much simpler, entirely obviating the need for a full potentiostat.

To enhance the magnitude of this signal from these microelectrodes, an electrochemical amplification method known as redox cycling is used. With a reversible redox pair (two molecules that oxidize and reduce back into each other) and closely spaced interdigitated electrodes biased at the reduction and oxidation potentials respectively, the redox molecules shuttle electrons between the electrodes producing an amplified signal as shown in Figure 4.3b.

To explain the relationship between the concentration of the redox species and the discharge rate, the electrochemical process that generates the current between IDEs can be derived as follows. Equation (4.1) describes the relationship between the voltage *E(t)* on one of the IDEs and corresponding current *I(t)* generated at the electrode [86,87]**:**

$$E(t) = E^0 + \frac{RT}{nF} \ln\left(\frac{I(t)}{I^{lim} + I(t)}\right) \tag{4.1}$$

where E^0 is the standard potential of the redox pair, *R* is gas constant, *T* is temperature, *n* is the number of electrons transferred in each in each redox event, *F* is Faraday's constant, and I^{lim} is the steady state current before the disconnection occurs. I^{lim} is linearly dependent on the initial concentration of the redox molecule and, hence, is the signal that we are trying to measure. The discharging of the double layer capacitance can be written as:

$$I(t) = -C_{dl} \frac{dE(t)}{dt} \tag{4.2}$$

where C_{dl} is the double-layer capacitance created by the formation of layers of ions on the surface of the electrode. An extra calibration constant was added to the resultant differential equation in order to set the equilibrium potential equal to the potential of WE2. Unlike in previous work, where an external capacitor is added to the voltage measurement node, only the capacitor inherent to the electrochemical sensor, which is the double-layer capacitance, and parasitic capacitance are used here [10]. By not adding an extra capacitor for each sensor, a significant amount of area is conserved, especially when considering an integrated solution. However, this double-layer capacitor does have a slight dependence on bias voltage. By running electrochemical impedance spectroscopy with our own fabricated electrode array chip, discussed in a following section, and sweeping the bias voltage, it is revealed that this capacitance (1-2 nF) does not vary significantly in the 0-0.3 V range.

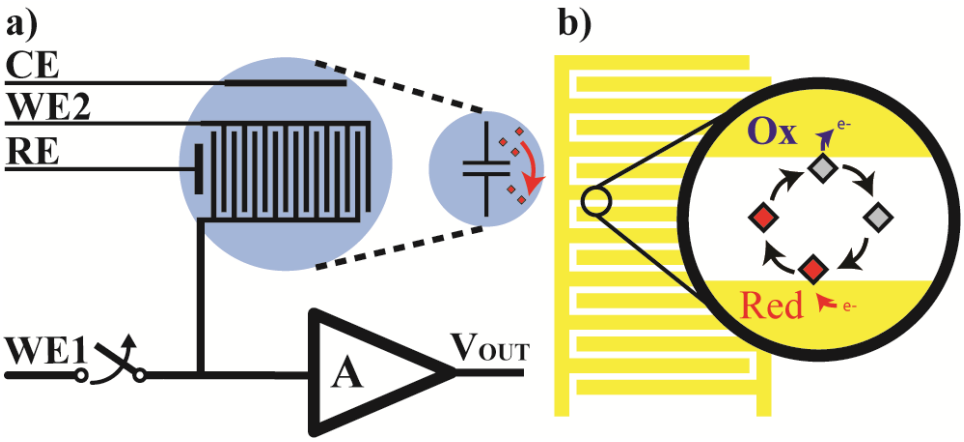

Figure 4.3. a) Simple circuit diagram for Coulostatic Discharge and b) redox cycling with IDEs.

4.2.3 Simulation

Solving Equation (4.1) and (4.2) results in a differential equation relating the voltage and equilibrium current. We solved the resultant differential equation using the “ode45” function in MATLAB. This allowed us to simulate predicted IDE potential discharge curves over time. The

simulation parameters can then be scaled to predict the discharge curves of IDEs in a high-density array. If coupled with a diffusion analysis of the redox molecules, we can maximize SNR of the discharge curves by optimizing sensor placement and geometry.

4.3 Design of Test Platform

As a proof of concept to gather experimental data that can be extrapolated for future larger designs, we have designed and built a custom multichannel bi-potentiostat that is capable of running most common electrochemical techniques, in addition to the discharge technique. This design is implemented with discrete components on a printed circuit board (PCB) and interfaces with a custom fabricated 4×4 microelectrode array.

4.3.1 Coulostatic Discharge Bi-Potentiostat

The design, as shown in Figure 4.4, consists of a feedback loop used to set the solution potential, a transimpedance amplifier on each side of the electrode, and an ultra-low input bias (60 fA max) buffer used to measure the discharge voltage with a bandwidth of 10 kHz. This implementation can measure voltages between ±100 μV to ±1.8 V (~90 dB dynamic range), which is the relevant range for most electrochemical techniques, and the potentiostat can source up to 30 mA to the cell. The circuit operates in the following fashion: 1) Initially, the switch is closed and the sensor is charged up to V_{WE2}-V_{WE1}. 2) After the electrochemical sensor is charged up, the switch is opened and the voltage at the output of the low-leakage buffer, V_{DIS}, is monitored. This architecture was chosen because the charging currents and discharging current of WE2 can be recorded, which is useful for debugging, but can be implemented in a much more straightforward fashion once the system is well understood. Since discrete electronic switches tend to have

unacceptable leakage currents in the (~100 pA), we opted to use a mechanical relay instead. While this is impossible to do in standard CMOS, once the move is made to the integrated circuit version, we will have much more control over adjusting the switch leakage and can use various methods to reduce this unwanted current. Using a Keithley Source Meter, the leakage at this node ($I_{Leakage}$ in Figure 4.4) was measured to be lower than 100 fA at a 1 V bias, limited only by the measurement equipment. All other measurements were gathered with a National Instruments data acquisition card and MATLAB script.

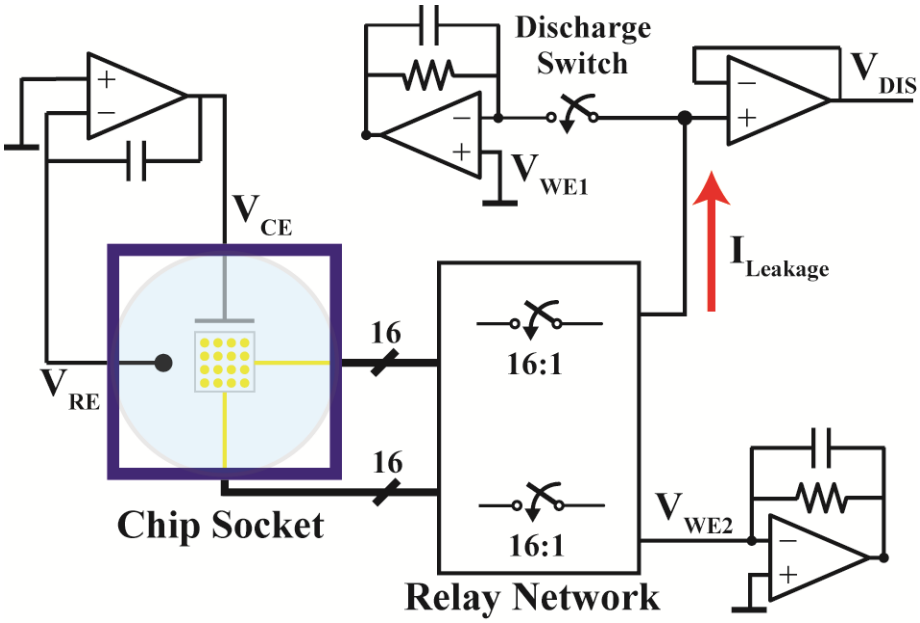

Figure 4.4. Test platform schematic with socket that holds array test chips.

4.3.2 16-Channel Low-Leakage Multiplexor

For the same reasoning as the discharge switch, multiple relays were used to implement the multiplexor that attaches each of the 16 pairs of electrodes to the discharge measurement circuitry. Hence, the entire array can be automatically iterated through running different tests on the same solution. The 4×4 test chip directly connects to the PCB via a custom designed socket

and solution can be directly pipetted onto the surface of the sensor through a hole in the PCB (Figure 4.5c).

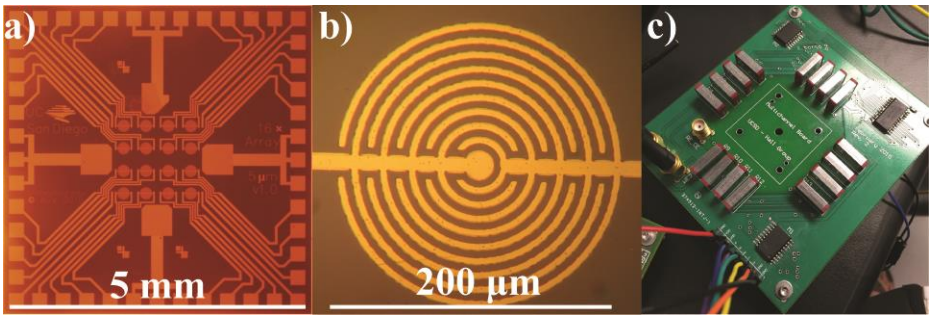

Figure 4.5. a) Microscope image of the 4×4 electrode array, b) image of a single sensor, and c) PCB which houses the low leakage multiplexor network.

4.4 Redox Molecule Characterization Tests

4.4.1 Materials and Procedures

In order to use the test platform to demonstrate coulostatic discharge for an array of sensors, 4×4 electrode arrays were fabricated. Each sensor is 200 µm in diameter with 5 µm spacing between the electrodes. The sensor was patterned using electron beam lithography and etched using Argon ion milling on a silicon wafer sputtered with 100 nm gold using Chromium for the adhesion layer. The sensors were then connected to contact pads by sputtering 150 nm gold to a patterned photoresist and lifted-off. The counter electrode was fabricated by lift-off after sputtering 200 nm platinum on a patterned photoresist. Finally, a 250 nm silicon dioxide passivation layer was deposited on top of the chip to prevent unwanted interaction of contact lines with the bulk solution during electrochemical experiments. An external silver wire electrode was dipped into the well surrounding the chip to function as a pseudo-reference electrode. While the voltage of such an electrode is more dependent on the composition of the test solution, it is still able to maintain a constant potential and does not require chlorination thereby making future on-chip reference

electrodes simpler to fabricate. A solution consisting of an equal mixture of potassium ferro/ferri-cyanide ($K_4[Fe(CN)_6]$) /($K_3[Fe(CN)_6]$) from Spectrum (P1286, P1296) in a phosphate buffer solution (PBS) in different dilutions was used to measure discharge curves and verify the functionality of the sensor array. 20 μL of each dilution was pipetted directly on top of the sensor array mounted on the test platform and then coulostatic discharge measurements were taken for each of the 16 electrode pairs. The hold time (before opening the switch) and the release time (after opening) were 2 and 8 seconds, respectively. WE1 and WE2 were biased at the reduction and oxidation potential of the redox molecule to promote redox cycling, which for this test was 0.2 V and 0.1 V, respectively.

4.4.2 Results

The complete response for each sensor for the different concentrations of the redox molecule is shown in Figure 4.6. Each 4×4 box represents the sensor chip at a different concentration and shows good uniformity of the signal response between the different electrodes. Figure 4.7a also shows that the measured discharge curves from a single sensor match well with the simulated curves for different concentrations. However, the measured data appears to have a slightly faster discharge rate than the simulated data. This discrepancy is most likely from leakage currents at the interface between the chip and PCB board that is discharging the buffer solution. More investigation will be done in the future to determine the exact origin and minimize this effect. A calibration curve (Figure 4.7b) is generated from the extracted initial slope (t = 40 ms) of both the simulated and measured data. As expected from Eq.1-2, the higher the concentration the steeper this slope and both the simulated and average measured values match well.

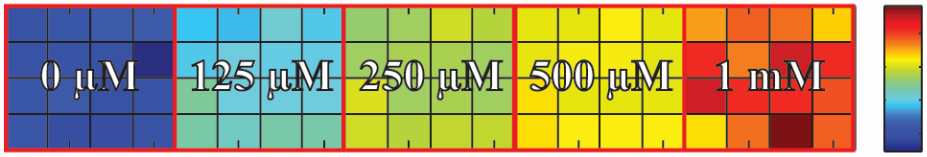

Figure 4.6. Heat map of measured data from the entire 16-sensor array with different redox molecule concentrations applied.

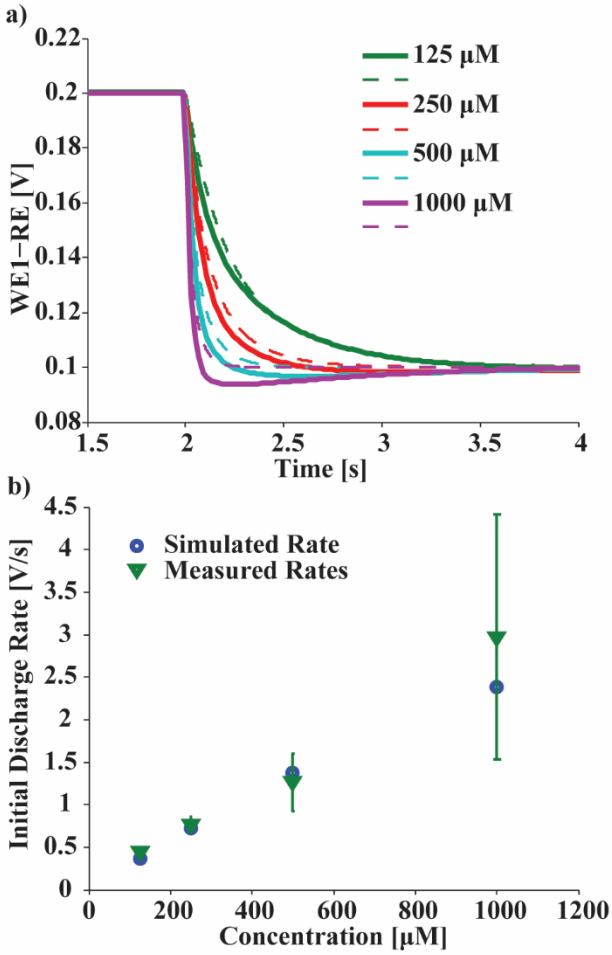

Figure 4.7. a) Measured (solid lines) and simulated (dashed lines) discharge curves for various concentrations of ferro/ferri-cyanide for a single electrode. b) Averaged discharge rates.

4.5 Conclusions

With this test platform and sensor chips, we have demonstrated a small scale version of a proposed design for minimizing size and complexity of high density sensor arrays. With this

preliminary data, along with further larger scale simulations, we hope to achieve an integrated solution with sensors implanted directly on top achieving roughly >10,000 active sensing areas on a 5×5 mm chip.

Chapter 4, in full, is a reprint of the material as it appears in IEEE Biomedical Circuits and Systems Conference 2015. Alexander C Sun, Anthony Au, A. G. Venkatesh, Vikash Gilja, and Drew A. Hall, "*A scalable high-density electrochemical biosensor array for parallelized point-of-care diagnostics*," in 2015 IEEE Biomedical Circuits and Systems Conference (BioCAS), 2015, pp. 1–4. The dissertation author was the first author of this paper.

Chapter 5

High-Density Redox Amplified Coulostatic Discharge-Based Biosensor Array

5.1 Introduction

Numerous biomedical applications rely on high-density biosensor arrays, which consist of thousands of individually addressable miniature sensors on a single substrate. One interesting application is the simultaneous detection of a wide range of humoral antibodies either for checking the immune system for the presence of antibodies created in the body post-vaccination, i.e., vaccination screening, or scanning the complete antibody profile for signs of illness as is the case in immunosignaturing (IMS) [88–90]. For the former, a single device capable of measuring multiple analytes would make rapid and comprehensive verification of immunization possible. For the latter, rather than directly sensing the disease antigen(s), IMS measures the immune system's response to the disease, i.e., the patient's antibody profile, which is amplified rapidly by white blood cells to several orders of magnitude higher concentration than the antigen itself. This shift

in focus towards monitoring a set of antibodies not only leads to accurate and early diagnosis, but also allows for the tracking of disease progression [91]. For example, the antibody profile of an individual infected with rhinovirus for the first time is vastly different than the profile during all subsequent infections of the same virus. This occurs because during the initial infection the body has yet to determine the appropriate antibody to target the virus, for which it produces a wide variety of combinations.

To enable these technologies, instead of running several targeted tests for all the possible antibodies, which would require impractical amounts of time, reagents, and biological samples, a single unguided assay can be run. As illustrated in Figure 5.1(a), this single assay can be performed by using an array of densely packed sensors, which are functionalized to detect a large set of antibodies in an individual.

Current high-density array technologies use optical detection (i.e., fluorescent dyes attached to the analyte) thus requiring complex microarray imaging equipment that is too bulky and impractical for point-of-care (PoC) applications where measurements are made in remote areas away from the resources of centralized labs. While electrochemical detection is known to improve the size and scalability of biosensors [9], most implementations still require a potentiostat with an extremely sensitive transimpedance amplifier (TIA) to measure the minute signals associated with microelectrodes, and such designs typically only scale to a ~100×100 μm^2 pixel area [92–105]. For higher-density implementations, many potentiostat-based arrays either have specially-fabricated sensors to increase sensitivity (i.e., amplify the signal) [96,106–108] or implement parts of the measurement circuitry outside of the array to decrease the pixel size [94,95]. Nonetheless, neither approach addresses the fundamental difficulty of measuring small currents with decreased sensor size.

In this paper, extended from [109], the design and validation of an integrated high-density biosensor array for vaccination screening, that also enables PoC IMS, is presented. It leverages an alternative and little-used electrochemical detection method, coulostatic discharge [84,85,109–111], to significantly reduce the complexity and size of the readout circuitry. Figure 5.1(a) shows an illustration of the array functionalized with different capture proteins to simultaneously detect multiple disease biomarkers. Each biopixel transduces capture events into an electrical signal, $I_{sig}(t)$, whose magnitude is related to the biomarker concentration. Unlike chronoamperometry, where this current is measured directly, the current is used to discharge the sensor's innate double layer capacitance (Figure 5.1b), translating the measurement to changes in $v_{out}(t)$. This technique effectively transforms a miniature current measurement to a much simpler voltage-over-time measurement. As the sensor's intrinsic capacitance is on the order of tens of pF and $I_{sig}(t)$ is ~1 pA/µM, the discharge rate of $v_{out}(t)$ is on the order of 1 V/s/µM, which greatly relaxes and simplifies the readout circuitry requirements. Hence, this technique along with electrochemical amplification from interdigitated electrodes (IDEs) allows for all the sensors and circuitry to be packed densely enough for high-density array applications using only the features available in a standard CMOS processes.

The remainder of the paper is organized as follows: Section II describes the coulostatic discharge sensing principle, and Section III discusses the design of the biopixel circuitry. Sections IV and V present characterization and biological measurement results, respectively. Comparisons are made in Section VI, and conclusions are drawn in Section VII.

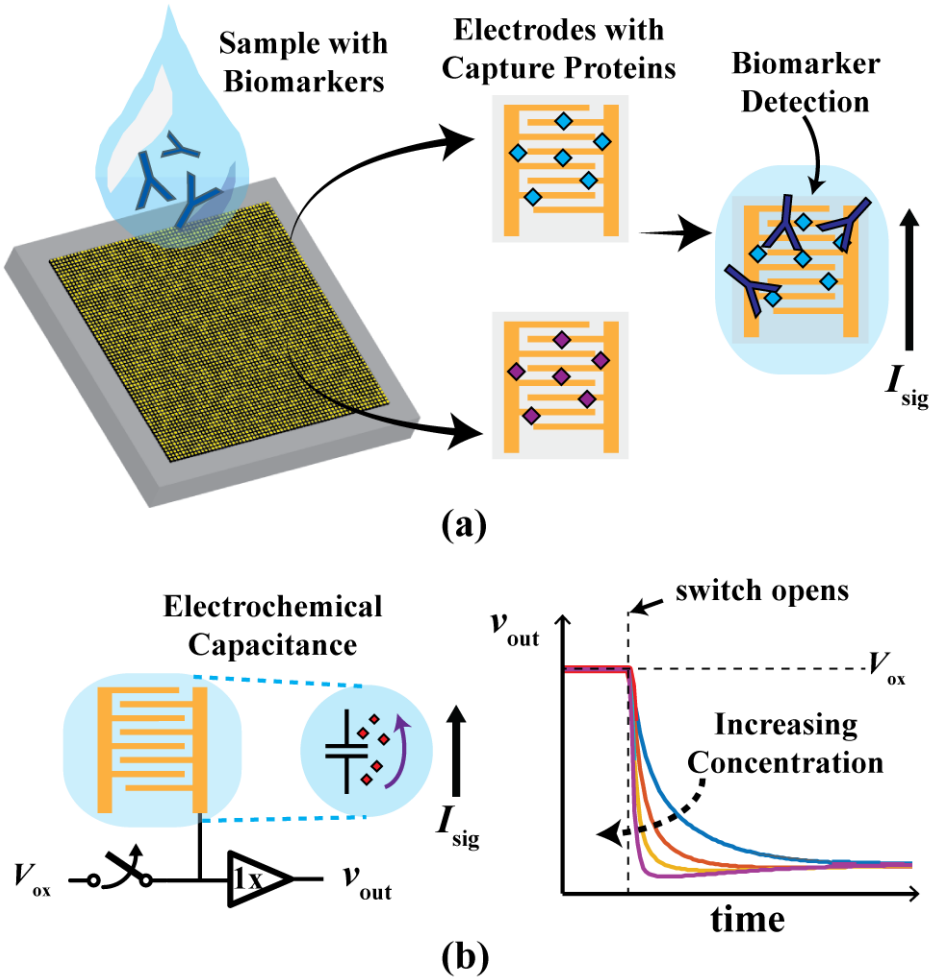

Figure 5.1. (a) Illustration of a high-density array of electrodes functionalized with multiple capture probes for detecting biomarkers. (b) Coulostatic discharge readout technique used to convert a current into a voltage using the inherent electrochemical capacitance of the sensor.

5.2 Sensing Principle

Coulostatic discharge is an electrochemical technique developed independently by both Reinmuth and Delahay in 1962 that uses the inherent double-layer capacitance between an electrode and an electrolytic solution to convert the signal current to a voltage that changes slowly over time [84,85]. Specifically, the measurement is performed by charging up this capacitance to a particular voltage and then letting it discharge through the electrochemical cell. To use this method for biomarker detection, the surface of the electrodes must be coated with capture

molecules that give the sensor specificity (i.e., the ability to distinguish a specific molecule from others).

The assay steps used in this work are as follows: 1) Each biopixel is functionalized by immobilizing capture proteins on the gold-plated sensor using a standard method of dropcasting an excess amount of proteins to saturate the surface completely. The sensor's surface is known as the working electrode (WE), which is where the biochemical detection occurs that is subsequently transduced into an electrical signal (Figure 5.2a-*i*). A single sensor contains two WEs separated by an insulating material (e.g., oxide in an IC). Each type of capture protein binds to a specific target antibody due to the binding affinity of the antibody-antigen complex. 2) The biological sample is added to the sensors and incubated so that any antibody biomarkers present in the sample bind to their specific capture protein (Figure 5.2a-*ii*). After washing to remove any unbound molecules, a secondary antibody that binds to the bound antibodies is added to the array, effectively sandwiching the biomarkers (Figure 5.2a-*iii*). This secondary antibody is conjugated with an enzyme, alkaline phosphatase (ALP), that reacts with a p-aminophenyl phosphate (pAPP) substrate, thus generating a by-product redox molecule, p-aminphenyl (pAP), that is detected by the biopixel (Figure 5.2a-*iv*). Detection occurs when pAP approaches a WE biased at a specific voltage, known as the oxidation potential, and reacts to form quinonimine (QI) by transferring electrons to the WE. QI, in turn, reacts at the second working electrode biased at the reduction potential converting back into pAP by receiving electrons. Thus, this shuttling of electrons creates a current proportional to the concentration of the biomarker in the sample. An important distinction to make here is that actual full-scale IMS relies on *in-situ* printing a large number of randomly-generated peptides onto the array sensors [89,112–114]. To use this array for IMS technology, peptides would be used in place of proteins to detect the antibody profile [115]. The underlying

sensing mechanism is the same for both cases, so successful operation of the protein-based assay implies that the array can be used for IMS.

The resulting signal would typically be measured directly using standard amperometric techniques and current-based readout circuitry (e.g., as is done in a glucometer). However, in coulostatic discharge, a potential is applied to the electrode only briefly allowing a build-up of charge on the sensor's intrinsic capacitance, C_{dl}. This capacitance, known as double layer capacitance, is formed from the layers of ions and charged molecules that assemble at the interface between the electrode and ionic solution, and exists between the electrode and the bulk solution (Figure 5.2b). After the source supplying the potential to the electrode is disconnected, C_{dl} is discharged through the electrochemical cell by the current generated due to the redox reactions, thus slowly decreasing the voltage of the electrode at a rate related to the biomarker concentration.

As implied by Figure 5.2(b), near the beginning of the discharge phase the sensor behaves as an *RC* circuit, where the capacitance is C_{dl} and the resistance is determined by the initial redox current, which is related to the concentration of the redox molecules. Hence, the discharge rate can be written as

$$\frac{dv_{\mathrm{out}}(t)}{dt} = \frac{I_{\mathrm{sig}}(t)}{C_{\mathrm{dl}}}, \tag{5.1}$$

where $I_{\mathrm{sig}}(t)$ is the current generated after opening the switch. In practice, the discharge curve is nonlinear due to the voltage dependence of both $I_{\mathrm{sig}}(t)$ and C_{dl}. As described by the Nernst-Planck equation [49], $I_{\mathrm{sig}}(t)$ depends on the concentration gradient of the redox molecules around the electrode:

$$I_{\mathrm{sig}}(t) = \frac{nFAD_{\mathrm{o}}C_{\mathrm{ox}}(t)}{\delta}, \tag{5.2}$$

where n is the number of electrons transferred per reaction, F is the Faraday constant, A is the area of the electrode, D_{o} is the diffusion coefficient of the redox molecule, $C_{\mathrm{ox}}(t)$ is the

concentration of the redox molecule at the electrode surface, and δ is the width of the diffusion layer, which, for microelectrodes, is simply the distance between electrode fingers. Also, the Nernst equation links the voltage of an electrode, i.e., WE1 in Figure 5.2, to the concentration of redox molecules at its surface as follows

$$V_{\mathrm{WE}}(t) = E_0 + \frac{RT}{nF}\ln\left(\frac{C_{\mathrm{ox}}(t)}{C_{\mathrm{ox,lim}} - C_{\mathrm{ox}}(t)}\right), \tag{5.3}$$

where E_0 is the standard potential of the redox species, R is the universal gas constant, T is the absolute temperature, and $C_{\mathrm{ox,lim}}$ is the total concentration of the oxidant and reductant at the electrode surface [86]. Furthermore, the capacitance C_{dl} is also a function of the electrode voltage. Specifically, C_{dl} is given by

$$C_{\mathrm{dl}}(t) = \frac{\varepsilon_0\varepsilon_{\mathrm{r}}}{\lambda_{\mathrm{D}}}\cosh\left(\frac{qV_{\mathrm{WE}}}{2kT}\right), \tag{5.4}$$

where $\varepsilon_0\varepsilon_{\mathrm{r}}$ is the dielectric constant, λ_{D} is the Debye length, which is a measure of how far the electric field extends into the solution, kT/q is the thermal voltage, and V_{WE} is the potential of the electrode [49]. Note that the presence of C_{dl}, which is on the order of 10 pF - 1 nF, obviates the need for an explicit capacitor in each biopixel. This capacitance is also at least one order of magnitude larger than the capacitance formed by the metal electrodes alone, so it dominates the sensor capacitance.

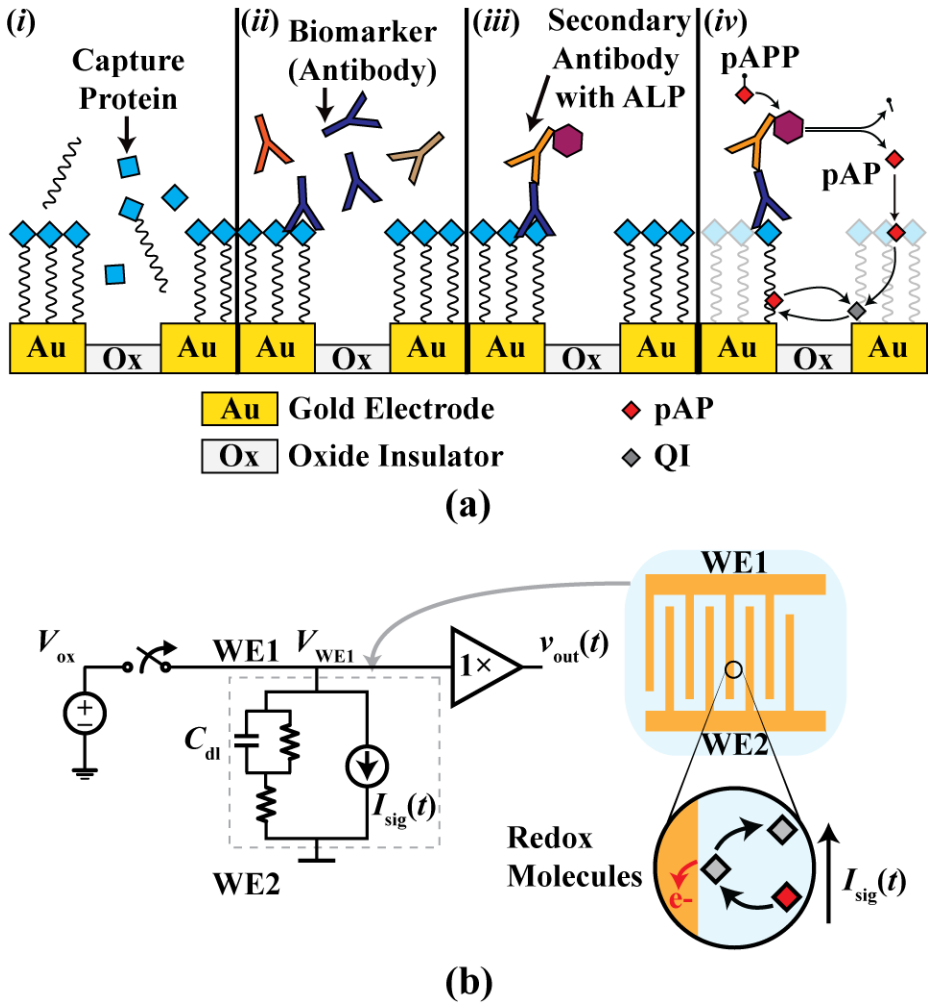

Figure 5.2. (a) Steps of the antibody detection assay and (b) coulostatic discharge measurement circuit with equivalent sensor model.

Figure 5.3(a) shows simulated discharge curves obtained using (2)-(4) and known redox coefficients. Due to the nonlinear nature of these curves, the optimum range at which to sample the voltage signal is not obvious. To examine the tradeoffs of different sampling times, a noise model of the biopixel including the buffer and sensor's equivalent noise contributions, $i_{b,n}(t)$ and $i_{e,n}(t)$, is shown in Figure 5.3(b), where the noise only affects the measurement after the switch is open. As the measurements are taken by subtracting two samples of the buffer's output taken at different times (i.e., right after the switch opens and after a certain amount of time), thus

implementing correlated double sampling [116], the buffer in this model is connected only to the sensor. Also, charge injection is cancelled by measuring this difference.

As described above, $I_{sig}(t)$ integrates onto C_{dl}, thus creating the characteristic discharge curves illustrated in Figure 5.3(a). The sensor's impedance is modelled as C_{dl} in parallel with the charge transfer resistance, $R_{ct,}$ which is a measure of how readily the sensor surface reacts with the redox molecules. It follows from Figure 5.3(b) and the previous discussion that the voltage noise power can be computed as

$$\sigma(\tau)^2 = \int_{1/\tau}^{\infty} \left| \frac{R_{ct}}{1+j2\pi f C_{dl} R_{ct}} \right|^2 \left(S_{e,n}(f) + S_{b,n}(f) \right) df, \tag{5.5}$$

where τ is the time at which the buffer output is measured, $S_{e,n}(f)$ and $S_{b,n}(f)$ are the one-sided power spectral densities (PSDs) of the noise current signals of the sensor and buffer, respectively, and C_{dl} is assumed to be constant. The noise contributed by the sensor is highly dependent on several biological and chemical factors. Measurement results show that this noise source, which can be modeled as having a white component and a $1/f$ component, is considerably more dominant than the noise contributed by the buffer, so the buffer design in this system is practically constrained only by the biopixel area.

As shown in Figure 5.3(c), for large values of τ the signal component in $v_{out}(\tau)$ increases, but the noise variance also increases due to both the white and $1/f$ components of $S_{e,n}(f)$. In contrast, for small values of τ the signal component in $v_{out}(\tau)$ decreases, but the $1/f$ noise barely affects the measurement. Therefore, a range of suitable sampling times as well as an optimal point that maximizes the signal-to-noise ratio (SNR) can be found. Using estimated values for R_{ct} and C_{dl}, as well as measured noise PSDs for the buffer and sensor, the noise variance for different values of τ between 10 ms and 100 s was computed. The computed SNR for a 100 nM

concentration for different scenarios is shown in Figure 5.3(d). As it can be seen from the figure, the SNR is maximized at $\tau \cong 1.2$ s.

Figure 5.3(e) shows that the same trend exists across various concentrations. Depending on the desired resolution, concentration range, and targeted measurement speed, the sampling time, τ, can be reduced. For instance, in applications such as IMS, where coarse or even binary detection is sufficient, a smaller sampling time can be chosen to decrease the time required to scan an entire array. Also, by relating the noise level back to current using C_{dl} and the sampling time, a current of ~600 fA is expected at $\tau \cong 1$ s, so the switch should have a leakage smaller than this value.

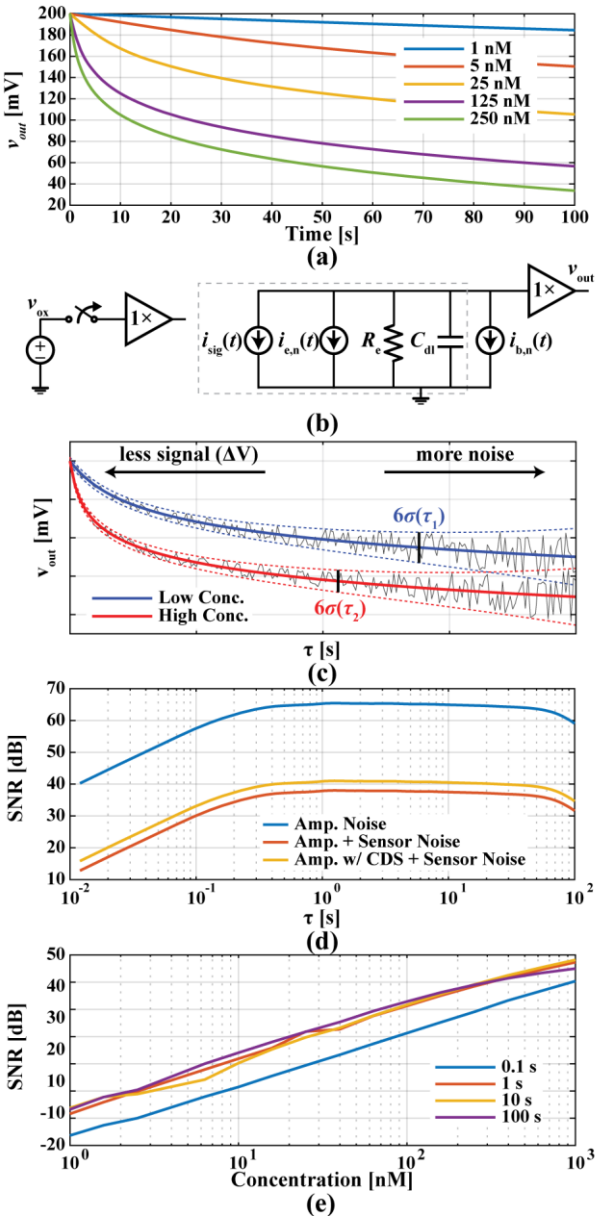

Figure 5.3. (a) Simulated discharge curves, (b) noise circuit model of pixel, (c) illustration of sampling time tradeoffs, (d) SNR at different sampling times with various noise sources included at a concentration of 100 nM, and (e) SNR in a range of concentrations at various τ.

5.3 System Design

5.3.1 Architecture

Figure 5.4 shows a block diagram of the implemented biosensor array, where V_{WE1} and V_{WE2} are the input voltages applied to the working electrodes WE_1 and WE_2, respectively, v_1, v_2,

…, v_{64} are the array outputs, and the readout circuit below each biopixel comprises a unity-gain buffer and a low-leakage switch controlled by the digital signals r and r_e. As each v_i output is shared among the 64 pixels from its respective column, a 6-bit decoder with outputs d_1, d_2, …, d_{64} is used to select the row of the array whose buffer outputs are connected to the array outputs. Given that all the buffers in a column are connected to the same output, the higher the biopixel is in the array, the longer the routing to the output pad is, so the signal sees a different delay to the output depending on the position of the biopixel. However, due to the slow-varying nature of the coulostatic discharge technique, these delays negligibly affect the measurements and are accounted for in the settling time. Nonetheless, in larger arrays, where the number of biopixels might force the use of smaller sampling times, this issue might need to be addressed. In such cases, this problem could be circumvented by dividing the array into subsections with separate outputs, so that the biopixel-to-output-pad paths are more uniform across the array.

The working electrode WE_2 is shared by all the pixels within the array, and it is always connected to V_{WE2}. In contrast, each biopixel has its own WE_1, and V_{WE1} is applied to this electrode only when the low-leakage switch is closed. Not shown in the figure are the counter electrode, implemented as a wide gold-plated strip across the center of the array, and the reference electrode, an external Ag/AgCl wire. Together, these electrodes, controlled by off-chip circuitry for flexibility, set the potential of the solution and provide a common reference voltage for the WEs.

A bias current is generated by a constant-g_m reference located at the corner of the array and an off-chip resistor. This current is copied to 16 current mirrors at the top of the array, and each distributes this current down the columns to 16 local bias-voltage generators along the length of the chip. Each one of these bias-voltage generators (256 in total), biases the buffers of a 4×4 quadrant of biopixels to reduce area overhead.

To assess the performance of the low-leakage switch, test pixels were implemented on the right side of the array with a dedicated output, v_{test}. Each one of such pixels is almost identical to an array's biopixel, but instead of having an IDE connected to the input of its buffer, it has a MIM capacitor of 100 fF, 1 pF or 10 pF size with its other terminal connected to ground. Instead of a low-leakage switch, some of these test pixels have a standard switch consisting of a PMOS transistor with its body tied to the supply voltage.

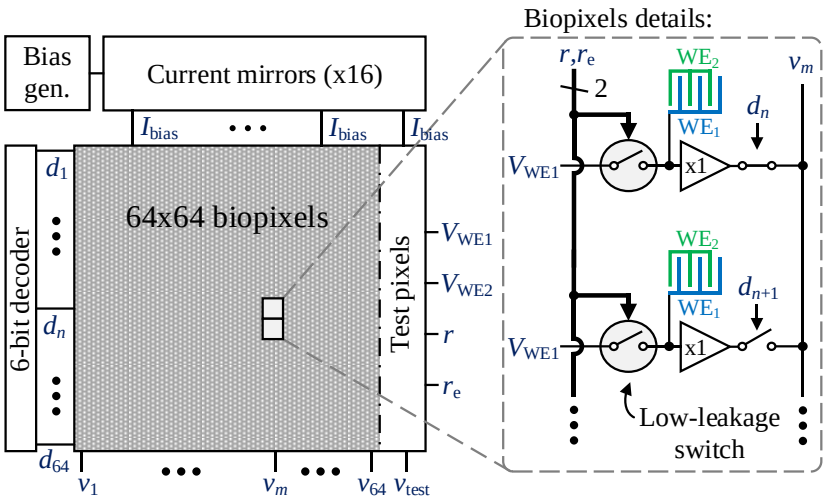

Figure 5.4. Simplified block diagram of the chip.

5.3.2 Sensor Design

Since IMS arrays of 330,000 pixels have been shown to be able to diagnosis multiple illnesses reliably, the eventual target number of sensors for a future full-sized electrochemical IMS array is on the order of 100,000. Therefore, assuming the array is fabricated using the full reticle size and that 10% is used for control and output circuitry overhead, the maximum size for each pixel would be ~100×100 μm^2. Specifically, an area of 42×42 μm^2 per sensor would allow for an

array of exactly 330,000 pixels. Guided by this analysis, the electrode geometries were designed using similar pixel areas and constrained by the minimum width and spacing rules of the process.

The microelectrode sensors were fabricated using the top metal layer. Each biopixel consists of two interdigitated electrodes designed to amplify the signal using an electrochemical amplification technique known as redox cycling. Redox cycling is the effect when a reversible redox pair repeatedly diffuses between two electrodes biased at different potentials, one at the reduction potential and the other at the oxidation potential of the pair, transferring electrons through redox reactions at the two electrodes. Hence, a single redox molecule can contribute multiple times to the overall current. The redox current signal, I_{rc}, obtainable from a planar IDE is given by the following empirical equation:

$$I_{\mathrm{rc}} = \alpha \left(0.64 \log\left(2.6\left(1 + \frac{W}{G}\right)\right) - 0.19\frac{G}{W+G}\right)^2, \tag{5.6}$$

where W and G are the finger width and the gap between fingers, respectively, and

$$\alpha = nNFD_{\mathrm{o}}C_{\mathrm{dl}}b, \tag{5.7}$$

where N is the number of fingers and b is length of the fingers [117–120]. It follows from (6) that for a given area, a smaller gap width and a larger number of fingers provide higher amplification. As shown in Figure 5.5, four different electrode designs were fabricated. Electrodes A.1 and A.2 have finger and gap widths of 5 µm and 5 µm, whereas electrodes B.1 and B.2 have finger and gap widths of 2 µm and 3 µm. In a standard phosphate buffered saline (PBS) buffer solution, the C_{dl} of these designs range from 24 to 180 pF. According to (6), the amplification factors of A.1, A.2, B.1 and B.2 are 2.25×, 5.27×, 4.93×, and 9.41×, respectively. Given that (6) is strictly applicable to two-dimensional IDE geometries, the estimated amplification factors are expected to underestimate the measured values.

Often, physical channels, trenches, and walls are fabricated directly on top of or around the sensor to increase the cycling efficiency, which is a measure of a sensor's ability to keep the same redox molecules shuttling between the two electrodes without them diffusing away from the sensing area [106,107,117]. While these structures are all effective in increasing the amplification, they require complex and customized post-processing steps, thus making the fabrication more time consuming and expensive. To avoid these additional complex post-processing steps while still increasing the signal amplification, an alternative approach that is CMOS foundry compatible was taken. Specifically, the passivation layer directly above each sensor was removed to create 3D structures. By waiving design rule check errors meant to protect the bottom layers of the chip from over etching (the top metal is often used as an etch stop), structures that take advantage of the height of the electrodes were created. Given that the passivation was opened across the entire IDE, the etchant can carve down the gaps between the fingers. As shown in Figure 5.6(a), this allows for the formation of 3D trenches between the two electrodes that increase the collection efficiency by trapping the redox molecules and further amplifying the signal. Moreover, as seen in Figure 5.6(b), due to the existence of walls left over by the removal of passivation between pixels, effective nanowells were created that isolate the sensors and contain the redox active molecules generated during the assay.

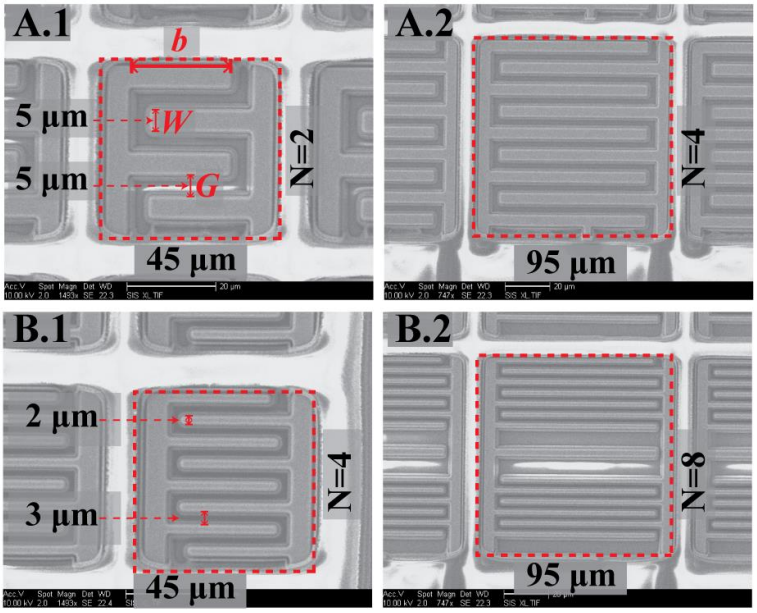

Figure 5.5. SEM images of the different IDE designs. Both the A and B designs (left and right) have the same finger width and spacing.

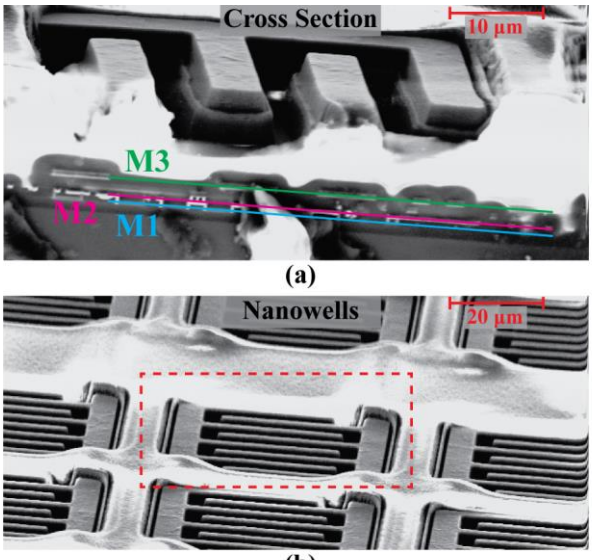

Figure 5.6. SEM images of (a) chip cross section showing trenches between fingers and (b) nanowells surrounding each pixel.

5.3.3 Biopixel Circuitry

The details of the readout circuit beneath each biopixel are shown in Figure 5.7(a). It consists of a low-leakage switch and a unity-gain buffer. To save circuit area, the buffer is used

both to read out the voltage of the electrode, $v_{n,m}$, and to assist the operation of the switch by driving the body of the right-most PMOS transistor when the switch is open. PMOS devices were chosen for the switch to allow for the low-leakage design to be used in any standard CMOS process where individual control of the NMOS body is not possible. The entire circuitry fits underneath the 45×45 μm^2 sensor using only three metal layers for routing and one metal layer for the electrodes.

The buffer is implemented as a differential amplifier with a cascoded tail transistor. It has 42.8 dB gain and a 26 kHz unity gain bandwidth product. Due to both the switch being PMOS and the voltages used to control the WEs, the input devices of the buffer were required to be NMOS. To minimize the $1/f$ noise contribution of the buffer, these transistors were made as large as possible given the limited area available.

The low-leakage switch is driven by the digital signals reset, r, and reset-early, r_e. It comprises of four PMOS transistors with their bodies tied to V_{DD}, illustrated as switches in Figure 5.7(a), and a body-driven PMOS transistor, M_1 [106,121]. To minimize the leakage current through M_1 when the working electrode WE1 is discharging, both the node labeled as x and the body of M_1 are connected to the buffer output, so ideally the PN junctions of M_1 see no voltage drop and thus have no leakage current.

The low-leakage switch operation is illustrated in Figure 5.7(b). Three phases of operation are distinguished: (*i*) reset phase 1, (*ii*) reset phase 2, and (*iii*) release phase. During (*i*), M_1 is on and the node labeled as y is charged to V_{WE1}. During (*ii*), M_1 is still on, but its body connection is switched from V_{DD} to the buffer output. This is done before M_1 is turned off to avoid any charge injection from M_1's channel to node y. Then, during (*iii*), M_1 is turned off and node y starts discharging through the electrodes. Given that both the body of M_1 and node x are being driven by the buffer during this phase, the voltage difference between the source, drain, and body terminals

of M_1 are ideally zero, so that the leakage current is minimized. In practice, the buffer's offset voltage causes a small voltage drop across the body of M_1 and node y, but simulation and measurement results suggest that this is not a problem in practice. For the assay measurement tests, the frequency of the reset signals is set to 1 Hz with r_e leading r by 1 µs. When measuring the output of the buffer during the release phase, the first and final points are measured at 1 µs and τ after the switch opens.

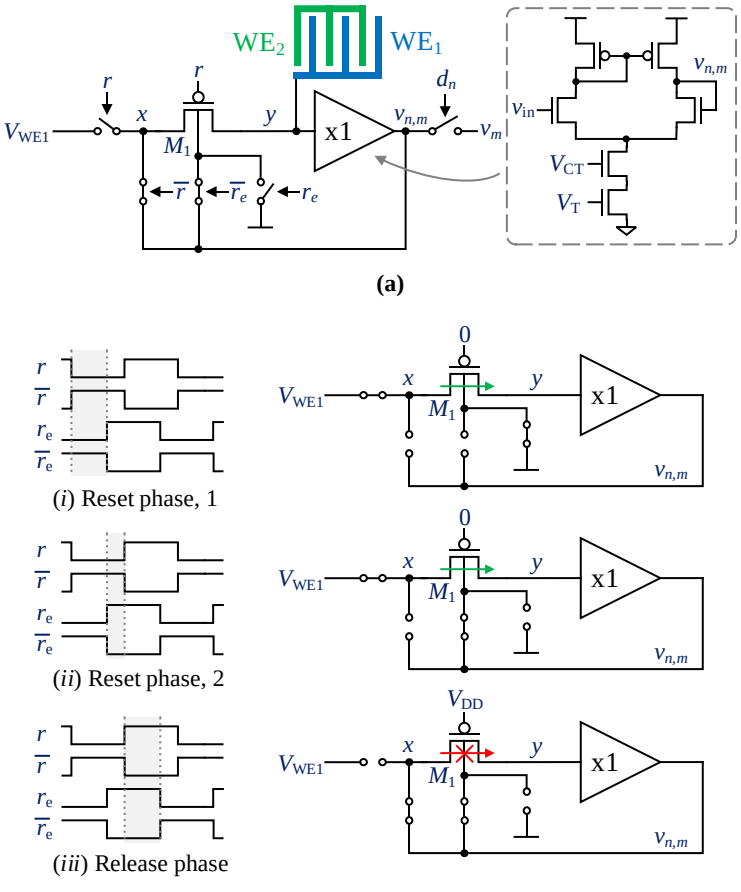

Figure 5.7. (a) Biopixel readout circuit. (b) Ultra-low-leakage switch operation. The frequency of the reset signals is 1 Hz with reset early leading by 1 µs.

5.4 Characterization Measurements

A 5×5 mm^2 chip (Figure 5.8) was fabricated in a 1P4M 180 nm CMOS SOI process. The array contains 64×64 biopixels split into four quadrants, each with a different IDE design. Each unit biopixel is only 45×45 µm^2.

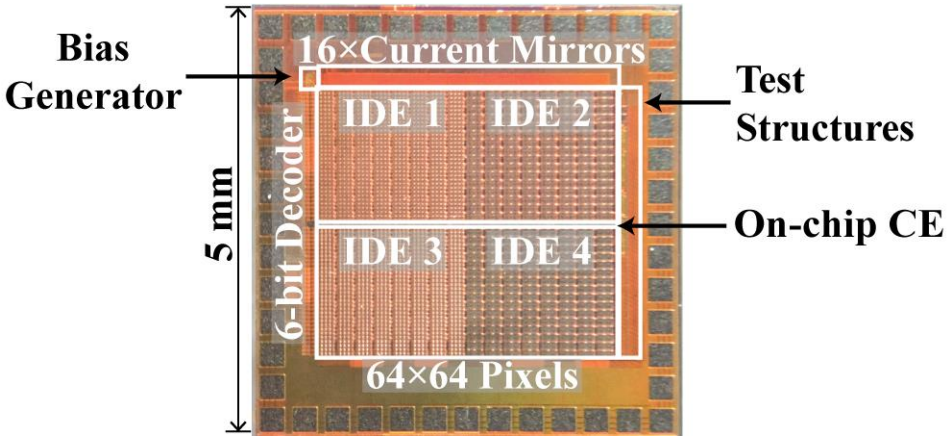

Figure 5.8. Chip photograph.

5.4.1 Electrical Characterization

The entire chip consumes a maximum of 95 mW (23 µW per biopixel) from a 2.5 V supply. The offset of the buffer averaged across the entire array was measured to be 1.78 ± 0.16 mV. The input-referred total integrated noise of the buffer is 33 μV_{rms} (100 kHz bandwidth) with a 1/*f* noise corner of 120 Hz.

To assess the performance of the low-leakage switch, discharge tests were run using the test pixels. There are two different types of test pixels: one with a standard PMOS switch and the other, which is identical to the one used in the array, with a body-driven switch (Figure 5.9a). Separate pixels of each type are attached to known MIM capacitors in place of the top metal electrodes. For each of these tests, up to 0.5 V was placed across the two working electrodes. Just as in a normal discharge test, the switch opens and charge begins to leak from the capacitor into the switch causing the voltage measured to decrease over time. The slope of the measured voltage

over time and the known capacitance size was then used to calculate the leakage current the test sensor experiences. The body-driven switch leakage was measured to be 13 aA, which is less than that of the standard PMOS switch with the body tied to V_{DD}, which was 195 aA (Figure 5.9b). The body-driven switch had better performance across the entire voltage range.

The results suggest that a standard switch could be used instead of a low-leakage switch in this application. This is the case because the array was designed in an SOI process. However, the biopixel topology is meant to be used in different processes, where standard switches might not perform as well. For instance, in a standard 180 nm process, according to simulations, the leakage current of a typical PMOS switch is ~1.3 pA, whereas that of the low-leakage switch is ~4 fA.

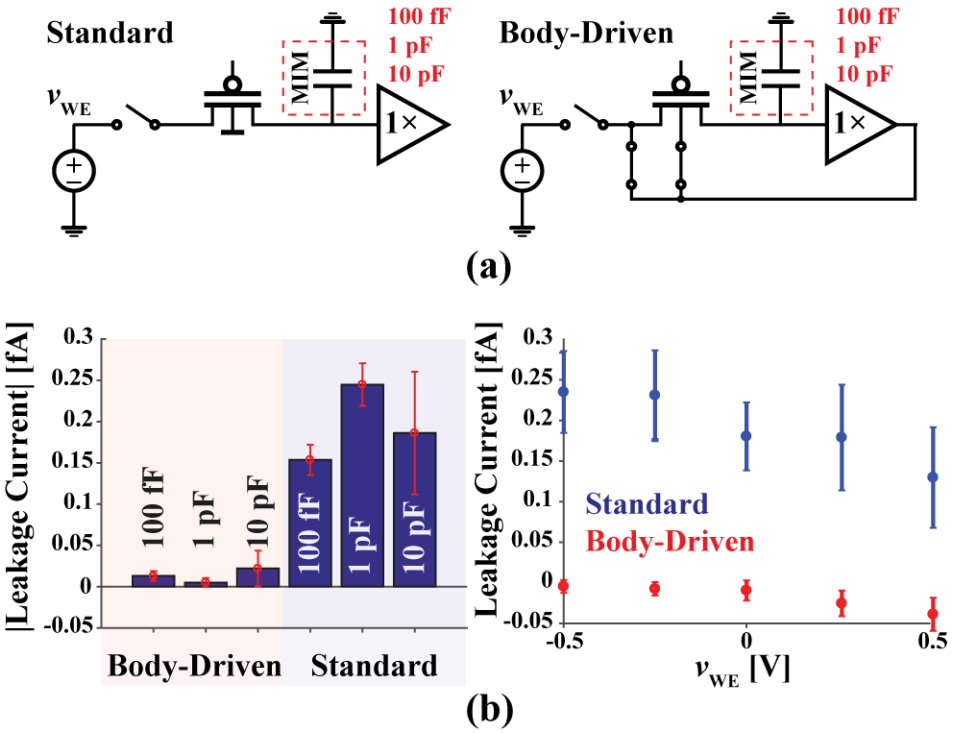

Figure 5.9. (a) Test pixel schematics. (b) Average leakage measurement results from the test structures with 0.5 V applied across each (left) and the average leakage of all the test structures at different sensor voltages (n = 3).

5.4.2 Sensor Preparation

For electrochemical compatibility, an electroless nickel immersion gold (ENIG) plating process (MICRO, Stapleton Technologies Inc.) was used to plate the exposed top metal aluminum electrodes [93,98,122,123]. After a thorough cleaning of the surface with acid, akaline, and deoxygenation cleaners, the entire chip was put through a double zincate process to prepare the exposed aluminum electrodes for the subsequent electroless nickel and gold plating steps. The SEM images of each sensor after plating are shown in Figure 5.10(a). Typically, as with most on-chip electrochemical sensors, it is desirable to maximize the thickness of both the nickel and gold layers in order to achieve reliable adhesion and uniform coverage. The combined thickness of these layers is usually around 3 μm. Since the electrodes in this work are interdigitated instead of a single pad of metal, the spacings and features of the IDEs are small enough that the plating can create unwanted shorts between the two working electrodes. Furthermore, even collections of small metal particles left over from the plating process can cause individual IDEs to have much lower resistances. Hence, different plating times of both the nickel and gold steps were experimented with and evaluated by measuring the resistance between the two halves of the IDE (Figure 5.10b). A total plating time of ~5 minutes was found to be optimal due to its high resistance while still maintaining a robust and even coverage of gold across the array.

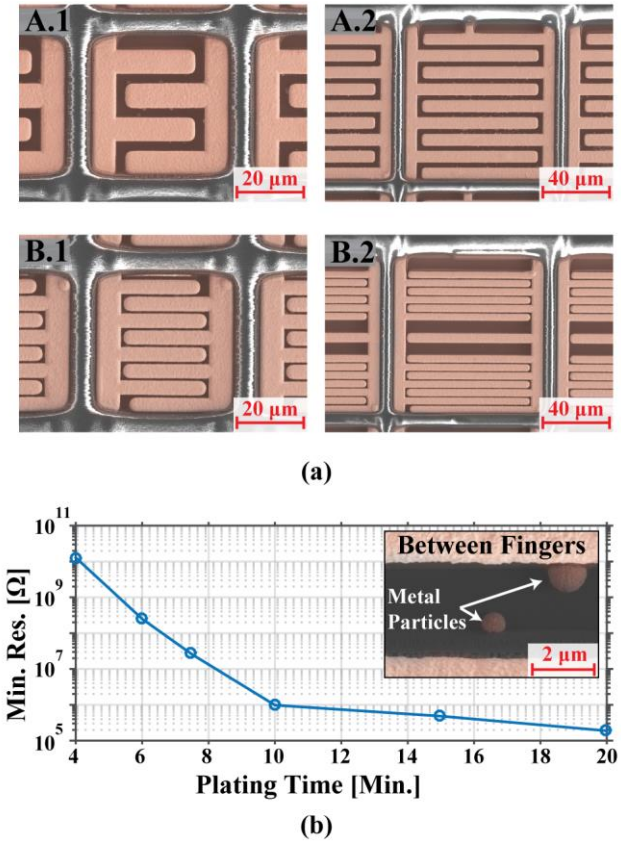

Figure 5.10. (a) SEM images of each sensor after gold plating colored to show texture. (b) Minimum resistance measured between the working electrodes with different gold plating times. Inset shows metal particles that can provide a low resistance path if plated for an extended period.

5.4.3 Electrochemical Characterization

To evaluate the performance of the sensors as well as the gold plating, a chip with bare gold electrodes was used to measure the redox molecule Ferro/Ferricyanide as a proxy for the actual assay. After cleaning the chip by sonicating in isopropyl alcohol, the chip was mounted in a socket designed to create a ~10 µL well over the sensors. External Ag/AgCl and Pt electrodes were dipped into this well to form the reference and counter electrodes. Next, coulostatic discharge was run using the in-pixel circuitry to measure the sensors in various concentrations of Ferri/Ferricyanide in both single working electrode, as seen in Figure 5.11(a), and dual working electrode modes to compare the same sensor with and without redox cycling. In single electrode mode, both sides of the IDE are shorted together, instead of biased independently, effectively

making them into a single electrode with combined area where no redox cycling can occur. In dual electrode mode, the IDE operates as intended with one electrode biased at 200 mV and the other at 0 mV relative to V_{CM}, allowing for the shuttling of the redox molecules. Using these measurements, the amplification factor was determined by calculating the ratio of the signals between the dual and single electrode modes. As shown in Figure 5.11(b), the average amplification factors for each design are 5.33 ± 1.2×, 8.1 ± 1.5×, 6.06 ± 2.1×, and 10.5 ± 2.1×, respectively. These values are slightly larger than the theoretical values due to the 3D trench and nanowell structures. IDEs with the same gap and finger widths but greater number of fingers have higher amplification. Smaller gap size also increases the redox cycling, as expected. Furthermore, the large variation in amplification can be explained as either a result of un-even plating of gold in the trenches or variability in the formation of the trenches themselves. The latter seems more likely since the plating procedure is widely used while the etching between fingers is unconventional and not guaranteed by the foundry.

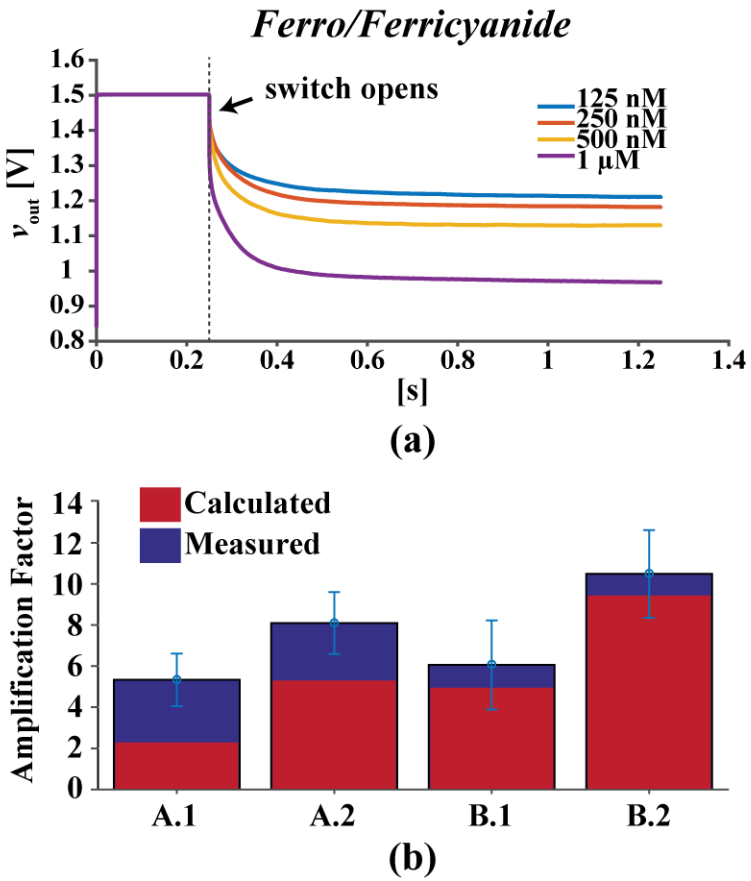

Figure 5.11. (a) Discharge measurements of combined working electrodes with various concentrations of Ferro/Ferricyanide. (b) Calculated and measured (n = 60) amplification factor using coulostatic discharge.

5.5 Biological Measurement Results

For the biological tests, only a portion of the array that has the same electrode design, A.2, was used to allow for a fair comparison between tests. To demonstrate a bioassay, 2 µg (66 pmol) of Rubella virus capsid protein (ab74574, Abcam) in PBS was dropcast on the surface of the gold sensor array using 20 µg of Traut's Reagent (26101, ThermoFischer Pierce) and blocked with 1% bovine serum albumin (37525, ThermoFischer Scientific). Mouse anti-Rubella antibodies (ab34749, Abcam) were subsequently added and incubated for one hour. For the secondary antibody, 1 µg of rabbit anti-mouse secondary antibodies linked with ALP (ab6729, Abcam) was used. Lastly, 6 mM pAPP substrate (sc-281392, Santa Cruz Biotechnology) in a 0.1 M glycine

buffer pH 8.4 was added and allowed to incubate for ten minutes. The ALP enzyme reacts with the pAPP substrate producing AP, an electrochemically active molecule that shuttles electrons between the two fingers of the sensor. Fig.12(a) shows measurement results for both CV, measured with a 25 mV/s scan rate from -0.2 V to 0.3 V for 3 cycles, and coulostatic discharge. Both successfully detect the presence of anti-Rubella antibodies. The experiment was then repeated for anti-Rubella spiked into human serum (HS-20, Omega Scientific, Inc.). Figure 5.12(b) shows the average discharge rates for serum with and without the antibody.

Next, a multi-biomarker assay meant to simultaneously detect both anti-Rubella and anti-Mumps (ab9880, Abcam) antibodies was performed using the array. The same portion of the array used for the previous Rubella-only test was split into two, with each part functionalized with either Rubella or Mumps protein (ab74560, Abcam). Four different chips were used for this experiment, all functionalized exactly as described above. Each chip was given a different test sample of serum spiked with 1.3 µM Rubella antibodies, 2.3 µM Mumps antibodies, both, or neither. As seen in Figure 5.12(c), the parts of the array that are exposed to their corresponding antibody show a higher slope than those that are not. Although there exists a large chip-to-chip variation, likely due to disparity in functionalization or test conditions between the different chips, the array can still distinguish between each of these different samples to detect the presence of either biomarker, thereby demonstrating its capability to monitor vaccinations.

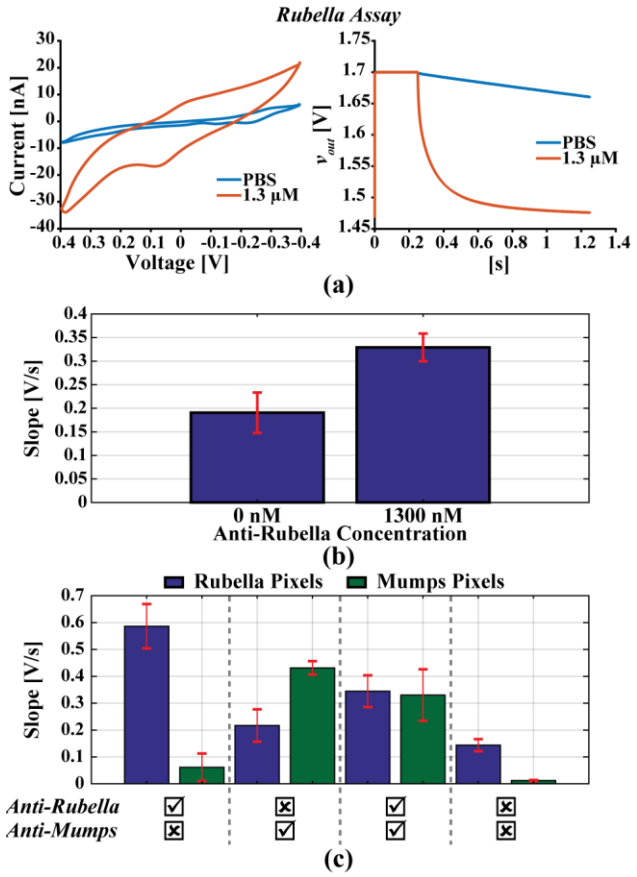

Figure 5.12. (a) CV and discharge curves for a single electrode compared with a control. (b) Average discharge rate for positive and negative detection of anti-Rubella antibody (n = 30). (c) Discharge rates for multi-antibody detection of both anti-Rubella and anti-Mumps antibodies (n = 8).

5.6 Comparison

Table 5.1 compares this work to other integrated electrochemical biosensor arrays, and Figure 5.13 plots their pixel areas and number of devices per pixel with different markers to signify those that have special post-processing and/or have measurement circuitry external to the array. Due to redox cycling, this work achieves a relatively small pixel area and high sensor density (400 pixels/mm^2) without any complex post-processing, which others need to increase sensitivity. While augmenting sensors with additional structures and materials is effective, it requires complex fabrication steps that are much more difficult and expensive to produce and scale than an array built purely with a standard CMOS process. To the best of our knowledge, this work is the highest

density amperometric biosensor array that does not require additional post-processing steps. Furthermore, coulostatic discharge greatly decreases the number of devices required in the measurement circuitry (~12) allowing for all the circuit to reside completely within the area of a pixel. In fact, the two arrays based on coulostatic discharge have the lowest number of devices that fit completely within a pixel. Hence, rather than occupying a considerable amount of area with circuit blocks external to the array, this work makes efficient use of the chip area as illustrated by the total density calculation in Table 5.1.

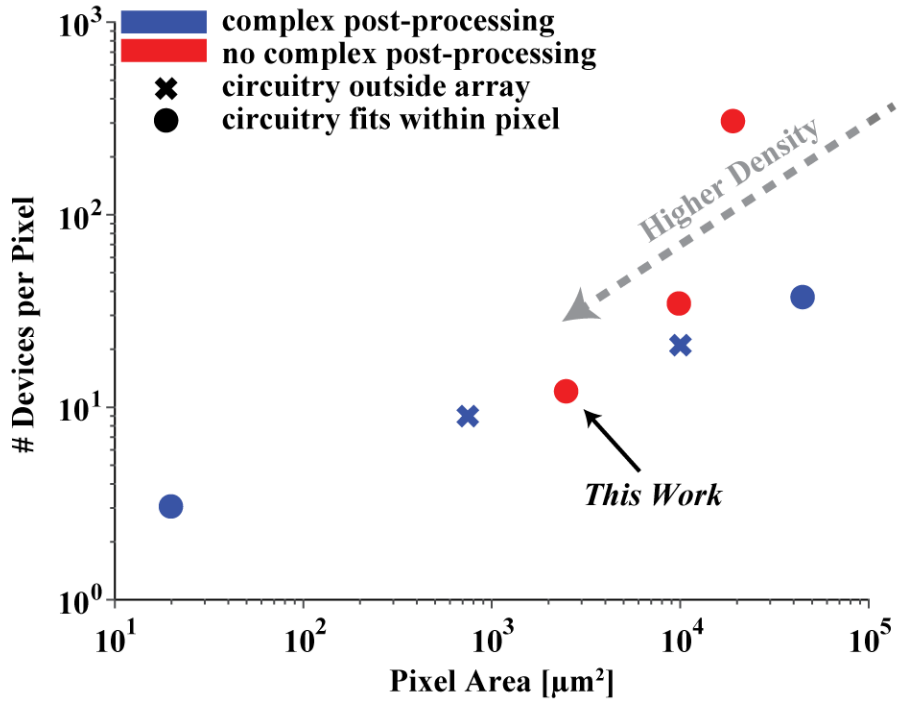

Figure 5.13. Plot comparing the pixel areas and number of devices per pixel of high-density electrode arrays summarized in the table.

Table 5.1. Comparison with state-of-the-art integrated electrochemical biosensor arrays

	HASSIBI [6]	MANICKAM [7]	KIM [8]	ROTHE [9]	HALL [20]	NASRI [10]	**THIS WORK**
Technology (µm)	0.18	0.35	0.5	0.35	0.032	0.065	***0.18***
Num. Pixels	50	100	100	1,024	8,192	4	***4,096***
Sensor Density [#/mm^2]	52.1	69.4	1,046	100	50,000	22.2	***400***
Total Density [#/mm^2]	11.90	25.00	11.11	28.44	327.68	0.44	***163.84***
Electrode Area [µm^2]	3,600	1,600	225	491	1	5,000	***2,025***
Pixel Area [µm^2]	19,200	10,000	745	10,000	20	45,000	***2,500***
Devices Per Pixel	301	34	>9*	21**	3	37	***12***
Complex Post-Processing?	NO	NO	YES	YES	YES	YES	***NO***
Dual Electrode?	YES	NO	NO	NO	YES	NO	***YES***
Technique	MULT.	EIS	CA	AMP.	CD	FSCV	***CD***

MULT – multiple techniques, EIS – Electrochemical Impedance Spectroscopy, CA – Chronoamperometry, Amp. – Amperometry, CD – Coulostatic discharge, FSCV – Fast scan cyclic voltammetry

* Part of the measurement circuitry is located outside of the pixel and a 50 fF capacitor and buffer circuit were not included in the device count.

** All the measurement circuitry is located outside of the pixel. This is a per row device number.

5.7 Conclusion

This paper presents a scalable coulostatic discharge-based high-density biosensor array designed to miniaturize multiple antibody measurement technology. Using coulostatic discharge rather than standard amperometry, the measurement circuitry in each biopixel is simplified to just a low-leakage switch and output buffer, thereby minimizing the overall density and area of the array. Furthermore, by optimizing on-chip IDE geometries and waiving fabrication design rules to create 3D structures, a signal amplification of ~10× was achieved without any complex, costly, and time-consuming post-processing of the sensors. Using this array, Rubella antibody was detected in human serum and simultaneous measurements of both Rubella and Mumps antibodies were possible on the same chip. These tests demonstrate this array's promise for use in full-scale IMS technology for rapid and accurate point-of-care screening and diagnosis.

Chapter 5, in full, is a reprint of the material as it appears in IEEE Journal of Solid-State Circuits 2018. Alexander C. Sun, Enrique Alvarez-Fontecilla, A. G. Venkatesh, Eliah Aronoff-Spencer, and Drew A. Hall, "*High-Density Redox Amplified Coulostatic Discharge-Based Biosensor Array*," IEEE Journal of Solid-State Circuits, pp. 1–11, 2018. The dissertation author was the first author of this paper.

Chapter 6

Summary

6.1 Summary of Dissertation

This dissertation describes improvements made to electrochemical measurement circuitry to shift biosensors towards the point-of-care by both bringing a diagnostic platform to the patient directly for at-home or remote testing and making multi-analyte testing more feasible in settings away from centralized labs. The following is a summary of the key points and results presented in the dissertation.

Chapter 1 demonstrated the motivation for point-of-care biosensors and their role in helping to solve current worldwide health issues. This chapter also introduced the benefits as well as the challenges in making PoC electrochemical biosensors. Chapter 2 presented a survey of the state-of-the-art PoC electrochemical biosensors that make efficient use of smartphones and other mobile devices. Chapter 3 presents the design of a multi-technique biosensor module to be integrated into a modular phone creating a portable and convenient testing platform. The key contribution is the efficient design of the single reconfigurable potentiostat intended to perform

three different electrochemical sensing modes all within a small form-factor. Each mode is able to achieve comparable performance to other state-of-the-art single technique devices while taking up only a fraction of the area. This module was paired with a modular smartphone and validated with real-world PoC assays for glucose, lactoferrin, pH, and label-free assays. This work was published in IEEE Transactions on Biomedical Circuit and Systems.

The following two chapters, 4 and 5, present the development of a scalable electrochemical detection method and measurement circuitry for multi-analyte high-density arrays. Chapter 4 details a board level relay-based solution for implementing coulostatic discharge, which greatly reduces and simplifies the measurement circuitry, and redox cycling with interdigitated microelectrodes. The device was successfully able to report the concentration of a redox molecule consistently across the entire 4×4 array. Chapter 5 describes a completely integrated version of the array with 64×64 pixels in a 0.18 µm SOI process with top metal electrodes and in-pixel coulostatic discharge measurement circuitry. Using a body-driven switch topology, the design was able to achieve attoampere leakage at the sensing node and a pixel size of 45×45 μm^2. The design and intentional removal of passivation across unprotected portions of the electrode resulted in a redox cycling amplification factor of ~10×. This array chip was able to successfully run a vaccination screening panel by simultaneously detecting antibodies for both Rubella and Mumps in human serum. It achieves the highest density amperometric array with no additional complex post-processing procedures.

6.2 Areas for Future Work

Both biosensor projects presented in this dissertation can be further expanded upon in a few ways. The next steps for the mHealth biosensor module would be to design a completely

integrated circuit version of the reconfigurable potentiostat, which would be much smaller and more suitable for installing inside a regular non-modular smartphone. To make the platform complete, we can include more measurement modes by adapting the circuit to provide galvanostatic capabilities, where current is applied and potential is measured. Also, since the current version is only a bipotentiostat, the addition of more working electrodes would allow the system to simultaneously use redox cycling amplification and have an experimental control.

While the high-density array was successful for multi-analyte detection, a few limitations hold it back from being used in a full-scale application. Firstly, the number of sensors needs to be increased at least 3× in order to be tested and compared with current IMS sensing technologies, which typically require 10,000 pixels functionalized with different peptides. While this can be accomplished now through simply increasing the silicon area, efforts to further increase the density such as through translating the design to a more advanced process, where other sources of leakage can begin to dominate, should be explored. Also, while it did not appear as a problem in our tests, both electrochemical and electrical pixel crosstalk should be further investigated and quantified. Finally, methods to improve the pixel-to-pixel variation should also be examined. While some sources of this variation are beyond the scope of this research such as the plating and surface functionalization techniques, the consistency of the double-layer capacitance is a concern that can be addressed. For example, adding a small on-chip capacitance to each pixel would reduce the amount of variation between sensors, but it would also decrease the sensitivity. A possible work-around would be to implement an on-chip calibration step to measure the double-layer capacitance of each pixel and use that to individually adjust the measured discharge rates, thereby improving the matching between sensors.

References

1. Chronic Disease Overview, Publications, Chronic Disease Prevention and Health Promotion, CDC Available online: https://www.cdc.gov/chronicdisease/overview/index.htm (accessed on May 5, 2018).

2. Ward, B. W.; Schiller, J. S.; Goodman, R. A. Multiple Chronic Conditions Among US Adults: A 2012 Update. *Prev. Chronic. Dis.* **2014**, *11*, doi:10.5888/pcd11.130389.

3. Additional Resources from AHRQ's Multiple Chronic Conditions (MCC) Research Network Available online: /professionals/prevention-chronic-care/decision/mcc/resources.html (accessed on May 14, 2018).

4. WHO The top 10 causes of death Available online: http://www.who.int/mediacentre/factsheets/fs310/en/ (accessed on May 6, 2018).

5. 2014 Ebola Outbreak in West Africa - Case Counts | Ebola Hemorrhagic Fever | CDC Available online: http://www.cdc.gov/vhf/ebola/outbreaks/2014-west-africa/case-counts.html (accessed on Apr 1, 2015).

6. Sun, A.; Wambach, T.; Venkatesh, A. G.; Hall, D. A. A low-cost smartphone-based electrochemical biosensor for point-of-care diagnostics. In *2014 IEEE Biomedical Circuits and Systems Conference (BioCAS)*; 2014; pp. 312–315.

7. Key figures – Ericsson Mobility Report Available online: https://www.ericsson.com/en/mobility-report/reports/november-2017/key-figures (accessed on May 3, 2018).

8. Rainie, L.; Perrin, rew 10 facts about smartphones as the iPhone turns 10. *Pew Res. Cent.* 2017.

9. Roda, A.; Michelini, E.; Zangheri, M.; Di Fusco, M.; Calabria, D.; Simoni, P. Smartphone-based biosensors: A critical review and perspectives. *TrAC Trends Anal. Chem.* **2016**, *79*, 317–325, doi:10.1016/j.trac.2015.10.019.

10. Quesada-González, D.; Merkoçi, A. Mobile phone-based biosensing: An emerging "diagnostic and communication" technology. *Biosens. Bioelectron.* **2017**, *92*, 549–562, doi:10.1016/j.bios.2016.10.062.

11. Zhang, D.; Liu, Q. Biosensors and bioelectronics on smartphone for portable biochemical detection. *Biosens. Bioelectron.* **2016**, *75*, 273–284, doi:10.1016/j.bios.2015.08.037.

12. Choi, S. Powering point-of-care diagnostic devices. *Biotechnol. Adv.* **2016**, *34*, 321–330, doi:10.1016/j.biotechadv.2015.11.004.

13. Lillehoj, P. B.; Huang, M.-C.; Truong, N.; Ho, C.-M. Rapid electrochemical detection on a mobile phone. *Lab. Chip* **2013**, *13*, 2950–2955, doi:10.1039/C3LC50306B.

14. Zhang, L.; Yang, W.; Yang, Y.; Liu, H.; Gu, Z. Smartphone-based point-of-care testing of salivary α-amylase for personal psychological measurement. *Analyst* **2015**, *140*, 7399–7406, doi:10.1039/C5AN01664A.

15. Deng, W.; Dou, Y.; Song, P.; Xu, H.; Aldalbahi, A.; Chen, N.; El-Sayed, N. N.; Gao, J.; Lu, J.; Song, S.; Zuo, X. Lab on smartphone with interfaced electrochemical chips for on-site gender verification. *J. Electroanal. Chem.* **2016**, *777*, 117–122, doi:10.1016/j.jelechem.2016.08.007.

16. Dou, Y.; Jiang, Z.; Deng, W.; Su, J.; Chen, S.; Song, H.; Aldalbahi, A.; Zuo, X.; Song, S.; Shi, J.; Fan, C. Portable detection of clenbuterol using a smartphone-based electrochemical biosensor with electric field-driven acceleration. *J. Electroanal. Chem.* **2016**, *781*, 339–344, doi:10.1016/j.jelechem.2016.04.022.

17. Pechlivanidis, N. G.; Papadimitriou, K. I.; Evans, D.; Vasilakis, N.; Prodromakis, T. Towards a smartphone-aided electronic ELISA for real-time electrochemical monitoring. In *2017 IEEE International Symposium on Circuits and Systems (ISCAS)*; 2017; pp. 1–4.

18. Sun, A.; Phelps, T.; Yao, C.; Venkatesh, A. G.; Conrad, D.; Hall, D. A. Smartphone-Based pH Sensor for Home Monitoring of Pulmonary Exacerbations in Cystic Fibrosis. *Sensors* **2017**, *17*, 1245, doi:10.3390/s17061245.

19. Jiang, H.; Sun, A.; Venkatesh, A. G.; Hall, D. A. An Audio Jack-Based Electrochemical Impedance Spectroscopy Sensor for Point-of-Care Diagnostics. *IEEE Sens. J.* **2017**, *17*, 589–597, doi:10.1109/JSEN.2016.2634530.

20. Yao, C.; Sun, A.; Hall, D. A. Efficient power harvesting from the mobile phone audio jack for mHealth peripherals. In *2015 IEEE Global Humanitarian Technology Conference (GHTC)*; 2015; pp. 219–225.

21. Sun, A. C.; Yao, C.; A.G., V.; Hall, D. A. An efficient power harvesting mobile phone-based electrochemical biosensor for point-of-care health monitoring. *Sens. Actuators B Chem.* **2016**, *235*, 126–135, doi:10.1016/j.snb.2016.05.010.

22. Nemiroski, A.; Christodouleas, D. C.; Hennek, J. W.; Kumar, A. A.; Maxwell, E. J.; Fernández-Abedul, M. T.; Whitesides, G. M. Universal mobile electrochemical detector

designed for use in resource-limited applications. *Proc. Natl. Acad. Sci.* **2014**, *111*, 11984–11989, doi:10.1073/pnas.1405679111.

23. Wang, X.; Gartia, M. R.; Jiang, J.; Chang, T.-W.; Qian, J.; Liu, Y.; Liu, X.; Liu, G. L. Audio jack based miniaturized mobile phone electrochemical sensing platform. *Sens. Actuators B Chem.* **2015**, *209*, 677–685, doi:10.1016/j.snb.2014.12.017.

24. Jiang, J.; Wang, X.; Chao, R.; Ren, Y.; Hu, C.; Xu, Z.; Liu, G. L. Smartphone based portable bacteria pre-concentrating microfluidic sensor and impedance sensing system. *Sens. Actuators B Chem.* **2014**, *193*, 653–659, doi:10.1016/j.snb.2013.11.103.

25. Zhang, D.; Jiang, J.; Chen, J.; Zhang, Q.; Lu, Y.; Yao, Y.; Li, S.; Logan Liu, G.; Liu, Q. Smartphone-based portable biosensing system using impedance measurement with printed electrodes for 2,4,6-trinitrotoluene (TNT) detection. *Biosens. Bioelectron.* **2015**, *70*, 81–88, doi:10.1016/j.bios.2015.03.004.

26. Giordano, G. F.; Vicentini, M. B. R.; Murer, R. C.; Augusto, F.; Ferrão, M. F.; Helfer, G. A.; da Costa, A. B.; Gobbi, A. L.; Hantao, L. W.; Lima, R. S. Point-of-use electroanalytical platform based on homemade potentiostat and smartphone for multivariate data processing. *Electrochimica Acta* **2016**, *219*, 170–177, doi:10.1016/j.electacta.2016.09.157.

27. Fan, Y.; Liu, J.; Wang, Y.; Luo, J.; Xu, H.; Xu, S.; Cai, X. A wireless point-of-care testing system for the detection of neuron-specific enolase with microfluidic paper-based analytical devices. *Biosens. Bioelectron.* **2017**, *95*, 60–66, doi:10.1016/j.bios.2017.04.003.

28. Ji, D.; Liu, L.; Li, S.; Chen, C.; Lu, Y.; Wu, J.; Liu, Q. Smartphone-based cyclic voltammetry system with graphene modified screen printed electrodes for glucose detection. *Biosens. Bioelectron.* **2017**, *98*, 449–456, doi:10.1016/j.bios.2017.07.027.

29. Jung, J.; Lee, J.; Shin, S.; Kim, Y. T. Development of a Telemetric, Miniaturized Electrochemical Amperometric Analyzer. *Sensors* **2017**, *17*, 2416, doi:10.3390/s17102416.

30. Liu, L.; Zhang, D.; Zhang, Q.; Chen, X.; Xu, G.; Lu, Y.; Liu, Q. Smartphone-based sensing system using ZnO and graphene modified electrodes for VOCs detection. *Biosens. Bioelectron.* **2017**, *93*, 94–101, doi:10.1016/j.bios.2016.09.084.

31. Talukder, N.; Furniturewalla, A.; Le, T.; Chan, M.; Hirday, S.; Cao, X.; Xie, P.; Lin, Z.; Gholizadeh, A.; Orbine, S.; Javanmard, M. A portable battery powered microfluidic impedance cytometer with smartphone readout: towards personal health monitoring. *Biomed. Microdevices* **2017**, *19*, 36, doi:10.1007/s10544-017-0161-8.

32. Wang, X.; Lin, G.; Cui, G.; Zhou, X.; Liu, G. L. White blood cell counting on smartphone paper electrochemical sensor. *Biosens. Bioelectron.* **2017**, *90*, 549–557, doi:10.1016/j.bios.2016.10.017.

33. Yang, L.; Chen, T. A handheld electrochemical sensing platform for point-of-care diagnostic applications. In *2017 IEEE Biomedical Circuits and Systems Conference (BioCAS)*; 2017; pp. 1–4.

34. Ainla, A.; Mousavi, M. P. S.; Tsaloglou, M.-N.; Redston, J.; Bell, J. G.; Fernández-Abedul, M. T.; Whitesides, G. M. Open-Source Potentiostat for Wireless Electrochemical Detection with Smartphones. *Anal. Chem.* **2018**, doi:10.1021/acs.analchem.8b00850.

35. Bandodkar, A. J.; Imani, S.; Nuñez-Flores, R.; Kumar, R.; Wang, C.; Mohan, A. M. V.; Wang, J.; Mercier, P. P. Re-usable electrochemical glucose sensors integrated into a smartphone platform. *Biosens. Bioelectron.* **2018**, *101*, 181–187, doi:10.1016/j.bios.2017.10.019.

36. Rowe, A. A.; Bonham, A. J.; White, R. J.; Zimmer, M. P.; Yadgar, R. J.; Hobza, T. M.; Honea, J. W.; Ben-Yaacov, I.; Plaxco, K. W. CheapStat: An Open-Source, "Do-It-Yourself" Potentiostat for Analytical and Educational Applications. *PLoS ONE* **2011**, *6*, e23783, doi:10.1371/journal.pone.0023783.

37. Berg, B.; Cortazar, B.; Tseng, D.; Ozkan, H.; Feng, S.; Wei, Q.; Chan, R. Y.-L.; Burbano, J.; Farooqui, Q.; Lewinski, M.; Di Carlo, D.; Garner, O. B.; Ozcan, A. Cellphone-Based Hand-Held Microplate Reader for Point-of-Care Testing of Enzyme-Linked Immunosorbent Assays. *ACS Nano* **2015**, *9*, 7857–7866, doi:10.1021/acsnano.5b03203.

38. Oncescu, V.; O'Dell, D.; Erickson, D. Smartphone based health accessory for colorimetric detection of biomarkers in sweat and saliva. *Lab. Chip* **2013**, *13*, 3232–3238, doi:10.1039/C3LC50431J.

39. Ionescu, C.; Svasta, P.; Tamas, C.; Bala, C.; Rotariu, L. Portable measuring and display unit for electrochemical sensors. In *Design and Technology in Electronic Packaging (SIITME), 2010 IEEE 16th International Symposium for*; 2010; pp. 215–218.

40. Ludwig, S. K. J.; Tokarski, C.; Lang, S. N.; van Ginkel, L. A.; Zhu, H.; Ozcan, A.; Nielen, M. W. F. Calling Biomarkers in Milk Using a Protein Microarray on Your Smartphone. *PLoS ONE* **2015**, *10*, e0134360, doi:10.1371/journal.pone.0134360.

41. Ludwig, S. K. J.; Zhu, H.; Phillips, S.; Shiledar, A.; Feng, S.; Tseng, D.; Ginkel, L. A. van; Nielen, M. W. F.; Ozcan, A. Cellphone-based detection platform for rbST biomarker analysis in milk extracts using a microsphere fluorescence immunoassay. *Anal. Bioanal. Chem.* **2014**, *406*, 6857–6866, doi:10.1007/s00216-014-7984-4.

42. McGeough, C. M.; O'Driscoll, S. Camera Phone-Based Quantitative Analysis of C-Reactive Protein ELISA. *IEEE Trans. Biomed. Circuits Syst.* **2013**, *7*, 655–659, doi:10.1109/TBCAS.2012.2234122.

43. Cevenini, L.; Calabretta, M. M.; Tarantino, G.; Michelini, E.; Roda, A. Smartphone-interfaced 3D printed toxicity biosensor integrating bioluminescent “sentinel cells.” *Sens. Actuators B Chem.*, doi:10.1016/j.snb.2015.11.017.

44. Su, K.; Zou, Q.; Zhou, J.; Zou, L.; Li, H.; Wang, T.; Hu, N.; Wang, P. High-sensitive and high-efficient biochemical analysis method using a bionic electronic eye in combination with a smartphone-based colorimetric reader system. *Sens. Actuators B Chem.* **2015**, *216*, 134–140, doi:10.1016/j.snb.2015.04.052.

45. Xu, W.; Lu, S.; Chen, Y.; Zhao, T.; Jiang, Y.; Wang, Y.; Chen, X. Simultaneous color sensing of O2 and pH using a smartphone. *Sens. Actuators B Chem.* **2015**, *220*, 326–330, doi:10.1016/j.snb.2015.05.088.

46. Zangheri, M.; Cevenini, L.; Anfossi, L.; Baggiani, C.; Simoni, P.; Di Nardo, F.; Roda, A. A simple and compact smartphone accessory for quantitative chemiluminescence-based lateral flow immunoassay for salivary cortisol detection. *Biosens. Bioelectron.* **2015**, *64*, 63–68, doi:10.1016/j.bios.2014.08.048.

47. Zhang, D.; Lu, Y.; Zhang, Q.; Liu, L.; Li, S.; Yao, Y.; Jiang, J.; Liu, G. L.; Liu, Q. Protein detecting with smartphone-controlled electrochemical impedance spectroscopy for point-of-care applications. *Sens. Actuators B Chem.* **2016**, *222*, 994–1002, doi:10.1016/j.snb.2015.09.041.

48. Doeven, E. H.; Barbante, G. J.; Harsant, A. J.; Donnelly, P. S.; Connell, T. U.; Hogan, C. F.; Francis, P. S. Mobile phone-based electrochemiluminescence sensing exploiting the ‘USB On-The-Go’ protocol. *Sens. Actuators B Chem.* **2015**, *216*, 608–613, doi:10.1016/j.snb.2015.04.087.

49. Allen J. Bard; Larry R. Faulkner *Electrochemical Methods Fundamentals and Applications*; 2nd ed.; Wiley, 2001;

50. Butt, H.-J.; Graf, K.; Kappl, M. *Physics and Chemistry of Interfaces*; 2nd ed.; Weinheim: Wiley-VCH, 2006;

51. Nazari, M. H.; Mazhab-Jafari, H.; Leng, L.; Guenther, A.; Genov, R. CMOS Neurotransmitter Microarray: 96-Channel Integrated Potentiostat With On-Die Microsensors. *IEEE Trans. Biomed. Circuits Syst.* **2013**, *7*, 338–348, doi:10.1109/TBCAS.2012.2203597.

52. Ahmadi, M. M.; Jullien, G. A. Current-Mirror-Based Potentiostats for Three-Electrode Amperometric Electrochemical Sensors. *IEEE Trans. Circuits Syst. Regul. Pap.* **2009**, *56*, 1339–1348, doi:10.1109/TCSI.2008.2005927.

53. Stanacevic, M.; Murari, K.; Rege, A.; Cauwenberghs, G.; Thakor, N. V. VLSI Potentiostat Array With Oversampling Gain Modulation for Wide-Range Neurotransmitter Sensing. *IEEE Trans. Biomed. Circuits Syst.* **2007**, *1*, 63–72, doi:10.1109/TBCAS.2007.893176.

54. Manickam, A.; Chevalier, A.; McDermott, M.; Ellington, A. D.; Hassibi, A. A CMOS Electrochemical Impedance Spectroscopy (EIS) Biosensor Array. *IEEE Trans. Biomed. Circuits Syst.* **2010**, *4*, 379–390, doi:10.1109/TBCAS.2010.2081669.

55. Carullo, A.; Ferraris, F.; Parvis, M.; Vallan, A.; Angelini, E.; Spinelli, P. Low-cost electrochemical impedance spectroscopy system for corrosion monitoring of metallic antiquities and works of art. *IEEE Trans. Instrum. Meas.* **2000**, *49*, 371–375, doi:10.1109/19.843080.

56. Jafari, H.; Soleymani, L.; Genov, R. 16-Channel CMOS Impedance Spectroscopy DNA Analyzer With Dual-Slope Multiplying ADCs. *IEEE Trans. Biomed. Circuits Syst.* **2012**, *6*, 468–478, doi:10.1109/TBCAS.2012.2226334.

57. Vergani, M.; Carminati, M.; Ferrari, G.; Landini, E.; Caviglia, C.; Heiskanen, A.; Comminges, C.; Zor, K.; Sabourin, D.; Dufva, M.; Dimaki, M.; Raiteri, R.; Wollenberger, U.; Emneus, J.; Sampietro, M. Multichannel Bipotentiostat Integrated With a Microfluidic Platform for Electrochemical Real-Time Monitoring of Cell Cultures. *IEEE Trans. Biomed. Circuits Syst.* **2012**, *6*, 498–507, doi:10.1109/TBCAS.2012.2187783.

58. Li, L.; Liu, X.; Qureshi, W. A.; Mason, A. J. CMOS Amperometric Instrumentation and Packaging for Biosensor Array Applications. *IEEE Trans. Biomed. Circuits Syst.* **2011**, *5*, 439–448, doi:10.1109/TBCAS.2011.2171339.

59. Sun, A.; Wambach, T.; Venkatesh, A. G.; Hall, D. A. A multitechnique reconfigurable electrochemical biosensor for integration into mobile technologies. In *2015 IEEE Biomedical Circuits and Systems Conference (BioCAS)*; 2015; pp. 1–4.

60. Hwang, S.; Sonkusale, S. CMOS VLSI Potentiostat for Portable Environmental Sensing Applications. *IEEE Sens. J.* **2010**, *10*, 820–821, doi:10.1109/JSEN.2009.2035098.

61. Ramfos, I.; Vassiliadis, N.; Blionas, S.; Efstathiou, K.; Fragoso, A.; O'Sullivan, C. K.; Birbas, A. A compact hybrid-multiplexed potentiostat for real-time electrochemical biosensing applications. *Biosens. Bioelectron.* **2013**, *47*, 482–489, doi:10.1016/j.bios.2013.03.068.

62. Das, J.; Jo, K.; Lee, J. W.; Yang, H. Electrochemical Immunosensor Using p-Aminophenol Redox Cycling by Hydrazine Combined with a Low Background Current. *Anal. Chem.* **2007**, *79*, 2790–2796, doi:10.1021/ac062291l.

63. Daniels, J. S.; Anderson, E. P.; Lee, T. H.; Pourmand, N. Simultaneous measurement of nonlinearity and electrochemical impedance for protein sensing using two-tone excitation. In *30th Annual International Conference of the IEEE Engineering in Medicine and Biology Society, 2008. EMBS 2008*; 2008; pp. 5753–5756.

64. Park, J.-H.; Park, G.-T.; Cho, I. H.; Sim, S.-M.; Yang, J.-M.; Lee, D.-Y. An antimicrobial protein, lactoferrin exists in the sweat: proteomic analysis of sweat. *Exp. Dermatol.* **2011**, *20*, 369–371, doi:10.1111/j.1600-0625.2010.01218.x.

65. Mizuhashi, F.; Koide, K.; Toya, S.; Takahashi, M.; Mizuhashi, R.; Shimomura, H. Levels of the antimicrobial proteins lactoferrin and chromogranin in the saliva of individuals with oral dryness. *J. Prosthet. Dent.*, doi:10.1016/j.prosdent.2013.12.028.

66. Arao, S.; Matsuura, S.; Nonomura, M.; Miki, K.; Kabasawa, K.; Nakanishi, H. Measurement of Urinary Lactoferrin as a Marker of Urinary Tract Infection. *J. Clin. Microbiol.* **1999**, *37*, 553–557.

67. Kijlstra, A.; Jeurissen, S. H.; Koning, K. M. Lactoferrin levels in normal human tears. *Br. J. Ophthalmol.* **1983**, *67*, 199–202.

68. Joishy, M.; Davies, I.; Ahmed, M.; Wassel, J.; Davies, K.; Sayers, A.; Jenkins, H. Fecal Calprotectin and Lactoferrin as Noninvasive Markers of Pediatric Inflammatory Bowel Disease: *J. Pediatr. Gastroenterol. Nutr.* **2009**, *48*, 48–54, doi:10.1097/MPG.0b013e31816533d3.

69. Daniels, J. S.; Pourmand, N. Label-Free Impedance Biosensors: Opportunities and Challenges. *Electroanalysis* **2007**, *19*, 1239–1257, doi:10.1002/elan.200603855.

70. Katz, E.; Willner, I. Probing Biomolecular Interactions at Conductive and Semiconductive Surfaces by Impedance Spectroscopy: Routes to Impedimetric Immunosensors, DNA-Sensors, and Enzyme Biosensors. *Electroanalysis* **2003**, *15*, 913–947, doi:10.1002/elan.200390114.

71. Xu, M.; Luo, X.; Davis, J. J. The label free picomolar detection of insulin in blood serum. *Biosens. Bioelectron.* **2013**, *39*, 21–25, doi:10.1016/j.bios.2012.06.014.

72. Ohno, R.; Ohnuki, H.; Wang, H.; Yokoyama, T.; Endo, H.; Tsuya, D.; Izumi, M. Electrochemical impedance spectroscopy biosensor with interdigitated electrode for detection of human immunoglobulin A. *Biosens. Bioelectron.* **2013**, *40*, 422–426, doi:10.1016/j.bios.2012.07.052.

73. Bryan, T.; Luo, X.; Bueno, P. R.; Davis, J. J. An optimised electrochemical biosensor for the label-free detection of C-reactive protein in blood. *Biosens. Bioelectron.* **2013**, *39*, 94–98, doi:10.1016/j.bios.2012.06.051.

74. Cruz, A. F. D.; Norena, N.; Kaushik, A.; Bhansali, S. A low-cost miniaturized potentiostat for point-of-care diagnosis. *Biosens. Bioelectron.* **2014**, *62*, 249–254, doi:10.1016/j.bios.2014.06.053.

75. Steinberg, M. D.; Kassal, P.; Kereković, I.; Steinberg, I. M. A wireless potentiostat for mobile chemical sensing and biosensing. *Talanta* **2015**, *143*, 178–183, doi:10.1016/j.talanta.2015.05.028.

76. Angelini, E.; Corbellini, S.; Parvis, M.; Ferraris, F.; Grassini, S. An Arduino-based EIS with a logarithmic amplifier for corrosion monitoring. In *Instrumentation and Measurement Technology Conference (I2MTC) Proceedings, 2014 IEEE International*; 2014; pp. 905–910.

77. Punter-Villagrasa, J.; del Moral-Zamora, B.; Colomer-Farrarons, J.; Miribel-Catala, P.; Cid, J.; Rodriguez-Villarreal, I.; Prieto-Simon, B. A portable point-of-use EIS device for in-vivo biom #x00E9;dical applications. In *2014 Conference on Design of Circuits and Integrated Circuits (DCIS)*; 2014; pp. 1–6.

78. Legutki, J. B.; Zhao, Z.-G.; Greving, M.; Woodbury, N.; Johnston, S. A.; Stafford, P. Scalable high-density peptide arrays for comprehensive health monitoring. *Nat. Commun.* **2014**, *5*, 4785, doi:10.1038/ncomms5785.

79. Stanacevic, M.; Murari, K.; Cauwenberghs, G.; Thakor, N. 16-channel wide-range VLSI potentiostat array. In *2004 IEEE International Workshop on Biomedical Circuits and Systems*; 2004; p. S1/7/INV-S1/17-20.

80. Li, L.; Qureshi, W. A.; Liu, X.; Mason, A. J. Amperometric instrumentation system with on-chip electrode array for biosensor application. In *2010 IEEE Biomedical Circuits and Systems Conference (BioCAS)*; 2010; pp. 294–297.

81. Liu, X.; Li, L.; Awate, B.; Worden, R. M.; Reguera, G.; Mason, A. J. Biosensor array microsystem on a CMOS amperometric readout chip. In *2011 IEEE Biomedical Circuits and Systems Conference (BioCAS)*; 2011; pp. 305–308.

82. Luo, T.; Wang, H.; Song, H.; Christen, J. B. CMOS-based on-chip electrochemical sensor. In *2014 IEEE Biomedical Circuits and Systems Conference (BioCAS)*; 2014; pp. 336–339.

83. Price, J. V.; Tangsombatvisit, S.; Xu, G.; Yu, J.; Levy, D.; Baechler, E. C.; Gozani, O.; Varma, M.; Utz, P. J.; Liu, C. L. On silico peptide microarrays for high-resolution mapping of antibody epitopes and diverse protein-protein interactions. *Nat. Med.* **2012**, *18*, 1434–1440, doi:10.1038/nm.2913.

84. Delahay, P. Coulostatic Method for the Kinetic Study of Fast Electrode Processes. I. Theory. *J. Phys. Chem.* **1962**, *66*, 2204–2207, doi:10.1021/j100817a030.

85. Reinmuth, W. H.; Wilson, C. E. An Impulse (Coulostatic) Relaxation Method for the Study of Rapid Electrode Processes. *Anal. Chem.* **1962**, *34*, 1159–1161, doi:10.1021/ac60189a002.

86. Zhu, X.; Choi, J.-W.; Ahn, C. H. A new dynamic electrochemical transduction mechanism for interdigitated array microelectrodes. *Lab. Chip* **2004**, *4*, 581–587, doi:10.1039/B407930B.

87. Anderson, L. B.; Reilley, C. N. Thin-layer electrochemistry: steady-state methods of studying rate processes. *J. Electroanal. Chem. 1959* **1965**, *10*, 295–305, doi:10.1016/0022-0728(65)85063-X.

88. Stafford, P.; Cichacz, Z.; Woodbury, N. W.; Johnston, S. A. Immunosignature system for diagnosis of cancer. *Proc. Natl. Acad. Sci.* **2014**, *111*, E3072–E3080, doi:10.1073/pnas.1409432111.

89. Legutki, J. B.; Zhao, Z.-G.; Greving, M.; Woodbury, N.; Johnston, S. A.; Stafford, P. Scalable high-density peptide arrays for comprehensive health monitoring. *Nat. Commun.* **2014**, *5*, doi:10.1038/ncomms5785.

90. Legutki, J. B.; Johnston, S. A. Immunosignatures can predict vaccine efficacy. *Proc. Natl. Acad. Sci. U. S. A.* **2013**, *110*, 18614–18619, doi:10.1073/pnas.1309390110.

91. Restrepo, L.; Stafford, P.; Johnston, S. A. Feasibility of an early Alzheimer's disease immunosignature diagnostic test. *J. Neuroimmunol.* **2013**, *254*, 154–160, doi:10.1016/j.jneuroim.2012.09.014.

92. Hassibi, A.; Lee, T. H. A programmable electrochemical biosensor array in 0.18 μm standard CMOS. In *ISSCC. 2005 IEEE International Digest of Technical Papers. Solid-State Circuits Conference, 2005.*; 2005; pp. 564-617 Vol. 1.

93. Manickam, A.; Chevalier, A.; McDermott, M.; Ellington, A. D.; Hassibi, A. A CMOS electrochemical impedance spectroscopy biosensor array for label-free biomolecular detection. In *2010 IEEE International Solid-State Circuits Conference - (ISSCC)*; 2010; pp. 130–131.

94. Kim, B. N.; Herbst, A. D.; Kim, S. J.; Minch, B. A.; Lindau, M. Parallel recording of neurotransmitters release from chromaffin cells using a 10×10 CMOS IC potentiostat array with on-chip working electrodes. *Biosens. Bioelectron.* **2013**, *41*, 736–744, doi:10.1016/j.bios.2012.09.058.

95. Rothe, J.; Frey, O.; Stettler, A.; Chen, Y.; Hierlemann, A. Fully Integrated CMOS Microsystem for Electrochemical Measurements on 32 × 32 Working Electrodes at 90 Frames Per Second. *Anal. Chem.* **2014**, *86*, 6425–6432, doi:10.1021/ac500862v.

96. Nasri, B.; Wu, T.; Alharbi, A.; Gupta, M.; RanjitKumar, R.; Sebastian, S.; Wang, Y.; Kiani, R.; Shahrjerdi, D. 15.7 Heterogeneous integrated CMOS-graphene sensor array for dopamine detection. In *2017 IEEE International Solid-State Circuits Conference (ISSCC)*; 2017; pp. 268–269.

97. Ghoreishizadeh, S. S.; Georgiou, P.; Carrara, S.; Micheli, G. D. An integrated platform for differential electrochemical and ISFET sensing. In *2016 IEEE International Symposium on Circuits and Systems (ISCAS)*; 2016; pp. 2875–2878.

98. Niitsu, K.; Ota, S.; Gamo, K.; Kondo, H.; Hori, M.; Nakazato, K. Development of Microelectrode Arrays Using Electroless Plating for CMOS-Based Direct Counting of Bacterial and HeLa Cells. *IEEE Trans. Biomed. Circuits Syst.* **2015**, *9*, 607–619, doi:10.1109/TBCAS.2015.2479656.

99. Chen, Y.; Wong, C. C.; Pui, T. S.; Nadipalli, R.; Weerasekera, R.; Chandran, J.; Yu, H.; Rahman, A. R. A. CMOS high density electrical impedance biosensor array for tumor cell detection. *Sens. Actuators B Chem.* **2012**, *173*, 903–907, doi:10.1016/j.snb.2012.07.024.

100. Li, L.; Liu, X.; Qureshi, W. A.; Mason, A. J. CMOS Amperometric Instrumentation and Packaging for Biosensor Array Applications. *IEEE Trans. Biomed. Circuits Syst.* **2011**, *5*, 439–448, doi:10.1109/TBCAS.2011.2171339.

101. Yang, C.; Huang, Y.; Hassler, B. L.; Worden, R. M.; Mason, A. J. Amperometric Electrochemical Microsystem for a Miniaturized Protein Biosensor Array. *IEEE Trans. Biomed. Circuits Syst.* **2009**, *3*, 160–168, doi:10.1109/TBCAS.2009.2015650.

102. Levine, P. M.; Gong, P.; Levicky, R.; Shepard, K. L. Active CMOS Sensor Array for Electrochemical Biomolecular Detection. *IEEE J. Solid-State Circuits* **2008**, *43*, 1859–1871, doi:10.1109/JSSC.2008.925407.

103. Ayers, S.; Gillis, K. D.; Lindau, M.; Minch, B. A. Design of a CMOS Potentiostat Circuit for Electrochemical Detector Arrays. *IEEE Trans. Circuits Syst. Regul. Pap.* **2007**, *54*, 736–744, doi:10.1109/TCSI.2006.888777.

104. Thewes, R.; Hofmann, F.; Frey, A.; Holzapfl, B.; Schienle, M.; Paulus, C.; Schindler, P.; Eckstein, G.; Kassel, C.; Stanzel, M.; Hintsche, R.; Nebling, E.; Albers, J.; Hassman, J.; Schulein, J.; Goemann, W.; Gumbrecht, W. Sensor arrays for fully-electronic DNA detection on CMOS. In *2002 IEEE International Solid-State Circuits Conference*; 2002; Vol. 1, pp. 350–473 vol.1.

105. Augustyniak, M.; Paulus, C.; Brederlow, R.; Persike, N.; Hartwich, G.; Schmitt-Landsiedel, D.; Thewes, R. A 24x16 CMOS-Based Chronocoulometric DNA Microarray. In *2006 IEEE International Solid State Circuits Conference - Digest of Technical Papers*; 2006; pp. 59–68.

106. Hall, D. A.; Daniels, J. S.; Geuskens, B.; Tayebi, N.; Credo, G. M.; Liu, D. J.; Li, H.; Wu, K.; Su, X.; Varma, M.; Elibol, O. H. 16.1 A nanogap transducer array on 32nm CMOS for electrochemical DNA sequencing. In *2016 IEEE International Solid-State Circuits Conference (ISSCC)*; 2016; pp. 288–289.

107. Ma, C.; Contento, N. M.; Bohn, P. W. Redox Cycling on Recessed Ring-Disk Nanoelectrode Arrays in the Absence of Supporting Electrolyte. *J. Am. Chem. Soc.* **2014**, *136*, 7225–7228, doi:10.1021/ja502052s.

108. Ino, K.; Kanno, Y.; Nishijo, T.; Komaki, H.; Yamada, Y.; Yoshida, S.; Takahashi, Y.; Shiku, H.; Matsue, T. Densified Electrochemical Sensors Based on Local Redox Cycling between Vertically Separated Electrodes in Substrate Generation/Chip Collection and Extended Feedback Modes. *Anal. Chem.* **2014**, *86*, 4016–4023, doi:10.1021/ac500435d.

109. Sun, A.; Alvarez-Fontecilla, E.; Venkatesh, A. G.; Aronoff-Spencer, E.; Hall, D. A. A 64×64 High-Density Redox Amplified Coulostatic Discharge-Based Biosensor Array in 180nm CMOS. In; Leuven, Belgium, 2017.

110. Zhu, X.; Ahn, C. H. On-Chip Electrochemical Analysis System Using Nanoelectrodes and Bioelectronic CMOS Chip. *IEEE Sens. J.* **2006**, *6*, 1280–1286, doi:10.1109/JSEN.2006.881351.

111. Sun, A.; Au, A.; Venkatesh, A. G.; Gilja, V.; Hall, D. A. A scalable high-density electrochemical biosensor array for parallelized point-of-care diagnostics. In *2015 IEEE Biomedical Circuits and Systems Conference (BioCAS)*; 2015; pp. 1–4.

112. Halperin, R. F.; Stafford, P.; Johnston, S. A. Exploring Antibody Recognition of Sequence Space through Random-Sequence Peptide Microarrays. *Mol. Cell. Proteomics MCP* **2011**, *10*, doi:10.1074/mcp.M110.000786.

113. Brown, J. R.; Stafford, P.; Johnston, S. A.; Dinu, V. Statistical methods for analyzing immunosignatures. *BMC Bioinformatics* **2011**, *12*, 349, doi:10.1186/1471-2105-12-349.

114. Breitling, F.; Nesterov, A.; Stadler, V.; Felgenhauer, T.; Bischoff, F. R. High-density peptide arrays. *Mol. Biosyst.* **2009**, *5*, 224–234, doi:10.1039/B819850K.

115. Legutki, J. B.; Magee, D. M.; Stafford, P.; Johnston, S. A. A general method for characterization of humoral immunity induced by a vaccine or infection. *Vaccine* **2010**, *28*, 4529–4537, doi:10.1016/j.vaccine.2010.04.061.

116. Avila, D.; Alvarez, E.; Abusleme, A. Noise Analysis in Pulse-Processing Discrete-Time Filters. *IEEE Trans. Nucl. Sci.* **2013**, *60*, 4634–4640, doi:10.1109/TNS.2013.2283242.

117. Dam, V. a. T.; Olthuis, W.; Berg, A. van den Redox cycling with facing interdigitated array electrodes as a method for selective detection of redox species. *Analyst* **2007**, *132*, 365–370, doi:10.1039/B616667A.

118. Min, J.; Baeumner, A. J. Characterization and Optimization of Interdigitated Ultramicroelectrode Arrays as Electrochemical Biosensor Transducers. **2004**, 724–729.

119. Paeschke, M.; Wollenberger, U.; Köhler, C.; Lisec, T.; Schnakenberg, U.; Hintsche, R. Properties of interdigital electrode arrays with different geometries. *Anal. Chim. Acta* **1995**, *305*, 126–136, doi:10.1016/0003-2670(95)00440-B.

120. Aoki, K.; Morita, M.; Niwa, O.; Tabei, H. Quantitative analysis of reversible diffusion-controlled currents of redox soluble species at interdigitated array electrodes under steady-state conditions. *J. Electroanal. Chem. Interfacial Electrochem.* **1988**, *256*, 269–282, doi:10.1016/0022-0728(88)87003-7.

121. Su, J. J.; Demirci, K. S.; Brand, O. A Low-Leakage Body-Guarded Analog Switch in 0.35-BiCMOS and Its Applications in Low-Speed Switched-Capacitor Circuits. *IEEE Trans. Circuits Syst. II Express Briefs* **2015**, *62*, 947–951, doi:10.1109/TCSII.2015.2458093.

122. Ota, S.; Niitsu, K.; Kondo, H.; Hori, M.; Nakazato, K. A CMOS sensor platform with 1.2 μm × 2.05 μm electroless-plated 1024 × 1024 microelectrode array for high-sensitivity rapid direct bacteria counting. In *2014 IEEE Biomedical Circuits and Systems Conference (BioCAS) Proceedings*; 2014; pp. 460–463.

123. Hwang, S.; LaFratta, C. N.; Agarwal, V.; Yu, X.; Walt, D. R.; Sonkusale, S. CMOS Microelectrode Array for Electrochemical Lab-on-a-Chip Applications. *IEEE Sens. J.* **2009**, *9*, 609–615, doi:10.1109/JSEN.2009.2020193.